Theory, Development and Validation of a Novel Label-Free Waveguide Grating based Biosensor System

A dissertation submitted to
ETH Zürich
Diss. ETH No. 22799
Florian Kehl, 2015

$$n_{c/s} \cdot sin(\theta_c) = n_{eff} - \frac{m_g \lambda}{\Lambda}$$

c) $\lambda = 779.7 \pm 0.2$ nm

Diss. ETH N° 22799

Theory, Development and Validation of a Novel Label-Free Waveguide Grating based Biosensor System

A dissertation submitted to

ETH ZÜRICH

for the degree of

DOCTOR OF SCIENCES
(Dr. sc. ETH Zurich)

presented by

FLORIAN KEHL

MSc. in Nanosciences
born on 13.04.1984
citizen of Oberegg (AI)

accepted on the recommendation of

Prof. Dr. János Vörös, examiner
Prof. Dr. Christoph Stamm, co-examiner
Dr. Stéphane Follonier, co-examiner

2015

To my parents

Acknowledgments

First of all I would like to express my sincere gratitude to my professor and supervisor Janos Vörös from the Laboratory of Biosensors and Bio-electronics at the Federal Institute of Technology ETH in Zürich. With his supportive nature, generous and collegial group management style and positive attitude, he succeeds in creating an incredible, truly unique environment. I therefore also thank the entire LBB group for the memorable time and for being an outstanding team.

I would also like to thank Max Wiki and Peter Seitz for initially bringing me to CSEM Landquart, for mentoring and inspiring me during the beginning of my thesis. My sincere gratitude also goes to Stéphane Follonier, Division Head at CSEM Landquart, FP7 Project Coordinator and co-referee, for his unlimited trust, academic freedom and perpetual support. In this context, I would also like to thank my second co-referee Christoph Stamm from the ZHAW Winterthur.

This work would not have been possible without the support of many highly talented individuals, who managed to pull all in the same direction to act as a team. I would like to thank Noe Tscharner and Gerhard Etlinger for their contributions in the electronics design, my diligent students Luca Hirt, Thomas Guillod, Mirjad Keka, David Bischof, Thomas Gartmann and Philip Häner for their invaluable contributions, Christoph Hofer with his broad background in optics, Sarah Heub, Véronique Monnier and Hui Gao for their support in microfluidics and bio-chemistry. Many thanks also to Patrick Grandi and Andrea Giangreco for their support in mechanical engineering. Additionally, I would like to thank Maurus Tschirky, Stefano Cattaneo, Stefan Arnold and the entire

Acknowledgments

....

....

Contents

Contents

....

....

Contents

....

....

Summary

Label-free optical biosensors are important tools to study the kinetics, interaction and presence of (bio)chemical compounds in various fields, such as biotechnology, pharmaceutical industry, diagnostics as well as in-situ environmental monitoring. The objective of the dissertation at hand is to give a comprehensive overview of the individual tasks required to design, engineer and test an automated and fully integrated biosensor system.

Planar optical waveguides with input grating couplers are highly sensitive transducers and are of interest as they offer multiple tuning parameters for the sensor chip design. In the first part of this thesis, an algorithm based on Transmission Line Transfer Matrix Method combined with Finite Element Method is proposed to optimize the sensor sensitivity. Such nummerical tools are a prerequisite to in silico design a biosensor system with a low limit of detection. Unlike some widely used approximations, the impact of the grating depth, shape, duty cycle, losses, and surface roughness can be taken into account.

Based on the previous simulations, optimized transducer chips were produced and the anticipated performance experimentally verified. Despite the fact that the theoretical foundations of the sensitivity of waveguide grating (bio)sensors are well-known and their implications anticipated by the scientific community for several decades, to our knowledge, no prior publication has experimentally confirmed waveguide sensitivity for multiple film thicknesses, wavelengths, and polarization of the propagating light. In the second part of the thesis, the sensitivity versus waveguide thickness of said refractometric sensors is experimentally confirmed and compared with

Summary

....

predictions based on established theory. The effective refractive indices and the corresponding sensitivity were determined via the sensors' coupling angles at different cover refractive indices for transverse electric as well as transverse magnetic polarized illumination at various wavelengths in the visible and near-infrared. A good agreement between the measured data and the numerical simulations confirms the correctness of the theory.

In the thesis' main chapter, I present the first fully integrated, label-free optical biosensor system ARGOS (angle interrogated optical sensor), which relies on the optimized optical transducers as introduced in the previous sections and on a MEMS micro-mirror to interrogate said waveguide grating regions at a high repetition rate by scanning the angle of the incident coherent light. The tunable MEMS mirror permits an extended angle scanning range and offers the flexibility to measure at various wavelengths and optical powers. An excellent refractometric sensitivity with a detection limit of $\Delta n_{eff} < 2\text{x}10^{-7}$ and long-term stability ($<10^{-6}$/min) is reported, as well as the capability to perform affinity measurements for large (>150 kDa) and small (<250 Da) molecules. The fully-integrated, compact, low-power and affordable sensor unit is well-suited for in-situ environmental monitoring or point-of-care diagnostics.

As a conceptual outlook, the last part of the thesis introduces a novel approach of a resonant, dielectric waveguide sensor based on distributed Bragg gratings. The refractive index sensitive optical transducer aims at improving the performance of common planar waveguide grating sensor systems with limited Q-factor and dynamic range. This is achieved by combining the advantages of resonant cavities, such as a multitude of resonance peaks with high finesse, with the manageable complexity of waveguide grating couplers. The presented Fabry-Pérot type distributed Bragg resonator exhibits an extended measurement range (> 500 %) as well as relaxed fabrication tolerances. The chapter's appendix discusses the production and characterization of first sensor prototypes on a proof of concept level and provides recommendations for future sensor developments.

....

Zusammenfassung

Label-freie optische Biosensoren sind wichtige Werkzeuge um die Kinetik, Interaktion und Konzentration von (bio)chemischen Stoffen in verschiedenen Gebieten wie Biotechnologie, Pharmazie, Diagnostik sowie für in-situ Messungen in der Umweltanalytik zu studieren. Das Ziel dieser Dissertation ist es, einen umfassenden Überblick über die verschiedenen Schritte, das heisst vom Entwurf, zur Entwicklung bis hin zum Testen eines vollintegrierten Biosensor-Systems, zu geben.

Planare optische Wellenleiter mit Gitterkoppler sind hochsensitive Sensorstrukturen und sind daher interessant, da sie eine Vielzahl an Parametern aufweisen, welche für die Entwicklung des Sensor-Chips optimiert werden können. Im ersten Teil dieser Dissertation wird ein Algorithmus eingeführt, welcher auf einer Kombination der Transmission Line Transfer Matrix und Finite Elemente Methode beruht. Solche numerischen Werkzeuge sind eine Grundvoraussetzung um hochempfindliche Biosensorsysteme mit einer tiefen Nachweisgrenze zu entwickeln. Im Gegensatz zu anderen Methoden erlaubt das hier vorgestellte Verfahren die Berücksichtigung der Gittertiefe und -form, des Füllfaktors, der Verluste sowie der Oberflächenrauheit.

Basierend auf diesen Simulationen wurden optimierte Sensorchips hergestellt und die errechneten Empfindlichkeiten experimentell verifiziert. Obwohl die theoretischen Grundlagen bezüglich der Sensitivität von Gitterkopplern bestens verstanden und der wissenschaftlichen Gemeinschaft seit mehreren Jahrzehnten bekannt sind, hat noch keine vorangehende Arbeit die Sensitivität von optischen Wellenleitern für verschiedene Schichtdicken, Wellenlängen und Polarisationen experimentell nachgewiesen. Diese Lücke wird im zweiten Teil der Disserta-

tion anhand von experimentellen Messungen bezüglich der refrakto-metrischen Sensitivität geschlossen und mit der gängigen Theorie verglichen. Hierzu wurden die effektiven Brechungsindizes und die daraus resultierenden Sensitivitäten anhand der Kopplungswinkel bei verschiedenen Brechungsindizes des Cover-Mediums für transversal-elektrisch sowie transversal-magnetisch polarisiertes Licht unterschiedlicher Wellenlängen gemessen. Die gute Übereinstimmung der gemessenen und simulierten Daten bestätigt die Gültigkeit der Theorie.

Im Hauptteil dieser Arbeit wird das vollintegrierte, label-freie optische Biosensorsystem ARGOS (angle interrogated optical sensor) vorgestellt. Das neuartige Messprinzip basiert auf den zuvor optimierten Gitterkopplern sowie auf einem MEMS Mikrospiegel zur schnellen Auslese der Sensorflächen durch Scannen des Einfallswinkels des kohärenten Lichts. Wesentliche Vorteile des MEMS Spiegels sind ein erweiterter Messbereich sowie die Möglichkeit das System mit unterschiedlichen Wellenlängen und optischen Leistungen zu betreiben. Es wird eine ausgezeichnete refraktometrische Sensitivität und Detektionslimite von $\Delta n_{eff} < 2 \times 10^{-7}$ und Langzeitstabilität ($< 10^{-6}$/min) berichtet, sowie die Fähigkeit aufgezeigt, Affinitätsmessungen mit grossen (>150 kDa) sowie kleinen (< 250 Da) Molekülen durchzuführen.

Der letzte Teil der Dissertation stellt schliesslich ein neuartiges Konzept eines resonanten, dielektrischen Wellenleitersensors vor, welches auf Distributed Bragg Gratings beruht. Der brechungsindexsensitive optische Sensor zielt darauf ab, die Eigenschaften von planaren Gitterkopplern mit limitiertem Q-Faktor und Messumfang zu verbessern. Dies geschieht durch die gezielte Kombination der jeweiligen Vorteile von Resonator-basierten Sensoren, wie zum Beispiel die Vielzahl von resonanten Moden mit hoher Finesse, mit der relativ geringen Komplexität von Gitterkopplern. Im Gegensatz zu einfachen Bragg Reflektoren besitzt der vorgestellte Fabry-Pérot Resonator einen ausgedehnten Messbereich (> 500 %) sowie gelockerte Fabrikationstoleranzen. Im Kapitelanhang werden die Produktion und Charakterisierung erster Sensorprototypen aufgezeigt, sowie Vorschläge für zukünftige Sensorentwicklungen besprochen.

A

A........................ sensor area

ADC.................... analogue-to-digital converter

AFM.................... atomic force microscopy

Al_2O_3 .... aluminium oxide

ARGOS.............. angle interrogated optical sensor

ARROW .... anti-resonant reflecting optical waveguide

C

C........................ cover layer

c .... speed of light

CAII.................... carbonic anhydrase II

CC...................... constant current

CCD.................... charge-coupled device

CMOS .... complementary metal-oxide-semiconductor

CMT .... coupled mode theory

CP .... constant power

CPU .... central processing unit

CTI...................... commission for technology and innovation

D

D .... duty-cycle

d........................ resonator length

Da .... Dalton

DBR.................... distributed Bragg resonator

DIO.................... digital inputs/output

DPSS.................. diode pumped solid state (laser)

E

E........................ electric field

EDC .... N-ethyl-N'-(dimethylaminopropyl) carbodiimide hydrochloride

EPDM................. ethylene propylene diene monomer

F

F .... film

$\mathcal{F}$ .... finesse

FBG.................... fiber Bragg grating

FBS..................... fetal bovine serum

f_c .... confidence factor

FEM .... finite element method

FoM.................... figure of merit

FPGA .... field programmable gate array

FRAM .... ferroelectric random access memory

FSR..................... free spectral range

FWHM............... full width at half maximum

G

GUI .... graphical user interface

H

H .... magnetic field

h_{ad} .... adlayer thickness

h_{eff} .... effective waveguide thickness

HEPES .... 4-(2-hydroxyethyl)-1-piperazineethanesulfonic acid

h_f .... waveguide film thickness

List of Abbreviations and Symbols

h_{fmin} .... cut-off thickness
h_r .... rib height

I

I .... intensity
IgG .... immunoglobulin G

K

k .... wave vector
kDa .... kilodalton
kHz .... kilohertz
k_{wg} .... waveguide extinction coefficient

L

L .... interaction length
L_{eff} .... effective grating length
L_g .... grating length
LIME .... local interference method
LoD .... limit of detection

M

m .... mode number
M .... molar
$\mathcal{M}$ .... surface mass
MEMS .... micro-electro-mechanical system
MES .... 2-(N-morpholino) ethane sulfonic acid
m_g .... diffraction order
MHz .... megahertz
m_{wg} .... waveguide mode number

N

n_{ad} .... adlayer refractive index
n_{air} .... refractive index of air

n_c .... cover refractive index
n_{eff} .... effective refractive index
n_f .... waveguide film refractive index
NHS .... N-hydroxysuccinimide
nm .... nanometer
n_s .... substrate refractive index
n_{water} .... refractive index of water

O

OWLS .... optical waveguide light mode spectroscopy

P

P .... power
PBS .... phosphate-buffered saline
PEEK .... polyether ether ketone
pg .... pictogram
PLL-g-PEG .... poly(L-lysine)-g-poly(ethylene glycol)
pm .... picometer
PML .... perfectly matched layer
POM-C .... polyoxymethylen copolymer
PPMCC .... Pearson product-moment correlation coefficients
PTFE .... polytetrafluoroethylene

Q

Q(-factor) .... quality factor
q_b .... Bragg order

R

R .... reflectance
RAM .... random access memory
RIE .... reactive ion etching
RifS .... reflectometric inter-ference spectroscopy
RMS .... root-mean-square
RMSD .... root-mean-square deviation

S

s .... sensitivity
S .... substrate
SBSR .... sensing layer to bulk volume signal ratio
Si_3N_4 .... silicon nitride
SiO_2 .... silicon dioxide
SiO_xN_y .... silicon oxynitride
SNR .... signal-to-noise ratio

T

t .... time
T .... transmission coeffi-cient
Ta_2O_5 .... tantalum pentoxide
TE .... transverse electric
TiO_2 .... titanium dioxide
TLTMM .... transmission line transfer matrix meth-od
TM .... transverse magnetic

U

UV .... ultraviolet

V

VCSEL .... vertical-cavity sur-face-emitting laser

v_p .... phase velocity in the guided mode

W

W .... energy density
w .... rib/grating width
WIOS .... wavelength interro-gated optical sensor
wt% .... percentage by mass

αβγ

β .... propagation constant
Γ .... surface mass density
ΔM_{min} .... minimal detectable mass
Δn_c .... change in cover re-fractive index
Δz .... penetration depth
$\delta\lambda_{FWHM}$ .... spectral width
$\Delta\lambda_{shift}$ .... wavelength shift
$\Delta\lambda_{VCSEL}$ .... VCSEL tuning range
θ_a .... acceptance angle
θ_{scan} .... angular interrogation range
Λ .... grating period
λ .... wavelength
λ_b .... Bragg wavelength
ρ .... polarization
σ .... standard deviation
φ .... phase shift
φ_{fc} .... Fresnel shift at film-cover interface
φ_{fs} .... Fresnel shift at film-substrate interface
ω .... angular frequency

List of Abbreviations and Symbols

....

....

XIV

1 Introduction to Integrated Planar Waveguide Biosensors[*]

1.1 Preface

Due to the cumulative nature of this thesis with individual, self-contained contributions, this introduction aims at covering propaedeutic aspects not discussed in the latter. After briefly reviewing the history of biosensing, the reader will be familiarized with the basic concepts and theory of integrated optics, which is not explicitly covered in the subsequent, published chapters. Albeit of crucial importance for the understanding of the entire thesis, consolidated knowledge in waveguide optics will mainly facilitate the reading of the more theoretical Chapters 3 and 4. Towards the end of this chapter, an overview of various label-free sensor principles previously introduced to the scientific community as well as commercially available systems will be provided. This historical review of optical biosensors and the compilation of various interrogation schemes will allow the reader to comprehend the practical implementations required and the features desired for the conceptualization of novel, integrated sensor system principles as introduced in Chapters 5 and 6. The content, objective and outcome of the individual chapters, as well as their relation, will be outlined in Chapter 2.

---

[*] Parts of this chapter are published in: P. Kozma, F. Kehl, E. Ehrentreich-Förster, C. Stamm, and F. F. Bier. Integrated planar optical waveguide interferometer biosensors: A comparative review, *Biosensors and Bioelectronics*, **58**. 287–307, (2014).

1.2 Background

With the development of the enzyme electrode in 1962, Clark and Lyons[1] presented the first biosensor and hereby demonstrated its huge prospects in medicine and biotechnology. With this achievement, they started a continuous and ongoing development process within the field of biosensing[2]. Although, during the past more than 50 years, numerous new sensor designs with better and better properties have been published and commercialized, the need for decreasing size and cost, but improving sensitivity, detection limit, specificity and stability still challenges today's scientists and engineers. Miniaturized, fast, cheap, easy-to-use and reliable glucose biosensors already make the life more comfortable and safe for those, who are suffering from diabetes[3]. Beyond the biomedical applications of e.g. pregnancy, bacterial infection, cholesterol and troponin T quick tests[4,5], the new approaches of biosensorics open up new opportunities; they are e.g. widely used in forensic medicine (alcohol, drug, doping tests, etc.) and industry (pharmaceuticals, water-, food quality, etc.), as well[6–8]. The sensitive and specific detection of biological substances of molecular weights of even less than 500 Da at a concentration of typically less than a few pg/ml, is still not trivial today in a sample, where numerous other molecules may also be present dissolved in a significantly larger quantity[9]. The interest in reliable and cost-effective transducers, namely biosensors, which are able to convert the recognition of these tiny biological entities, i.e., targets to an amplified signal, still remains[10].

Today, the most sensitive biosensors are based on fluorescent, radioactive or magnetic labelling, since following the signal produced by the label, the binding or the presence of even an individual molecule can be detected in the observed volume or on the studied surface[11,12]. Beyond this indubitable advantage, unfortunately, they are suffering from numerous drawbacks compared to label-free techniques. For instance, the chemical procedure of labelling is rather expensive, time and labour intensive. The number of fluorophores on the molecules cannot be controlled precisely, which leads to a fluorescence signal bi-

as. Furthermore, the presence of these anchored tags could have a not-negligible effect on the molecules, thus on the experimental results, as well[7,13]. As a consequence, the label-free techniques are very important mates of labelling ones. Moreover, they have better future perspectives since they offer sensitive, specific and fast measurements without the above-mentioned drawbacks. By immobilizing recognition elements and by mounting a flow-cell onto a label-free sensor chip, quantitative, in situ and real-time detection of the target molecules or kinetic measurements of molecular interactions is possible.

Regarding the competition of label-free signal transducers such as mass-sensitive, temperature-sensitive, electrochemical and optical biosensors, the optical methods are dominating both the research literature and the market[14,15]. The reason is mainly that optical methods are merging the advantages of other label-free techniques into a cost-effective way. The binding of the target analytes is detected in their natural form using low-power electric field in or close to the visible range with neither destructive nor considerable manipulative effect on the experiment. The sampling rate and the detection limit of surface mass density changes are outstandingly good, which allows a very efficient real-time monitoring. In most cases, performing parallel measurements is straightforward due to their ability of multiplexing for multi-parameter analysis[9]. The technological demands for the fabrication of these transducers are relatively low and by batch manufacturing the optical elements in a more cost-effective and more compact way, their ongoing miniaturization leads to novel possibilities towards even lower reagent consumption, shorter analysis time and consequently towards point-of-care applications.

The working principle of these devices is depicted in Figure 1.1 and can briefly be summarized as follows: binding target molecules with higher refractive index are displacing the lower refractive index ambient (e.g. water or buffer) of the biological or biologically derived recognition elements, such as e.g. receptors, antibodies, aptamers, nucleic acids, enzymes or molecular imprints[2], which are integrated or associated with an optical signal transducer[16]. As a consequence, the

value of this physical parameter is changing locally, which has an effect on the related optical quantities, such as e.g. phase velocity of the propagating electromagnetic wave, polarization state, light intensity and wavelength[7,9]. The optical signal transducer amplifies this variation to a measurable, typically electric signal.
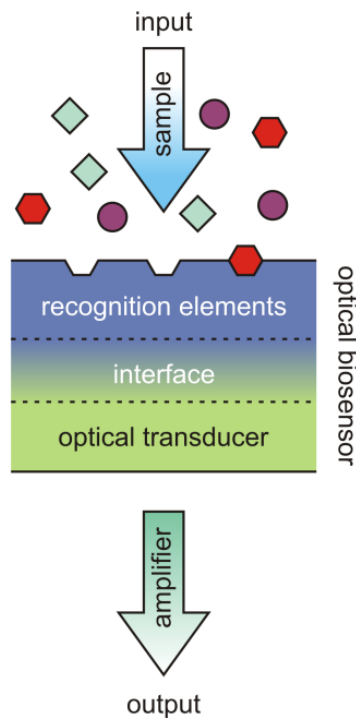

Figure 1.1: Schematic working principle of label-free optical biosensors. Surface immobilized recognition elements specifically bind the sample of interest; commonly one or several target molecules within a complex sample. The resulting mass adsorption and displacement of the surrounding medium results in a change of the local refractive index at the sensor surface. This variation has a direct effect on the physical properties of the interrogating electromagnetic wave, which can be amplified by the optical transducer.

1.3 Wave Propagation in Planar Optical Waveguides

The first demonstration of waveguiding is usually related to John Tyndall. However, Jean-Daniel Colladon has presented his "light fountain" earlier in 1842[17,18]. His experiment revealed that due to total internal reflection, the light can be guided in a transparent material, of

which refractive index is higher than that of the surrounding ambient. This phenomenon has later been exhausted in many applications of the optical waveguides amongst others in telecommunication and sensor devices, in which the confinement and guidance of electromagnetic waves along an arbitrary but defined path in space is the basis of performance.

A group of optical waveguides, the so-called planar optical waveguides can be regarded as a by-product of two industry branches, namely the telecommunication and semiconductor industries. Whereas the former led to novel methods to couple, transfer, switch, multi- and demultiplex light in optical fibers for high-speed communication, the latter can be accounted for developing the technologies to master the fabrication of complex, miniature integrated optical systems on a wafer level[19]. In their simplest form, planar optical waveguides consist of a three-layer structure, in which a thin film *(F)* of thickness h_f is sandwiched between a substrate *(S)* and a cover medium *(C)*. The refractive indices of the layers are n_f, n_S and n_C, respectively. As it is depicted in Figure 1.2, light can be guided in the (waveguide) film by total internal reflection, if the refractive index of the film is higher than those of the surrounding media *($n_C < n_f > n_S$)* and if the angle of light propagation relative to the interface normal is larger than the critical angles at the two boundaries *($\theta_{crit} = arcsin(n_{S,C}/n_f)$)* based on Snell's law[20]. Nevertheless, waveguide modes can arise and propagate through the film without any loss of power (in ideal case, when no scattering and absorption occurs), if h_f is larger than a minimum or "cut-off" thickness, h_{fmin}, which is a function of the abovementioned waveguide parameters, its mode number and the applied wavelength[21], and if the light rays reflected from the interfaces achieve constructive interference. As a consequence of the latter, only a discrete set of waveguiding states, i.e., of guided modes, exists in a planar waveguide configuration. This is the so-called self-consistency criterion of the classical "zig-zag" model interpretation[22]. It is important to note that if these constraints are not fulfilled, the guiding of the waves confined in the film cannot be performed and only radiation modes can be observed[23].
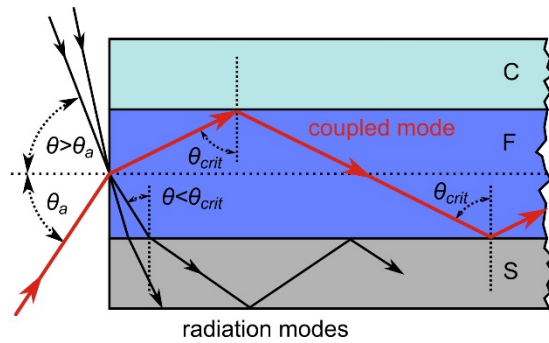
Figure 1.2: Light propagation in a planar optical waveguide. Light can be coupled and guided in a waveguide if $n_C < n_f > n_S$ and if the angle of light propagation relative to the interface normal is larger than the critical angle θ_{crit}. Light entering the waveguide under an angle that is bigger than the acceptance angle θ_a will lead to radiation modes and will be lost.

To get a deeper insight into this phenomenon, it is better to apply Maxwell's equations and the proper boundary conditions for homogeneous, stationary, non-magnetic, source-free and non-conducting layers of a configuration written above. As it is discussed by Jackson[20], on the one hand, important consequences of the boundary conditions are not only Snell's law and that the wave vector of original, refracted and reflected plane waves must lie in a plane, but also that the tangential component of a wave vector across an interface is continuous. This criterion defines a quantity, the effective refractive index $n_{eff} = k_t / k_0$ for planar waveguides $(n_S, n_C < n_{eff} < n_f)$, where $k_t \equiv \beta$ is the tangential component of the wave vector, the so-called propagation constant. It reflects that n_{eff} can be also introduced as $n_{eff} = c_0 / v_{mode}$, where $v_{mode} = \omega/\beta$ is the phase velocity of the guided mode, c_0 is the speed of light in vacuum and ω is the angular frequency of the guided light. On the other hand, in case of planar waveguides, the plane wave solutions of Maxwell equations divide themselves into two orthogonal sets of functions. Modes with only two different polarizations can be excited; either the total electric or the total magnetic field is oscillating in the plane of the interfaces (Figure 1.3). These polarizations are denoted consequently as transversal electric (TE) and transversal magnetic (TM) modes, respectively[22]. Let us consider a general orthogonal coordinate system, where the modes are propagating along

the z axis. Furthermore, the x and y axes are perpendicular and parallel to the interfaces, respectively. Based on the definition of TE and TM modes, we conclude that for $\underline{E}$ electric and $\underline{H}$ magnetic fields and consequently for the boundary conditions:

TE: $E_x = 0, E_z = 0, H_y = 0, k_y = 0$ thus

$E_y, H_z, \dfrac{\partial E_y}{\partial x}$ are continuous.

(1.1a)

TM: $E_y = 0, H_x = 0, H_z = 0, k_y = 0$ thus

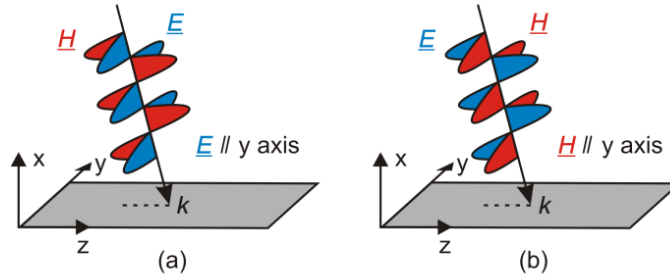$E_z, H_y, \dfrac{\partial H_y}{\partial x}$ are continuous.

(1.1b)

Figure 1.3: Visualization of (**a**) TE and (**b**) TM modes. In planar optical waveguides, modes with only two different polarizations can be excited; either the total electric or the total magnetic field is oscillating in the plane of the interfaces. These are the TE and TM modes, respectively.

Expressing Helmholtz' wave equation[20] for these specificities, the following relationship can be revealed for the x component of the wave vector in the substrate, film and cover layers of a planar optical waveguide:

$$k_{x,X} = \pm k_0 \sqrt{n_X^2 - n_{eff}^2}$$

(1.2)

where X denotes S, F or C, respectively. In case of isotropic media, n_X is a single constant value, and the solution of Equation (1.2) is independent of TE and TM polarizations. In case of anisotropic media, n_X is orientation dependent. Consequently, it is a matrix, which results in different solutions for TE and TM polarizations. A detailed description of ani-

sotropy can be found in Refs. 24,25. Corresponding to Equation (1.2), the total electromagnetic field inside the waveguide film is given by the linear combination of an upwards, $\underline{U}^+(x,z,t)$, and a downwards, $\underline{U}^-(x,z,t)$, propagating wave:

$$\underline{U}(x,z,t) = \underline{U}^+(x,z,t) + \underline{U}^-(x,z,t)$$

$$= \left(\underline{U}_0^+ \, e^{ik_x(x-x_0)+\varphi^+} + \underline{U}_0^- \, e^{-ik_x(x-x_0)+\varphi^-} \right) e^{in_{eff}k_0 z - i\omega t}$$

(1.3)

where $\underline{U} = \underline{E}, \underline{H}$ and $\underline{U}_0 = \underline{E}_0, \underline{H}_0$. (It is visualized in Figure 1.4) Considering Equations (1.2) and (1.3) it can be seen that the amplitude of the propagating waves attenuates exponentially outside of the waveguide film in the function of the distance measured from the nearest interface, since k_x becomes imaginary in the substrate as well as in the cover media. This exponentially decaying electromagnetic field is the so-called evanescent field. The penetration depth of the evanescent field (with other words the decay length of the field strength) can be gained by expressing Equations (1.2) and (1.3) for the cover layer:

$$\delta_{x,C} = \left(k_0 \sqrt{n_{eff}^2 - n_C^2} \right)^{-1}$$
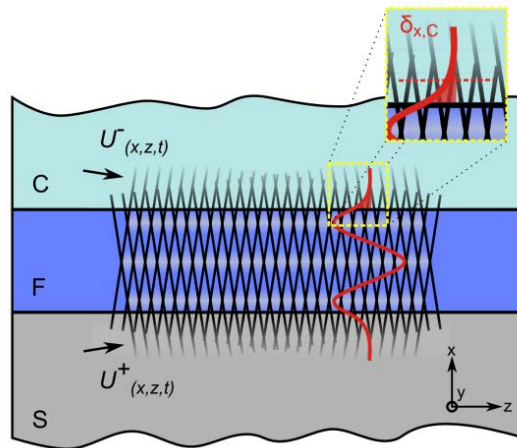
(1.4)

Figure 1.4: Visualization of mode formation in a planar optical waveguide. The total electromagnetic field inside the waveguide film is composed by the superposition of an upwards, $\underline{U}^+(x,z,t)$, and a downwards, $\underline{U}^-(x,z,t)$, propagating wave. Here, a mode of order 2 is depicted. The evanescent field with the penetration depth $\delta_{x,C}$ is magnified in the inset.

Applying Equation (1.3) at the film/substrate and film/cover interfaces, where $x = x_0$ and $x = x_0 + h_f$, respectively, the ratios of the upwards and downwards traveling waves can be written in the form of the (complex) Fresnel reflection coefficients, r_S and r_C, at the two interfaces:

$$r_S = \frac{\underline{U}_0^+}{\underline{U}_0^-} = |r_S|e^{i\varphi_S} \quad at \ x = x_0 \tag{1.5}$$

$$r_C = \frac{\underline{U}_0^- e^{-ik_x h_f}}{\underline{U}_0^+ e^{ik_x h_f}} = |r_C|e^{i\varphi_C} \quad at \ x = x_0 + h_f \tag{1.6}$$

where φ_S and φ_C are phase shifts due to the reflection from the interfaces. The reflection coefficients can be expressed by the parameters of the waveguide, as well, as it is described in more detail in the given ref. 24. It is important to emphasize that they are different for TE and TM modes; consequently, TE and TM wave propagations can be performed under different conditions (also in case of isotropic media). Inserting Equation (1.5) into (1.6), the mode equation can be gained as:

$$r_S r_C e^{2ik_x h_f} = |r_S||r_C|e^{i(\varphi_S + \varphi_C + 2k_x h_f)} = 1 \tag{1.7}$$

which can be rewritten in order to conclude to the classical mode equation:

$$2h_f k_x - \varphi_S - \varphi_C = 2\pi m \tag{1.8}$$

where $m = 0, 1, 2, ...$ is the mode order. As it is demonstrated, due to the cross-sectional size and shape of the waveguide, only discrete electromagnetic field distributions characterized with $n_{eff,m}$ or β_m (see Equation (1.2)) can be guided, because only these satisfy the boundary conditions. Figure 1.5 depicts the field distribution profiles of the first four modes, i.e., TE_0, TM_0, TE_1 and TM_1 in planar optical waveguides. The number of modes of different orders is also determined by the opto-geometrical parameters. The orders are counted from zero referring to the shape of the wave fronts[22]. The number of guided modes decreases with h_f and refractive index contrast between film and surrounding or with increasing wavelengths. Waveguide films not supporting any

modes are below h_{fmin} for a given wavelength, or vice-versa, a certain wavelength is below a distinct value determined by the cut-off frequency for a given waveguide configuration and mode[20]. In a special case, when h_f is chosen to be slightly thicker than h_{fmin}, only the fundamental TE_0 and TM_0 modes can be excited and the waveguides are commonly called single-mode waveguides[22]. In a typical dielectric single-mode waveguide, h_f is about 100 – 200 nm.
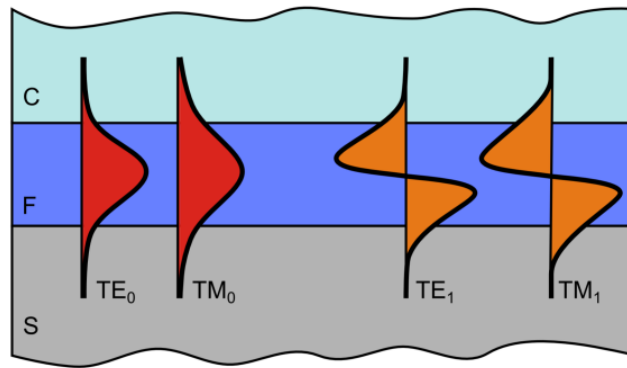

Figure 1.5: Schematic visualization of the waveguide modes in a planar optical waveguide. The field distribution profile of the modes $m = 0$ (red) and 1 (orange) for TE and TM polarizations are presented, respectively. As it is depicted, TM modes interrogate deeper into the surrounding media than TE modes.

1.4 Waveguide Types and Light Coupling Techniques

Planar optical waveguides exist in various configurations differing in both material as well as geometry, since their technology offers a great flexibility and variability in sensor design, production and optimization[26]. Generally, planar waveguides deposited on a stable and thin substrate, which is typically made of low refractive index and glassy materials (e.g. SiO_2 or polymers), can be classified into two types regarding their geometrical design, namely slab waveguides and channel waveguides[27]. It is important to note that the theory of planar optical waveguides introduced in the previous sub-chapter is exact for slab waveguide modes and is a very good approximation for channel ones[26]. Slab waveguides are structures with a planar geometry, which

guide light in only one transverse direction as lateral modes become effectively infinite[28]. Besides the relatively easy fabrication, another benefit of the slab waveguide is the absence of scattering between the transverse and lateral modes. Contrary to the slab waveguides, channel waveguides act as a conduit for the light in both transverse directions with a two-dimensional optical confinement. Channel waveguides can be further divided into buried channel, strip-loaded, diffused, ridge and rib waveguides (Figure 1.6) and are microfabricated by embossing or conventional photolithographic means[19]. A buried waveguide is embedded in the substrate and completely surrounded by the cladding material and therefore not a suitable configuration for the sensitive area of the interferometer, but it is commonly used to guide the light from and to the latter. Another method to form a waveguiding channel is to load a dielectric strip on top of a slab waveguide. This induces a localized difference in the underlying effective refractive index and is known as strip-loaded waveguide. Again, due to the shielding cover cladding, this configuration is not beneficial for biosensing applications. A third method to form a laterally confined waveguide is the diffused waveguide, which is formed by indiffusion of foreign atoms or by ion exchange. In the field of planar optical interferometric waveguide biosensors, the ridge and the rib waveguides are the most common of their kind, whereas the former is a fully, the latter a partly freestanding channel structure on top of a supporting substrate. An alternative rib waveguide configuration is the anti-resonant reflecting optical waveguide (ARROW) fabricated with standard integrated circuit technology[29–31]. In an ARROW waveguide, the light is confined in a waveguide rib, which is separated from a semiconductor substrate with two interference layers. The light confinement is based on total internal reflection at the ambient-waveguide film interface and on high anti-resonant reflection (>99.9%) from the interference cladding layers. The interference layers behave as a Fabry–Pérot resonator, consequently, single-mode behaviour is guaranteed by loss discrimination of modes higher than the fundamental[32]. The advantages over the conventional total internal reflection waveguides include the greater film thickness, the

greater freedom regarding their fabrication parameters and the lower insertion losses[32].
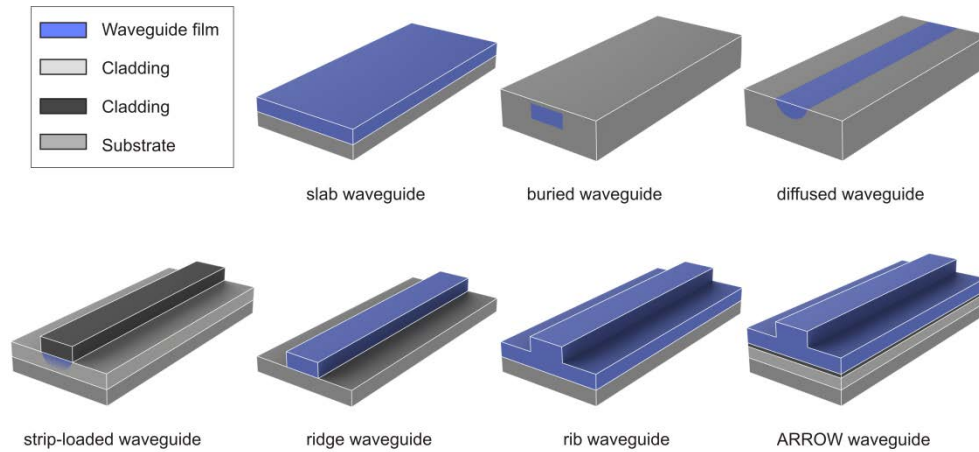

Figure 1.6: Schematic 3-dimensional representation of different waveguide types. In the interest of an easier comparison, the same functional layers are marked with same colours (see the inset in the upper left corner).

Depending on their refractive index profiles, both categories can be divided into three sub-groups, namely step-index, graded-index and photonic crystal waveguides. Step-index waveguides exhibit an abrupt refractive index step at the substrate-waveguide and cover-waveguide transitions. Most commonly, a thin layer of a high refractive index material (e.g. Ta_2O_5, TiO_2, Si_3N_4, Al_2O_3 or SiO_xN_y) is deposited on the substrate[33]. In the case of a graded-index waveguide, the refractive index profile has a smooth transition between cover and substrate as they are fabricated by diffusive ion-exchange or more recently, written in glass by femtosecond laser pulses[34,35]. Contrary to step-index waveguides, only rather small refractive index contrasts can be achieved for graded-index waveguides and, therefore, exhibit a lower sensitivity[36]. Step-index and graded-index waveguides are depicted in Figure 1.7. Photonic crystal waveguides are composed of repetitive regions of low and high dielectric constants that affect the propagation of the electromagnetic waves by diffraction and interference effects[37].
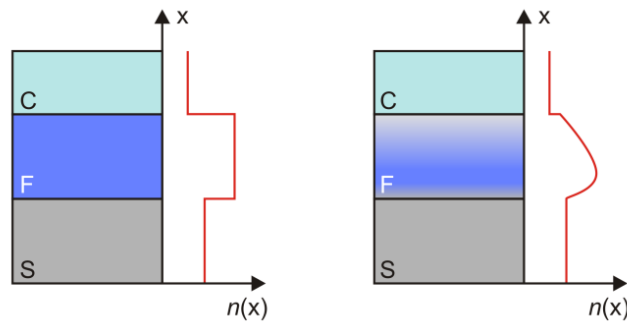
Figure 1.7: Step-index and graded-index waveguides. Step-index waveguides exhibit an abrupt refractive index step at the substrate and cover transitions, while the refractive index profile of graded-index waveguides has a smooth transition between them.

In waveguide applications, light from an external source needs first to be coupled into and subsequently out of the waveguide for detection. In general, five coupling methods can be differentiated as follows: free-space end-fire-, butt-end-, prism-, grating- and directional coupling (Figure 1.8). The reader is referred to specialized books for further literature on this topic[22,38].
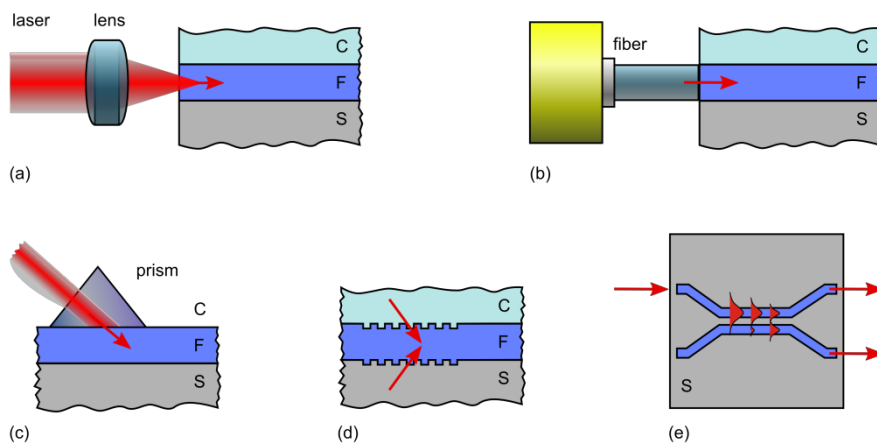

Figure 1.8: Light coupling techniques for optical waveguides: (a) end-fire coupling, (b) butt-end coupling, (c) prism coupling, (d) grating coupling and (e) directional coupling.

In the case of free-space end-fire coupling, the illumination light is directly focused on a cleaved edge face of the waveguide. It can be regarded as the most common and simplest way to couple a free-

space source into a waveguide. However, for efficient coupling, the end faces must be extremely smooth and the numerical aperture of the focusing lens needs to be fitted to the propagation constant of the mode excited in the waveguide film. Moreover, the precise alignment of the impinging beam relative to the waveguide is of crucial importance for high coupling efficiency and makes high demands on the positioning devices and their mechanical stability, especially for thin single-mode waveguides.

The closely related concept of butt-end coupling brings an optical fiber in direct contact (often via immersion oil) with the cleaved edge face of the waveguide. Advantageous is the fact that two physical units need to be aligned and brought in contact, which is generally easier than the alignment of a light cone (especially for wavelengths beyond the visible spectrum) and can be done under a microscope or even with fiber guiding alignment grooves. Similarly to end-fire coupling, the alignment is crucial as well as the mode matching between the two waveguides for the efficient coupling. Further difficulties of the butt-end approach are the presence of immersion oil (if applied) and the fact, analogue to the chicken or the egg problem, that the light already needs to be coupled in the optical fiber.

In the case of directional coupling, channel waveguides are brought in close proximity so that a mode can be excited in a secondary waveguide via the evanescent field of a primary one[39]. In other words, one of the two waveguides acts as the source for the second one, whereby the amount of optical power transfer from the former to the latter can be adjusted by geometrical means like interaction length and their relative distance. The concept of directional coupling is mainly used for signal multiplexing or coupling into ring resonators, where this sophisticated and stable coupling mechanism is necessary, but it has the disadvantage that their production is technology-intensive and, analogue to the butt-end coupling, the light already needs to be coupled into one of the waveguides beforehand.

Another method to couple light into a waveguide is via prism coupling[40]. A high refractive index prism is either brought in direct contact with the waveguide by applying mechanical pressure or by the use of immersion oil. Illuminating the waveguide through the prism at an incident angle that matches the propagation constant of a guided mode, light can be coupled into but also extracted from the waveguide with high efficiency. The need for mechanical pressure or immersion oil and the direct contact of the prisms with the waveguide make these couplers unfavourable for sensing applications. In practice, this is because the applied pressure can lead to slight waveguide deformations, whereas the immersion oil may contaminate the waveguide surface. Additionally, the prism's physical size is disadvantageous in bioexperiments, since prism and flow-cell need to be mounted on the same side of the waveguide.

Waveguide grating couplers are periodic structures with an alternating effective refractive index, usually with a grating period in the range of half the wavelength of the coupled light[41–43] (Figure 1.9). The grating either consists of a periodically corrugated surface relief, realized by embossing or photolithographic processes or an alternating modification of the waveguide refractive index. The latter can either be achieved persistently by ion exchange or UV-induced refractive index modulation[44]. In general, both the coupling of an impinging coherent beam and conversion into a guided mode within the waveguide as well as the reciprocal process of coupling the light out of the waveguide by means of grating couplers is defined by the resonance condition:

$$n_{c/s} \cdot sin(\theta_c) = n_{eff} - \frac{m_g \lambda}{\Lambda} \qquad (1.9)$$

where θ_c is the coupling angle, m_g is the diffraction order, λ is the wavelength measured in free-space and Λ is the grating period. The grating acts as a diffractive element to achieve higher order diffraction angles within the waveguide, which fulfill the conditions of total internal reflection. Waveguide grating couplers offer various advantages compared to the abovementioned methods: First, free space coupling into

the expanded grating elements is rather easy, as only the coupling angle of a collimated beam needs to be adjusted. Second, contrary to the prism coupler, light can be coupled via both sides, via the substrate or the cover, of the waveguide. Since the fluidic chamber for the sample analysis is placed on the cover side of the waveguide sensor, hereby potentially obstructing the light, coupling via the substrate is commonly applied. Additionally, no immersion oil is needed. As drawbacks, it has to be mentioned that the production of waveguide gratings is technology-intensive and they are also sensitive to mechanical vibrations since the coupling efficiency is a very sensitive function of the angle of incidence[45].
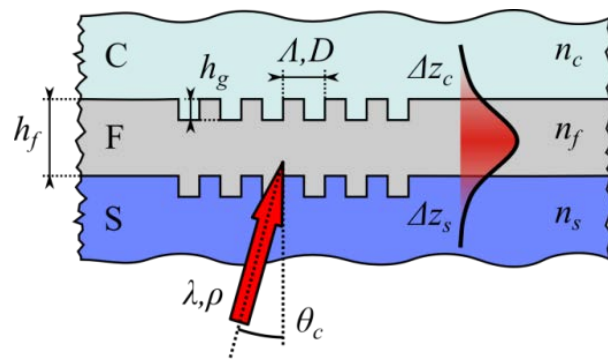

Figure 1.9: Schematic representation of a waveguide grating coupler, consisting of a substrate S, waveguide film F with a layer thickness of h_f and cover layer C with refractive indices n_s, n_f and n_c, respectively. A corrugated grating with a depth of h_g, period Λ and duty-cycle D acts as a coupling element for coherent light with wavelength λ, polarization ρ incident at an angle θ_c, thereby creating a guided mode with evanescent tails with penetration depths Δz_c and Δz_s.

1.5   Evanescent Field based Sensor Systems

Depending on the waveguide configuration, mode, wavelength and polarization, the penetration depth and hence the sensitive region of the waveguide usually extends 30 – 150 nm into the cover medium, but it can be increased even up to about 1 µm using reverse symmetry waveguides[46]. Whereas in optical fiber communication, it may be regarded as a parasitic effect, since the optical power of the propagating mode can be decreased by scattering of the field at the boundary

and/or by attenuation of the cladding, it allows waveguide sensors to investigate surface bound effects within the close proximity of the evanescent field.

As the evanescent electromagnetic field of the guided light penetrates slightly into the surrounding material, any refractive index change in the near-interface region has an effect on the value of n_{eff}. Cover refractive index changes in close proximity to the sensor surface, e.g. due to the adsorption of biomolecules with a different refractive index than the displaced water, will affect n_{eff}, which can directly be quantified via optical transducers. A brief overview on the different transducers introduced to the market as well as to the scientific community will be given in the following paragraph.

The most established label-free optical biosensors in scientific literature as well as on the market are surface plasmon resonance (SPR) based systems[13,15,47–50]. In contrast to dielectric waveguide sensors, SPR substrates are coated with an unstructured, thin metallic film (mostly Au, seldomly Ag). Resonance occurs when the k-vector of the impinging photons matches the natural frequency of the metallic layer's surface electrons. Analogous to waveguide-based optical transducers, the plasmonic resonance of the conduction band electrons is sensitive to refractive index changes close to the metallic surface and can, therefore, be used as a biosensor. Countless examples of commercial SPR systems are available on the market, but the latter is mainly dominated by the pioneer and world-leading company Biacore (Uppsala, Sweden), as well as Bio-Rad (Hercules, USA), IBIS (Enschede, The Netherlands), BioNavis (Ylöjärvi, Finland) and Horiba (Kyōto, Japan).

Besides SPR, various dielectric waveguide sensor systems with different configurations and interrogation schemes are commercially available, but again dominated by a few players: Corning's Epic® system (Corning, Inc., Corning, USA) employs spectral interrogation of waveguide gratings for high-throughput screening at the bottom of a 384-well plate, as well as the BIND™ platform from SRU Biosystems' (now X-BODY Biosciences, Woburn, USA). Other waveguide grating based sen-

sor systems have been commercialized by small and medium sized enterprises (SMEs) such as MicroVacuum's OWLS (Budapest, Hungary) with angular interrogation[45], Artificial Sensing Instruments (Zürich, Switzerland), the wavelength interrogated WIOS[51] sensor from CSEM SA (Neuchâtel, Switzerland) as well as the grating coupled interferometry[52] based WAVE system from Creoptix™ (Wädenswil, Switzerland). Whereas the latter representative combines grating couplers with highly sensitive interferometric readout, interferometry based sensor systems have been introduced to the market by Farfield's (Linthicum, USA) AnaLight® which roots on dual polarization interferometry[53,54], whereas FortéBio's (Menlo Park, USA) products rely on bio-layer interferometry[55].

Numerous other label-free, optical sensing concepts making use of waveguides have been featured in the scientific literature[56]. This non-exhaustive enumeration includes: Mach-Zehnder[57], Hartman[58] and Young interferometers[59–61], sophisticated micro-sphere, disc and ring resonators[62–64], reflectometric interference spectroscopy (RifS)[65], bidiffractive[66,67] and chirped grating couplers[68], resonant mirrors[69], anti-resonant reflecting optical waveguides (ARROW)[32], ellipsometry[70], photonic crystals[71], as well as focal molography[72]. Non-optical, surface sensitive label-free sensors such as surface acoustic waves (SAW)[73,74], quartz crystal microbalance (QCM)[75,76] and electro-chemical sensors[77] are also widespread and important tools to characterize and compare the performance of the purely optical transducers.

For a detailed explanation of the different, abovementioned sensing principles, the interested reader is advised to consult the referenced literature, as the scope of this thesis will solely be on planar waveguide grating sensors.

Based on the work of Tiefenthaler and Lukosz[78,79], it is well known that waveguide gratings cannot only be used as integrated optical elements to facilitate the coupling into and out of the waveguide, but they can also act as very sensitive transducers themselves. The literature on waveguide grating couplers and their application as label-free biosensors is vast. Various angular[45,78], as well as spectral[51,80] inter-

rogation schemes for both input[81] and output[82] grating couplers, have been realized. An overview can be found in Refs. 7,45,83–85, and a detailed introduction to the sensing principle and transducer structure will be given in the following.

1.5.1 Angular Interrogation

Waveguide grating sensors with angular read-out rely on a monochromatic, coherent beam at a constant wavelength λ, which couples into the waveguide via a first grating and subsequently couples out of the waveguide via a second grating. The in- and out-coupling angles θ_c are defined via Equation (1.9) and change due to any changes in the waveguide's effective refractive index n_{eff}. In the input configuration, the angle of the incident beam is constantly scanned around the coupling angle to determine the resonance condition and eventually n_{eff}. Light couples into the waveguide via the first grating if the resonance condition is fulfilled and couples out onto a simple photodiode via a second grating or end-fire coupling to determine the angle of maximum coupling[81,86]. In this case, the input grating acts as sensitive element (Figure 1.10, left). In the output configuration, the angle of the out-coupled beam is monitored by a position sensitive detector[82], as depicted in Figure 1.10, right.

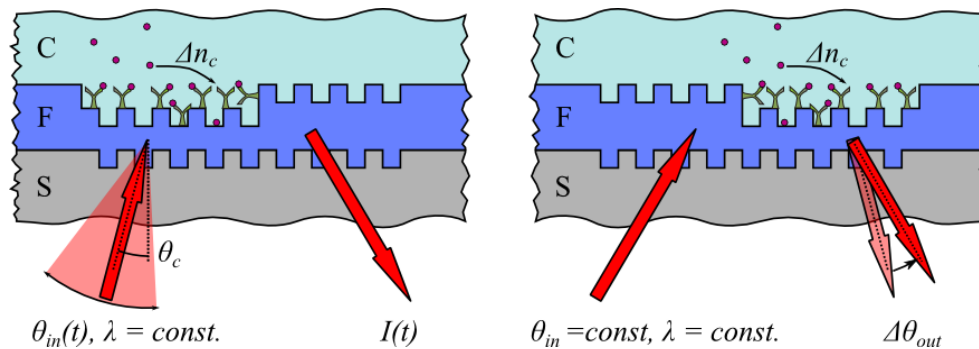**Figure 1.10:** Input (**left**) and output (**right**) configuration of angle interrogated waveguide grating sensors (Adapted from ref. 24).

The benefit of both angular configurations is the large measurement range and relatively simple implementation. In case of the input configuration, the mechanical movement of either the source or the chip itself limits both interrogation frequency as well as resolution.

An additional drawback is the involvement of moving parts. The output configuration is mainly limited by the size and resolution of the position sensitive detector, but does not require any moving elements.

1.5.2   Spectral Interrogation

Spectral interrogation of the input grating coupler is accomplished by constantly tuning the wavelength[51] of the incident beam while keeping the angle of incidence fixed. The out-coupled light is detected by a simple photodiode (Figure 1.11, left). Another approach to determine the effective refractive index is to analyze the out-coupled spectrum of a multichromatic[80], coupled light source (Figure 1.11, right). Similar to the angle interrogated output coupler, both spectral configurations do not require any moving parts. Wavelength interrogation can be accomplished by a relatively low-cost vertical cavity surface emitting laser diode (VCSEL) at high repetition rates.
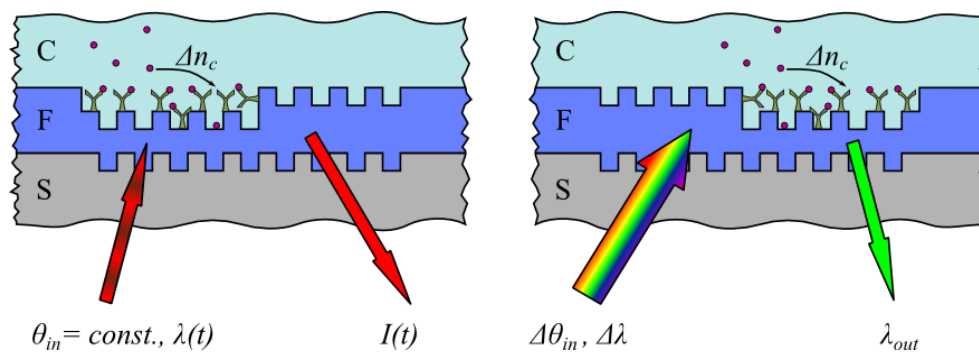

Figure 1.11: Input (**left**) and output (**right**) configuration of wavelength interrogated waveguide grating sensors (Adapted from ref. 24).

The disadvantage of this implementation is the VCSEL's relatively small spectral tuning range of approximately 2 nm, therefore limiting the measurement range of the sensor system. Additionally, the required single-mode VCSELs are limited in optical power and availability of wavelengths in the visible range. Lasers with a bigger tuning range are available, but in general costly. The second configuration is mainly limited by the spectral resolution of the detector. Optical spectrum analyzers with a big range and high resolution are commercially available, but expensive. Additionally, multiplexing (the read-out of several sensor pads in parallel) is limited to the number of spectrometers.

The countless configurations and read-out schemes reveal a common advantage of integrated optical waveguide sensors over SPR and other devices, namely the enhanced degree of freedom for transducer and reader design. Waveguide gratings possess a multitude of tuning parameters for waveguide (material, thickness), grating (period, depth, duty-cycle, shape) as well as for the interrogation of the latter (wavelength, polarization, angular/spectral read-out). Additionally, the transparent dielectric material is suitable for parallelized or subsequent signal verification by fluorescent means.

While *"standing on the shoulder of giants"* [†], the goal of this thesis was to combine and extract the common advantages of the presented sensor systems, while exploring the potential for the integration of novel technical achievements either not available or not affordable in the past decade. Recent developments in integrated optics and electronics, lasers as well as micro-electromechanical-systems (MEMS) allow for miniaturized, compact systems with increased computational power at lower energy expenses, paving the way for fully-integrated, affordable biosensors for in-situ measurements for environmental monitoring or point-of-care diagnostics. A detailed scope of the thesis will be given in the subsequent chapter.

1.6   References

1.   Clark, L. C. & Lyons, C. Electrode Systems for Continuous Monitoring in Cardiovascular Surgery. *Ann. N. Y. Acad. Sci.* **102,** 29–45 (1962).

2.   Chambers, J. P., Arulanandam, B. P., Matta, L. L., Weis, A. & Valdes, J. J. Biosensor Recognition Elements. *Curr. Issues Mol. Biol.* **10,** 1–12 (2008).

3.   Oliver, N. S., Toumazou, C., Cass, A. E. G. & Johnston, D. G. Glucose sensors: a review of current and emerging technology. *Diabet. Med.* **26,** 197–210 (2009).

[†] Bernard of Chartres, 12th century (The Metalogicon of John Salisbury. University of California Press. p. 167).

1.6 References

4.   Holford, T. R. J., Davis, F. & Higson, S. P. J. Recent trends in antibody based sensors. *Biosens. Bioelectron.* **34,** 12–24 (2012).

5.   Justino, C. I. L. L., Rocha-Santos, T. a. & Duarte, A. C. Review of analytical figures of merit of sensors and biosensors in clinical applications. *Trac-trends Anal. Chem.* **29,** 1172–1183 (2010).

6.   Alocilja, E. C. & Radke, S. M. Market analysis of biosensors for food safety. *Biosens. Bioelectron.* **18,** 841–846 (2003).

7.   Fan, X. *et al.* Sensitive optical biosensors for unlabeled targets: A review. *Anal. Chim. Acta* **620,** 8–26 (2008).

8.   Klenkar, G. & Liedberg, B. A microarray chip for label-free detection of narcotics. *Anal. Bioanal. Chem.* **391,** 1679–1688 (2008).

9.   Cunningham, B. T. in *Label-Free Biosensors: Techniques and Applications* 300 (2009).

10.   Kozma, P. *et al.* A novel handheld fluorescent microarray reader for point-of-care diagnostic. *Biosens. Bioelectron.* **47,** 415–420 (2013).

11.   Alivisatos, A. P. Less is more in medicine. *Sci. Am.* **285,** 66–73 (2001).

12.   Jain, K. K. Nanotechnology in clinical laboratory diagnostics. *Clin. Chim. Acta* **358,** 37–54 (2005).

13.   Cooper, M. a. Optical biosensors in drug discovery. *Nat. Rev. Drug Discov.* **1,** 515–528 (2002).

14.   Lazcka, O., Del Campo, F. J. & Muñoz, F. X. Pathogen detection: a perspective of traditional methods and biosensors. *Biosens. Bioelectron.* **22,** 1205–17 (2007).

15.   O'Malley, S. in *Protein Biosynthesis* 1–33 (2008).

16.   Turner, A. P. F. Biosensors-Sense and Sensitivity. *Science.* **290,** 1315–1317 (2000).

17.   Colladon, D. Sur les réflexions d'un rayon de lumière à l'intérieur d'une veine liquide parabolique. *Comptes Rendus* **15,** 800 (1842).

18.   Hecht, J. *City of light: the story of fiber optics.* (Oxford University Press, New York, 1999).

19.   Anderson, D. in *Optical and electro-optical information processing* (ed. Tippett, J. (Ed. .) 221–234 (M.I.T. Press, Cambridge, 1965).

20.   Jackson, J. D. *Classical Electrodynamics*. (John Wiley & Sons, Inc., 1998).

21.   Lukosz, W. Integrated optical chemical and direct biochemical sensors. *Sensors and Actuators B: Chemical* **29,** 37–50 (1995).

22.   Teich, M. & Saleh, B. Fundamentals of photonics. *Canada, Wiley Intersci.* (1991).

23.   Tien, P. K. Integrated optics and new wave phenomena in optical waveguides. *Rev. Mod. Phys.* **49,** 361–420 (1977).

24.   Cottier, K. Advanced label free biochemical sensors based on integrated optical waveguide gratings: theory, modeling, design and characterization. (Université de Neuchâtel, 2004).

25.   Kovacs, N. *et al.* Optical Anisotropy of Flagellin Layers: In Situ and Label-Free Measurement of Adsorbed Protein Orientation Using OWLS. *Anal. Chem.* **85,** 5382–5389 (2013).

26.   Lambeck, P. V. Integrated optical sensors for the chemical domain. *Meas. Sci. Technol.* **17,** R93–R116 (2006).

27.   Campbell, D. in *Principles of Bacterial Detection: Biosensors, Recognition Receptors and Microsystems* (eds. Zourob, M., Elwary, S. & Turner, A.) 169–211 (2008).

28.   Snyder, A. & Love, J. *Optical waveguide theory*. (Chapman and Hall Ltd., London, 1983).

29.   Benaissa, K. & Nathan, A. Silicon anti-resonant reflecting optical waveguides for sensor applications. *Sensors Actuators A* **65,** 33–44 (1998).

30.   Duguay, M. A., Kokubun, Y., Koch, T. L. & Pfeiffer, L. Antiresonant reflecting optical waveguides in SiO2-Si multilayer structures. *Appl. Phys. Lett.* **49,** 13–15 (1986).

31.   Jimenez, D., Bartolome, E., Moreno, M., Munoz, J. & Dominguez, C. An integrated silicon ARROW Mach-Zehnder interferometer for sensing applications. *Opt. Commun.* **132,** 437–441 (1996).

1.6 References

32. Prieto, F. *et al.* Design and analysis of silicon antiresonant reflecting optical waveguides for evanscent field sensor. *J. Light. Technol.* **18**, 966–972 (2000).

33. Brecht, A. & Gauglitz, G. Optical probes and transducers. in *Biosensors and Bioelectronics* **10**, 923–936 (1995).

34. Chen, F., Wang, X.-L. L. & Wang, K.-M. M. Development of ion-implanted optical waveguides in optical materials: A review. *Opt. Mater. (Amst).* **29**, 1523–1542 (2007).

35. Davis, K. M., Miura, K., Sugimoto, N. & Hirao, K. Writing waveguides in glass with a femtosecond laser. *Opt. Lett.* **21**, 1729–1731 (1996).

36. Parriaux, O. & Veldhuis, G. J. Normalized analysis for the sensitivity optimization of integrated optical evanescent-wave sensors. *J. Light. Technol.* **16**, 573–582 (1998).

37. Joannopoulos, J. D., Johnson, S. G., Winn, J. N. & Meade, R. D. Photonic Crystals: Molding the Flow of Light, 2nd Edition. *Photonic Cryst. Molding Flow Light. 2nd Ed.* 1–286 (2008).

38. Tamir, T. & Garmire, E. *Integrated optics. Berlin: Springer-Verlag* **2**, (Springer-Verlag Berlin, 1979).

39. Marcatili, E. A. J. A. J. Dielectric rectangular waveguide and directional coupler for integrated optics. *Bell Syst. Tech. J.* **48**, 2071–2102 (1969).

40. Osterberg, H. & Smith, L. Transmission of Optical Energy Along Surfaces: Part II, Inhomogeneous Media. *Journal of the Optical Society of America* **54**, 1078 (1964).

41. Dakss, M. L., Kuhn, L., Heidrich, P. F. & Scott, B. A. Grating coupler for efficient excitation of optical guided waves in thin films. *Appl. Phys. Lett.* **16**, 523–525 (1970).

42. Peng, S., Tamir, T. & Bertoni, H. L. Theory of periodic dielectric waveguides. *IEEE Trans. Microw. Theory Tech. MTT-23* **123**, (1975).

43. Tamir, T. & Peng, S. T. Applied Physics Analysis and Design of Grating Couplers. *Appl. Phys.* **254**, 235–254 (1977).

44.   Hamori, A. & Nagy, N. Sub-micrometer period refractive index grating coupler for single mode optical waveguide sensors [chemical and biosensor applications]. *Proc. IEEE Sensors, 2004.* (2004).

45.   Vörös, J. *et al.* Optical grating coupler biosensors. *Biomaterials* **23,** 3699–3710 (2002).

46.   Horvath, R., Pedersen, H. C., Skivesen, N., Selmeczi, D. & Larsen, N. B. Monitoring of living cell attachment and spreading using reverse symmetry waveguide sensing. *Appl. Phys. Lett.* **86,** 71101 (2005).

47.   Homola, J., Yee, S. S. & Gauglitz, G. Surface plasmon resonance sensors: review. *Sensors Actuators, B Chem.* **54,** 3–15 (1999).

48.   Cooper, M. a. Optical biosensors: where next and how soon? *Drug Discov. Today* **11,** 1061–7 (2006).

49.   Fang, Y. Label-Free Optical Biosensors in Drug Discovery. *Trends Bio/pharmaceutical Ind.* (2007).

50.   Gauglitz, G. & Goddard, N. J. N. in *Handbook of Spectroscopy* 1115–1158 (Wiley-VCH Verlag GmbH & Co. KGaA, 2014).

51.   Wiki, M. & Kunz, R. E. Wavelength-interrogated optical sensor for biochemical applications. *Opt. Lett.* **25,** 463–465 (2000).

52.   Kozma, P. *et al.* Grating coupled optical waveguide interferometer for label-free biosensing. *Sensors Actuators B Chem.* **155,** 446–450 (2011).

53.   Stamm, C. & Lukosz, W. Integrated optical difference interferometer as refractometer and chemical sensor. *Sensors and Actuators B: Chemical* **11,** 177–181 (1993).

54.   Swann, M. J., Peel, L. L., Carrington, S. & Freeman, N. J. Dual-polarization interferometry: an analytical technique to measure changes in protein structure in real time, to determine the stoichiometry of binding events, and to differentiate between specific and nonspecific interactions. *Anal. Biochem.* **329,** 190–198 (2004).

55.   Concepcion, J. *et al.* Label-free detection of biomolecular interactions using BioLayer interferometry for kinetic characterization. *Comb. Chem. High Throughput Screen.* **12,** 791–800 (2009).

1.6 References

56.   Nirschl, M., Reuter, F. & Vörös, J. Review of Transducer Principles for Label-Free Biomolecular Interaction Analysis. *Biosensors* **1,** 70–92 (2011).

57.   Heideman, R. G. G., KOOYMAN, R. P. H. P. H. & Greve, J. Performance of A Highly Sensitive Optical Wave-guide Mach-zehnder Interferometer Immunosensor. *Sensors and Actuators B-chemical* **10,** 209–217 (1993).

58.   Schneider, B. H., Edwards, J. G. & Hartman, N. F. Hartman interferometer: versatile integrated optic sensor for label-free, real-time quantification of nucleic acids, proteins, and pathogens. *Clin. Chem.* **43,** 1757–1763 (1997).

59.   Brandenburg, A., Krauter, R., Künzel, C., Stefan, M. & Schulte, H. Interferometric sensor for detection of surface-bound bioreactions. *Appl. Opt.* **39,** 6396–6405 (2000).

60.   Ymeti, A. *et al.* Realization of a multichannel integrated Young interferometer chemical sensor. *Appl. Opt.* **42,** 5649–5660 (2003).

61.   Kozma, P., Kehl, F., Ehrentreich-Förster, E., Stamm, C. & Bier, F. F. Integrated planar optical waveguide interferometer biosensors: A comparative review. *Biosensors and Bioelectronics* **58,** 287–307 (2014).

62.   Vahala, K. K. J. Optical microcavities. *Nature* **424,** 839–846 (2003).

63.   Ciminelli, C., Campanella, C. E. C. M., Dell'Olio, F., Campanella, C. E. C. M. & Armenise, M. N. Label-free optical resonant sensors for biochemical applications. *Prog. Quantum Electron.* **37,** 51–107 (2013).

64.   Vollmer, F. & Arnold, S. Whispering-gallery-mode biosensing: label-free detection down to single molecules. *Nat. Methods* **5,** 591–596 (2008).

65.   Tünnemann, R. *et al.* Optical biosensors. Monitoring studies of glycopeptide antibiotic fermentation using white light interference. *Anal. Chem.* **73,** 4313–4318 (2001).

66.   Fattinger, C. The bidiffractive grating coupler. *Appl. Phys. Lett.* **62,** 1460–1462 (1993).

67.   Spinke, J. *et al.* The bidiffractive grating coupler: application to im-
       munosensing. *Sensors Actuators B Chem.* **39,** 256–260 (1997).

68.   Kunz, R. E. E. R., Edlinger, J., Sixt, P. & Gale, M. T. Replicated chirped
       waveguide gratings for optical sensing applications. *Sensors Actua-
       tors A Phys.* **47,** 482–486 (1995).

69.   Cush, R. *et al.* The resonant mirror: A novel optical biosensor for di-
       rect sensing of biomolecular interactions. Part I: Principle of opera-
       tion and associated instrumentation. *Biosens. Bioelectron.* **8,** 347–353
       (1993).

70.   Rothen, A. The Ellipsometer, an Apparatus to Measure Thickness of
       Thin Surface Films. *Rev. Sci. Instrum.* **16,** 26–30 (1945).

71.   Nair, R. V. & Vijaya, R. Photonic crystal sensors: An overview. *Pro-
       gress in Quantum Electronics* **34,** 89–134 (2010).

72.   Fattinger, C. Focal Molography: Coherent Microscopic Detection of
       Biomolecular Interaction. *Phys. Rev. X* **4,** 031024 (2014).

73.   Nieuwenhuizen, M. S. & Venema, A. Surface acoustic wave chemical
       sensors. *Sensors Mater.* **5,** 261–300 (1989).

74.   Wohltjen, H. *et al.* Acoustic Wave Sensor - Theory, Design, and Phys-
       ico-Chemical Applications. (1997).

75.   Bruckenstein, S. & Shay, M. Experimental aspects of use of the quartz
       crystal microbalance in solution. *Electrochimica Acta* **30,** 1295–1300
       (1985).

76.   Becker, B. & Cooper, M. A survey of the 2006–2009 quartz crystal
       microbalance biosensor literature. *J. Mol. Recognit.* (2011).

77.   Grieshaber, D., MacKenzie, R., Vörös, J. & Reimhult, E. Electrochemi-
       cal Biosensors - Sensor Principles and Architectures. *Sensors* **8,** 1400–
       1458 (2008).

78.   Tiefenthaler, K. & Lukosz, W. Sensitivity of grating couplers as inte-
       grated-optical chemical sensors. *Journal of the Optical Society of
       America B* **6,** 209 (1989).

79.   Tiefenthaler, K. & Lukosz, W. Integrated optical switches and gas
       sensors. *Opt. Lett.* **9,** 137–139 (1984).

1.6 References

80.   Cunningham, B., Li, P., Lin, B. & Pepper, J. Colorimetric resonant re-flection as a direct biochemical assay technique. *Sensors Actuators B Chem.* (2002).

81.   Nellen, P. M., Tiefenthaler, K. & Lukosz, W. Integrated optical input grating couplers as biochemical sensors. *Sensors and Actuators* **15,** 285–295 (1988).

82.   Lukosz, W. *et al.* Output grating couplers on planar optical wave-guides as direct immunosensors. in *Biosensors and Bioelectronics* **6,** 227–232 (Elsevier, 1991).

83.   Duval, D. & Lechuga, L. M. Optical waveguide biosensors. *Photonics, Vol. 4 Biomed. Photonics, Spectrosc. Microsc.* (2015).

84.   Estevez, M.-C., Alvarez, M. & Lechuga, L. M. L. M. Integrated optical devices for lab-on-a-chip biosensing applications. *Laser Photon. Rev.* **6,** 463–487 (2012).

85.   Schmitt, K., Oehse, K., Sulz, G. & Hoffmann, C. Evanescent field Sen-sors Based on Tantalum Pentoxide Waveguides – A Review. *Sensors* **8,** 711–738 (2008).

86.   Kurrat, R., Textor, M., Ramsden, J. J., Böni, P. & Spencer, N. D. Instru-mental improvements in optical waveguide light mode spectroscopy for the study of biomolecule adsorption. *Rev. Sci. Instrum.* **68,** 2172–2176 (1997).

2 Scope of the Thesis

The doctoral thesis at hand is a result of my research conducted at the Centre Suisse d'Electronique et de Microtechnique (CSEM) SA (Landquart, Switzerland) and Optics Balzers AG (Balzers, Liechtenstein), in collaboration with the Laboratory of Biosensors and Bioelectronics (LBB) at the Federal Institute of Technology ETH (Zürich, Switzerland). Its content was motivated by the growing demand for compact, integrated and affordable biosensors for the comprehensive and continuous detection and monitoring of organic pollutants in the aquatic environment[1,2].

Natural and man-made endocrine disrupting compounds (EDCs) pose a significant hazard to the environment and human health and are a class of organic pollutant with an increasing presence in the environment[3,4]. EDCs are chemicals that can mimic natural hormones or inhibit their action by interacting with the receptors of natural hormones, thus altering the normal function of the endocrine, immune or nervous systems. In the aquatic environment, all organisms are continuously exposed to EDCs for several life generations since most of them are persistent pollutants. Sources of EDCs are manifold, including industrial, residential and agricultural waste. The thesis was financed and conducted within the framework of the European Union FP7 Project RADAR ("Rationally Designed Aquatic Receptors integrated in label-free biosensor platforms for remote surveillance of toxins and pollutants", grant agreement n° FP7-KBBE- 2010- 4-RADAR 265721). The goal of the project and its 7-member consortium was to develop a compact, versatile and fully-automated biosensor platform to detect interaction, presence and concentration of these potentially hazardous compounds.

After briefly reviewing the history, theory and interrogation principles of waveguide biosensors in Chapter 1, the objective of Chap-

ter 3 was to establish a designated, numerical tool to thoroughly understand, simulate and optimize the waveguide grating structure itself towards highest sensitivity. Albeit the commercial availability of sophisticated, highly specialized but costly simulations software, the intent was to develop methods that can easily be implemented with standard software commonly available in academia. The influence of various sensor design parameters has been simulated with the developed tool and compared with standard software.

Chapter 4 aims at the verification of the simulated results. Despite the fact that the theoretical foundations of the sensitivity of waveguide grating based (bio)sensors are well-known, understood and their implications anticipated by the scientific community for several decades, to our knowledge, no prior publication has experimentally confirmed waveguide sensitivity for multiple film thicknesses, wavelengths and polarization of the propagating light. In this chapter, the bulk refractive index sensitivity versus waveguide thickness of said refractometric sensors was experimentally determined and compared with predictions based on established theory.

The main Chapter 5 describes the actual development, integration and validation of the novel, angle interrogated optical sensor (ARGOS) platform. The previous chapters, the project requirements as well as the preceding work performed at CSEM (Kunz et al.[5]; Parriaux, Sixt[6]; Wiki et al.[7]; Cottier et al.[8]; Voirin, Pasche, Adrian et al.[9]), laid the foundations of this biosensor design. A novel concept for the angular interrogation of the waveguide grating regions with a MEMS micromirror was developed and characterized. Recent advances in MEMS technology and integrated electronics provide new opportunities for the implementation of devices unavailable at the time of the antecedent, pioneering work. The MEMS micromirror and dedicated, high-speed electronics allow for a high interrogation rate and extended measurement range in a compact format and at low energy expenses, both requirements for portable in-situ measurements. After an introduction to the basic sensor principle and design, the sensor performance was validated by refractometric as well as bioaffinity measurements, however the

main focus laid on the physical performance of the system as the biochemical assay development was assigned to the project partners. The chapter's appendix will give additional insights in unpublished work on improving the sensor performance as well as a detailed explanation of the systems engineering effort conducted and individual components implemented in the ARGOS system.

In general, label-free methods are still less sensitive than labeled ones. To overcome this disadvantage, many promising and highly sensitive interferometers, as well as resonator based integrated optical transducers, have been presented to increase the sensitivity and lower the limit of detection of label-free devices[10–12]. Sophisticated microsphere, disc and ring resonator sensors with low limit of detection (LoD) and high quality factors (Q-factor) have been realized but seem not to be suitable for volume production, due to their high level of complexity regarding fabrication and light coupling. In contrast, grating based waveguide sensors can be batch produced by standard lithographic means and light can easily be coupled via the diffractive grating itself, but they exhibit lower Q-factors and, therefore, higher LoD. In Chapter 6, a novel sensor concept was explored within the framework of a CTI-Project (Commission for Technology and Innovation, project n° 13865.2 PFNM-NM), combining the simplicity of planar grating couplers with a high finesse and extended dynamic range of resonant cavities. Whereas the chapter's main content focuses on the concept idea, theory and numerical design, preliminary experimental data are disclosed in the appendix of the chapter. Although the basic fabrication and working principle of this novel sensor type have been demonstrated, additional research effort is required to produce and thoroughly characterize a stable sensor platform.

In the concluding Chapter 7, the thesis and its content will be summarized and closing remarks regarding potential improvements and suggestions for further improvements in sensor design are provided.

2.1 References

1. Carvalho, R. N. *et al.* Mixtures of Chemical Pollutants at European Legislation Safety Concentrations: How Safe are They? *Toxicol. Sci.* **141,** 218–233 (2014).

2. Farré, M. & Barceló, D. *Biosensors for Environmental Monitoring of Aquatic Systems.* **5,** (Springer Berlin Heidelberg, 2009).

3. Diamanti-Kandarakis, E. *et al.* Endocrine-disrupting chemicals: an Endocrine Society scientific statement. *Endocr. Rev.* **30,** 293–342 (2009).

4. Pedotti, M. *et al.* Rationally Modified Estrogen Receptor Protein as a Bio-Recognition Element for the Detection of EDC Pollutants: Strategies and Opportunities. *Int. J. Environ. Res. Public Health* **12,** 2612–2621 (2015).

5. Kunz, R. E. E. R., Edlinger, J., Sixt, P. & Gale, M. T. Replicated chirped waveguide gratings for optical sensing applications. *Sensors Actuators A Phys.* **47,** 482–486 (1995).

6. Parriaux, O. & Sixt, P. Sensitivity optimization of a grating coupled evanescent wave immunosensor. *Sensors and Actuators B: Chemical* **29,** 289–292 (1995).

7. Wiki, M. & Kunz, R. E. Wavelength-interrogated optical sensor for biochemical applications. *Opt. Lett.* **25,** 463–465 (2000).

8. Cottier, K., Wiki, M., Voirin, G., Gao, H. & Kunz, R. E. Label-free highly sensitive detection of (small) molecules by wavelength interrogation of integrated optical chips. *Sensors and Actuators B: Chemical* **91,** 241–251 (2003).

9. Adrian, J. *et al.* Wavelength-interrogated optical biosensor for multi-analyte screening of sulfonamide, fluoroquinolone, β-lactam and tetracycline antibiotics in milk. *TrAC Trends Anal. Chem.* **28,** 769–777 (2009).

10. Ciminelli, C., Campanella, C. E. C. M., Dell'Olio, F., Campanella, C. E. C. M. & Armenise, M. N. Label-free optical resonant sensors for biochemical applications. *Prog. Quantum Electron.* **37,** 51–107 (2013).

11.   Estevez, M.-C., Alvarez, M. & Lechuga, L. M. L. M. Integrated optical devices for lab-on-a-chip biosensing applications. *Laser Photon. Rev.* **6,** 463–487 (2012).

12.   Kozma, P., Kehl, F., Ehrentreich-Förster, E., Stamm, C. & Bier, F. F. Integrated planar optical waveguide interferometer biosensors: A comparative review. *Biosensors and Bioelectronics* **58,** 287–307 (2014).

2 Scope of the Thesis

3 FEM-based Method for the Simulation of Dielectric Waveguide Grating Biosensors[‡]

3.1 Abstract

Label-free optical biosensors are important tools to study the kinetics, interaction and presence of (bio) chemical compounds in various fields, such as biotechnology, pharmaceutical industry, diagnostics as well as environmental and food quality monitoring. Systems based on planar optical waveguides with input/output grating couplers are of interest as they offer multiple tuning parameters for the chip design and their high sensitivity. In the present chapter, an algorithm based on the Finite-Elements Method (FEM) is proposed in order to find the chip response and to optimize the sensitivity of the sensor system. Total field and scattered field formulation, coupled with the Transmission Line Transfer Matrix Method (TLTMM), are compared with FEM. Unlike some widely used approximations, the impact of the grating depth, shape, duty-cycle as well as losses and surface roughness are taken into account. Another advantage of the presented method is the possibility to implement a large part of the algorithm with commercially available FEM solvers. Several practical situations are treated proving the validity of the approach against the Local Interference Method (LIME). The waveguide losses appear to be a decisive parameter for the chip design.

3.2 Introduction

The use of chemical and biological sensors based on electromagnetic waves at optical wavelengths has grown significantly over the last decade. A particularly interesting category of optical biosensors is based on waveguides with a high refractive index film. The sensing action is accomplished by measuring changes of the effective refractive index n_{eff} sensed by the evanescent field. This technique has found applications in label-free as well as in fluorescence-based, labelled sensors.

Different geometrical configurations as well as interrogation schemes for label-free waveguide based sensors have been presented in the scientific literature in the past decades[1–3]. Dielectric waveguide grating sensors with input/output couplers are one of the simpler and cheaper solutions, which have also been commercialized successfully. Since many parameters can be tuned for the design of the chip in order to maximize the waveguide grating coupler's sensitivity, the optimization of the latter is essential and deserves an explicit rationale. In this chapter, only the electromagnetic modeling of the waveguide will be considered, the biochemical modeling can be found in Ref. 3.

The chip is a simple multilayer planar dielectric waveguide. On a substrate S (mostly glass) a thin film F with a high refractive index n_f is deposited (such as Tantalum Pentoxide Ta_2O_5). The biological L layer (sensing layer) and the cover C (mostly aqueous solution) are directly applied to the waveguide film, hence the cover and the substrate form the cladding of the waveguide. The resulting sensor chip, together with important geometry and material parameters, is shown in Figure 3.1. Typical parameter values, together with the nominal values used in this report, are summarized in Table 3.1. For the investigated sensor chip, the waveguide thickness h_f differs for the input and output coupler to prevent interference between the input and output beams, which occurs if the film thicknesses and therefore the coupling angles are equal[3,4]. The dimensions in the x and z directions are much larger than

the grating period, and therefore it is possible to consider the grating as a two-dimensional, periodic geometry.
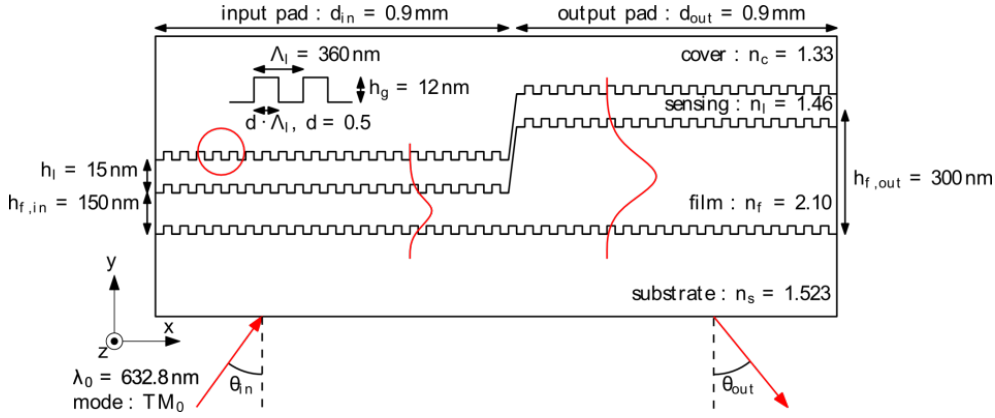

Figure 3.1: Schematic side view of a biosensor waveguide chip with an input and an output grating coupler, consisting of a substrate S, waveguide film F with thickness h_f, sensing layer L with thickness h_l and cover C, with refractive indices n_s, n_f, n_l and n_c, respectively, illuminated with a laser with wavelength λ and polarization TM_0 under an angle θ_{in}. Additional parameters are defined in Table 3.1.

Table 3.1: Input Parameters for Simulation of the BG Reflector and Resonator.

Parameter	Symbol	Range	Nominal
Input grating length	d_{in}	0.5 - 1 mm	0.9 mm
Output grating length	d_{out}	0.5 - 1 mm	0.9 mm
Length in z-direction	h_f	0.5 - 1 mm	0.9 mm
Grating period	Λ	200 – 800 nm	360 nm
Wavelength	λ	300 – 1000 nm	632.8 nm
Polarization	ρ	TE, TM	TM
Mode number	m	0, 1	0
Incidence angle	θ_{in}	±<90°	±<60°
Output angle	θ_{out}	±<90°	±<60°
Grating duty cycle	d	0.3 – 0.7	0.5
Grating depth	h_g	8 – 40 nm	12 nm
Film thickness input pad	$h_{f,in}$	80 – 500 nm	150 nm
Film thickness output pad	$h_{f,in}$	80 – 500 nm	300 nm
Sensing layer thickness	h_l	5 – 200 nm	15 nm
Substrate refractive index	n_s	1.5 – 1.7	1.523
Waveguide film refractive index	n_f	1.7 – 2.3	2.10
Sensing layer refractive index	n_l	1.3 – 1.5	1.46
Cover refractive index	n_c	1.3 – 1.5	1.33

3.2 Introduction

In the presented measurement configuration, the input pad is illuminated through the substrate with a collimated laser beam. Different interrogation schemes exist for waveguide grating couplers[2]. The first is via angular tuning of the input angle θ_{in}, whereas the intensity (eventually also the position) of the output beam is measured at a constant wavelength. At the coupling angle, a maximal coupling efficiency is reached. Any changes of the refractive index or the thickness of the sensing biolayer lead to a change of the coupling angle of the input grating pad and can therefore be detected. Alternatively, it is also possible to measure the transmitted light at the cover side. When the coupling condition is fulfilled, the energy couples into the film and a minimum can be observed at the cover. The second operation scheme is the so-called WIOS principle (wavelength interrogated optical sensor)[3,4]. The angle of the incident beam is maintained constant while the wavelength is tuned (by some nanometers), while the intensity of the output beam is measured. Again, any change of the effective refractive index, e.g., due to the adsorption of biomolecules to the sensor surface, the resulting resonance curve shift will be monitored. In the following, only the angular interrogation will be investigated, mainly due to practical means like extended tuning range as well as stability and independence of the wavelength of the laser source. Nonetheless, the following calculations would also hold true for the wavelength interrogating sensing scheme.

The design of a biosensor obeys some basic principles described in Ref. 2. The sensitivity should be maximal in order to have a low limit of detection (LoD). The signal to noise ratio is clearly another important factor to consider, strongly influenced by the so-called SBSR (sensing layer-to-bulk volume signal ratio), which is defined as the sensitivity with respect to the sensing layer divided by the sensitivity with respect to the cover[5]. In the following, the focus will solely be on the grating coupler and not on a complete chip. Since analogous structures, the presented methods are valid for both, input and output grating couplers. Because for many waveguide grating configurations, including the one presented in Figure 3.1, the TM_0 mode leads to higher

sensitivity[6] and a sharper resonance curve, only the fundamental TM mode will be investigated in this work. Even though the waveguide's first mode would be TE0, its sensitivity is inferior to the TM0 mode, implying that the TE0 mode is only useful if this is the unique existing mode due to the layer's thickness or if two linearly independent measurements are required[7]. The presented methods work both for TE and TM polarization.

For the prediction of the sensor sensitivity, different methods are known, such as analytical approximation based on the mode equation[7] or methods based on rigorous diffraction theory[6]. In Ref. 8, Cottier et al. have introduced the Local Interference Method (LIME), which is a simplified multiple scattering method[9]. This method has proven to be very fast but the used implementation suffers from many limitations. The computation relies on a thin grating approximation, thus it is not possible to take the exact grating shape, its duty-cycle (also known as "filling factor") nor depth into account. The waveguide film losses are also neglected. These simplifications preclude a reliable reconstruction of the sensor's resonance curve, particularly the full width at half maximum (FWHM).

The chapter presents an algorithm based on Finite-Elements Method (FEM) and Transmission Line Transfer Matrix Method (TLTMM) to compute the field distribution and extract the sensitivity of the chip. This method allows the inclusion of the grating depth, duty-cycle and shape, the film losses due to damping, the surface roughness, etc. The simulation of non-periodic, non-uniform gratings has also been done but will not be presented here. The main advantage of FEM is the flexibility and the availability of powerful commercial solvers. Consequently, the implementation of the described method is particularly fast and the simulation of other configurations is possible with small adaptations. After the presentation of the numerical methods and the validation against LIME, some results illustrate the influence of the film thickness, the grating depth and the film losses.

3.3 Numerical Methods

3.3.1 FEM Total Field

The input coupler as shown in Figure 3.1 can be simplified to a periodic structure as presented in Figure 3.2(a). The goal is to find the electromagnetic field distribution for a plane wave excitation. Periodic Floquet boundary conditions are introduced, therefore the x component of the wave vector k_x is constant at the interface between the materials. The propagation constant β is computed from the effective refractive index and the wave vector ($\beta = n_{eff} \cdot k_0$), together with the mode equation (Equation 1.8).
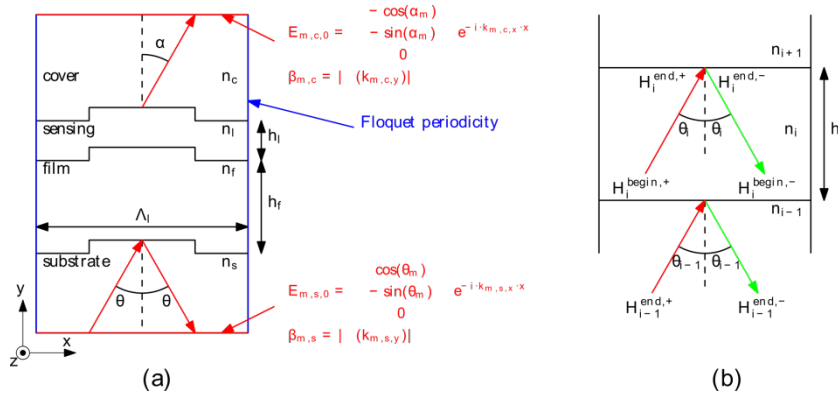
Figure 3.2: Considered geometry for FEM with TM waves. (**a**) Side view of layer stack. (**b**) Transition at layer boundaries i-1, i and i, i+1.

The main problem is to find boundary conditions that allow the injection of the plane wave and the absorption of the reflected and diffracted waves. First, we introduce the grating equations[10,11]:

$$m \cdot \lambda_0 = \Lambda \cdot \left(n_c \, sin\left(\alpha_m\right) - n_s \, sin\left(\theta\right)\right) \tag{3.1a}$$

$$m \cdot \lambda_0 = \Lambda \cdot n_s \left(sin(\theta_m) - sin\left(\theta\right)\right) \tag{3.1b}$$

where m represents the different grating diffraction orders, λ_0 the wavelength of the incident light, Λ the grating period, $n_{s/c}$ the refractive indices of the substrate and cover, respectively, θ the angle of the incident, θ_m of the diffracted and α_m transmitted wave of the mth diffrac-

tion order. The existence of a coupled mode is governed by the following equation:

$$-(n_s+n_c) < \frac{m \cdot \lambda_0}{\Lambda} < (n_s+n_c) \qquad (3.2a)$$

$$-2n_s < \frac{m \cdot \lambda_0}{\Lambda} < 2n_s \qquad (3.2b)$$

Note that this condition is conservative, since the incidence angle is not taken into account. Subsequently, Equation (3.1) can be solved for the angles θ_m and α_m and thus the wave vectors for the different orders are easily obtained at the substrate and at the cover with:

$$k_s = k_0 \cdot n_s \qquad (3.3a)$$

$$k_{m,s,x} = k_s \cdot sin(\theta_m) \qquad (3.3b)$$

$$k_{m,s,y} = k_s \cdot cos(\theta_m) \qquad (3.3c)$$

$$k_c = k_0 \cdot n_c \qquad (3.4a)$$

$$k_{m,c,x} = k_c \cdot sin(\alpha_m) \qquad (3.4b)$$

$$k_{m,c,y} = k_c \cdot cos(\alpha_m) \qquad (3.4c)$$

Finally, these waves are represented in the FEM model with port boundary conditions[12]. A port boundary condition can inject an electromagnetic wave with a given field distribution and propagation constant. Further, a port can also absorb the waves with identical propagation constants. Since the propagation constants are different for each diffraction order, a port is required at the cover and substrate for each order m (and $-m$). The electric field at the port and the propagation constant are deduced from the following equation for a transversal magnetic wave (see Figure 3.2(a)):

$$\begin{cases} E_{m,s,0} = \begin{bmatrix} cos(\theta_m) \\ -sin(\theta_m) \\ 0 \end{bmatrix} e^{-i \cdot k_{m,s,x} \cdot x} \\[20pt] \beta_{m,s} = \left| \mathbb{R}(k_{m,s,y}) \right| \end{cases} \tag{3.5}$$

$$\begin{cases} E_{m,c,0} = \begin{bmatrix} -cos(\alpha_m) \\ -sin(\alpha_m) \\ 0 \end{bmatrix} e^{-i \cdot k_{m,c,x} \cdot x} \\[20pt] \beta_{m,c} = \left| \mathbb{R}(k_{m,c,y}) \right| \end{cases} \tag{3.6}$$

Only the direction of the field is considered. The amplitude is scaled as such that a given amount of power is injected through the boundary. Only the port with the diffraction order 0 at the substrate side has a non-zero power. This corresponds to the plane wave illuminating the grating, modeling the incident laser beam.

The main advantage of the FEM is that a solution of the wave equation is searched for the real chip geometry, which is not the case for the local interference approximation. This allows taking into account additional parameters such as the grating depth and duty-cycle. The number of layers in the stack has no influence on the method, and it is possible to model an arbitrary grating shape. It is also possible to include materials with losses or metallic gratings[13]. From the ports, the scattering matrix and thus the reflection and transmission coefficients can be directly extracted. The limitations of the total field FEM formulation mainly remains in the computational cost. Problems also occur if many diffraction orders are present in the simulated geometry.

3.3.2   FEM Scattered Field

For plane wave excitation, it is often easier to write a scattered field formulations of the finite element method[14]. For a dielectric stacked grating, a plane wave cannot be used for the unscattered background field of the incident light. The background field should contain the solution for the stack with planar interfaces between the materials (without the grating). In this case, the grating rectangles are

subsequently added and the scattered field is solved again with Floquet periodicity but with perfectly matched layers (PMLs) at the top of the cover and the bottom of the substrate.

A possibility to obtain the background field is to use the FEM as described in Section 3.3.1. Since the interface is planar, only the diffraction order 0 is required. A better and faster solution is to find an analytical solution with the Transmission Line Transfer Matrix Method (TLTMM). The implementation of TLTMM is based on Refs. 15,16 and explained in more detail therein, and also allows for the consideration of inherent waveguide losses.

With Snell's law, the angle, the wave impedance and the component of the wave vector can easily be computed in each layer. The used notations are described in Figure 3.2(b). One can see that there is a forward and a backward travelling wave in each layer. Now the propagation of the wave inside a layer can be described for the TM polarization with its transverse field component H_i and an amplitude transmission matrix L_i:

$$\begin{bmatrix} H_i^{end,+} \\ H_i^{end,-} \end{bmatrix} = L_i \cdot \begin{bmatrix} H_i^{begin,+} \\ H_i^{begin,-} \end{bmatrix} \tag{3.7}$$

where $H^{end,\pm}$ and $H^{begin,\pm}$ are the forward and back travelling waves at the end and the beginning of each layer i, respectively. At the interface between two adjacent layers, the reflection and transmission coefficients $r_{i,i-1}^{TM}$ and $t_{i-1,i}^{TM}$ should be considered in both directions.

$$H_{i-1}^{end,-} = r_{i,i-1}^{TM} \cdot H_{i-1}^{end,+} + t_{i-1,i}^{TM} \cdot H_i^{begin,-} \tag{3.8a}$$

$$H_i^{begin,+} = t_{i,i-1}^{TM} \cdot H_{i-1}^{end,+} + r_{i-1,i}^{TM} \cdot H_i^{begin,-} \tag{3.8b}$$

After rearranging the terms, one ends up with:

$$\begin{bmatrix} H_i^{begin,+} \\ H_i^{begin,-} \end{bmatrix} = \frac{1}{t_{i-1,i}^{TM}} \cdot \begin{bmatrix} 1 & -r_{i,i-1}^{TM} \\ r_{i,i-1}^{TM} & 1 \end{bmatrix} \begin{bmatrix} H_{i-1}^{end,+} \\ H_{i-1}^{end,-} \end{bmatrix} \tag{3.9}$$

Consequently, the discontinuity transfer matrix between the ith and $i\text{-}1^{th}$ layer $I_{i,i\text{-}1}$ can be defined as:

$$\begin{bmatrix} H_i^{begin,+} \\ H_i^{begin,-} \end{bmatrix} = I_{i,i\text{-}1} \cdot \begin{bmatrix} H_{i\text{-}1}^{end,+} \\ H_{i\text{-}1}^{end,-} \end{bmatrix} \tag{3.10a}$$

with $\qquad I_{i,i\text{-}1} = \begin{bmatrix} 1+p & 1-p \\ 1-p & 1+p \end{bmatrix} \qquad p = \frac{Z_{w,i\text{-}1} \cdot \cos\left(\theta_{i\text{-}1}\right)}{Z_{w,i} \cdot \cos(\theta_i)} \tag{3.10b}$

where Z_w is the wave impedance. Finally, it is possible to assemble all the propagation and discontinuity transfer matrices in order to write an equation system for a stack of N dielectrics:

$$\begin{bmatrix} H_N^{end,+} \\ 0 \end{bmatrix} = T \cdot \begin{bmatrix} H_1^{begin,+} \\ H_1^{begin,-} \end{bmatrix} \tag{3.11a}$$

$$T = L_N \cdot I_{N,N\text{-}1} \cdot L_{N\text{-}1} \cdot \ldots \cdot L_2 \cdot I_{2,1} \cdot L_1 \tag{3.11b}$$

where $H_1^{begin,+}$ is the given plane wave excitation, and $H_1^{begin,-}$ and $H_N^{end,+}$ are the unknown variables. Per definition, there is no reflection at the last layer which implies $H_N^{end,-} = 0$. With the help of the matrix equation, the field distribution in the complete structure can be found recursively with the help of the Equations (3.7) and (3.10). With Maxwell's equations, all the fields (B, E, etc.) can be deduced. It is also possible to extract the Poynting vector and the absorption. The combined analytical (TLTMM) and numerical (FEM) is a very flexible and powerful method to simulate diffraction gratings. It is possible to take material losses into account or to include metallic shields (with a higher computation time). This inclusion of anisotropic materials is conceivable. There is also no computational limitation for the grating shape, such as triangular or sinusoidal. Additionally, it is possible to extend the procedure for a non-periodic gratings or for a gratings with non-planar wave excitation.

3.4 Comparison of the Methods

3.4.1 Detection of the Coupling

The presented methods will be compared to LIME for a defined grating (see input pad parameters in Figure 3.1). The FEM with total field formulations can be either modeled with ports at the cover or with a PML.

For FEM, different incidence angles are simulated in order to find the angle with the maximal coupling efficiency. For a biosensor, the goal is to maximize the amount of energy in the sensing layer (where the biochemical reaction takes places)[7]. Since the mode is guided within the film, it is also possible to search for a solution with maximum energy in the film. Another possibility is to minimize the transmission coefficient from the substrate to the cover if illuminated from the former side, hence at minimal transmission, the energy is coupled into the waveguide. With the total field formulation, this can be obtained directly from the scattering matrix between the ports. For a single mode waveguide the S-parameters can be interpreted in term of power flux[14]:

$$E_{domain,abs} = \iint_{domain} W_{avg} dS \tag{3.12a}$$

$$E_{domain,rel} = \frac{\iint_{domain} W_{avg} dS}{\iint_{all} W_{avg} dS} \tag{3.12b}$$

$$T_i = \left| S_{21}^2 \right| \tag{3.12c}$$

$$= \frac{power\ transmitted\ at\ cover\ side\ (order\ i)}{incident\ power\ at\ substrate\ side} \tag{3.12d}$$

where $E_{domain,abs}$ and $E_{domain,rel}$ are the absolute and relative energies in the respective domain (sensing layer L or waveguide film F), respectively, W_{avg} is the averaged energy density over a time period, T_i the transmission at the layer i and the corresponding scattering parameter S for forward transmission. To compare the absolute energy density between total and scattered field, the curves should be normalized.

The resulting resonance curve for different total field FEM expressions from Equation (3.12) can be seen in Figure 3.3. One can see that there is almost no difference between measuring the resonance with transmission coefficient, relative or absolute energy (less than 0.002° error). The deviation from the maximum becomes smaller with decreasing grating depth.
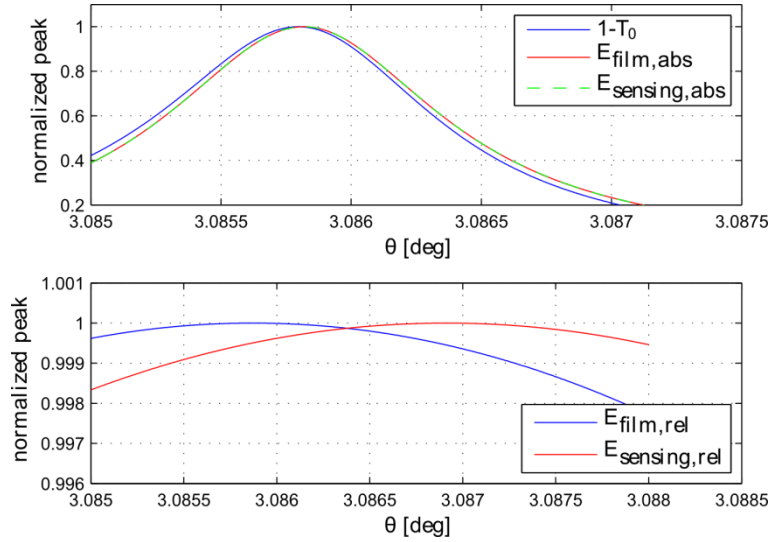

Figure 3.3: Resonance curves with total field FEM formulation (small scale).

The main difference lies in the FWHM. The theoretical peak width is only about 0.001° for the calculation with the transmission coefficient and the absolute energy, and about 0.08° for the relative energy. However, considering the relative energy is also useful because the peak is easier to detect with numerical maximization routines.

A comparison between total field and scattered field formulations has also been performed. Since the fields did not have the same amplitude, it is advantageous to make the comparison with the relative energy. It can be concluded that, in this case, the deviation between the total and scattered field FEM formulations is lower than 0.01% for $E_{film,rel}$ and $E_{sensing,rel}$ over the entire angular range.

3.4.2   Comparison between FEM and Lime

Since the used implementation of LIME is only valid for shallow gratings, the comparison has been done for grating depths between

0.25 nm and 25 nm. In the upper plot of Figure 3.4, the resonance curves are shown for shallower grating depths (considering the relative energy in sensing layer). The lower plots show the deviation of the resonance angle between LIME and FEM (scattered field and total field). The black line in the lower plots represents the maximum resolution (finite increment between two computed angles) which therefore represents the minimal reachable error with the implemented angular sweep.

With a grating depth of 0.25 nm, the deviation is clearly smaller than 10^{-5}°. Simulations with a smaller grating depth are hard to perform because the simulated mesh is becoming too large. Nonetheless, the presented precision is clearly sufficient for the design of a biosensor. It can be concluded that the different finite element models are in good agreement with LIME for simple geometries with shallow gratings. LIME has proven to be sufficient regarding the calculation of the coupling angle, although LIME should not be used if the grating depth is exceeds ~15 nm.
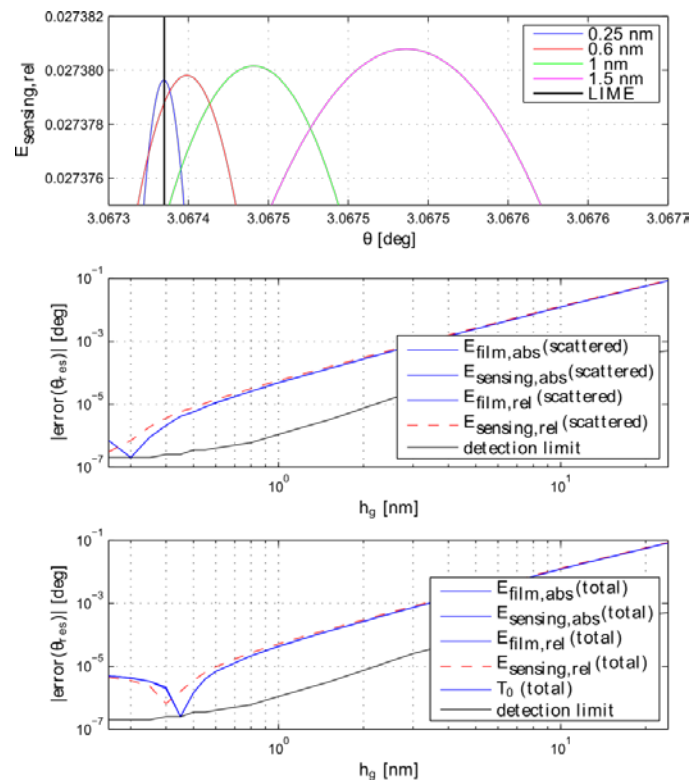

Figure 3.4: Influence of the grating depth h_g on the error between FEM and the local interference method.

3.5 Sensor Sensitivity

3.5.1 Procedure for the Detection of the Resonance

In Section 3.4, the resonance curves of the energy in the sensing layer have been obtained with an angular sweep. However, if only the angle of resonance needs to be calculated, this solution is clearly not optimal. A standard minimization algorithm can be used (for example Nelder-Mead simplex) to find the resonance, but here a model-based optimization was applied. From the grating theory, it is known that for the given configuration, the resonance curve is a Lorentzian function[6,17]. From the symmetry of the geometry, it is obvious that if there is a resonance peak at θ_{res}, there is another peak at $-\theta_{res}$. Consequently, the two peaks should be considered together. Another effect comes from the fact that even at a point far away from the resonance the energy in the sensing layer is not zero. Thus, an offset should also be included in the function. Considering these two facts, the following fit function can be deduced:

$$E_{fit}(\theta) = \frac{f_{max}\left(\frac{FWHM}{2}\right)^2}{\left(\theta-\theta_0\right)^2+\left(\frac{FWHM}{2}\right)^2} + \frac{f_{max}\left(\frac{FWHM}{2}\right)^2}{(\theta+\theta_0)^2+\left(\frac{FWHM}{2}\right)^2} + offset \qquad (3.13)$$

where FWHM is the full width at half maximum. The function is fitted with the least square method. Together with the computed points and the position of the maximum, the peak amplitude and the full width at half maximum can be extracted.
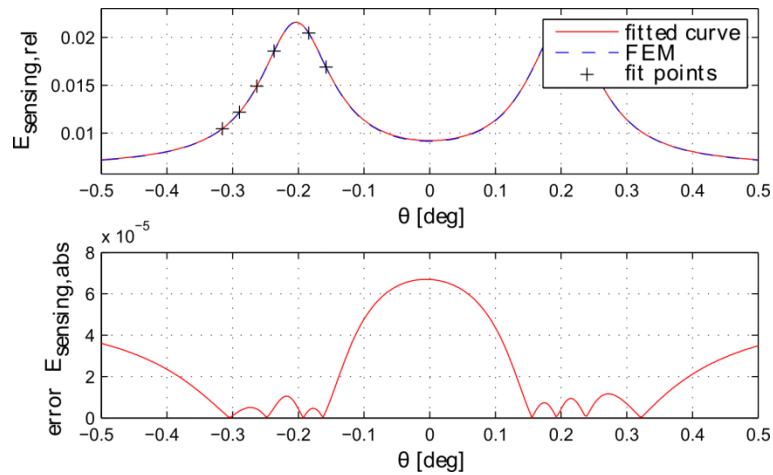
Figure 3.5: Comparison of the resonance peak computed with FEM and the fitted curve.

The validity of the chosen fit is shown in Figure 3.5. The geometry has been chosen (by adaptation of the film thickness) as such that the resonance angle is very small (about 0.2°). The obtained curve clearly supports the chosen method with two Lorentzian peaks with maxima at $\pm\theta_0$ (Equation (3.13)). The dashed blue curve is computed with FEM for different angles. The black points are the data used for the least square fit and the fitted function is the red curve. The lower plot shows the deviation between the fit and the reference curve obtained directly with FEM. One can see that a very low number of points is sufficient for reconstructing the shape of the resonance peak with a good accuracy. An advantage of the model-based search is, that not only the value and position of the extremum can be calculated, but also an estimation of the complete peak shape. The full width at half maximum is an important parameter for the sensor regarding its Q-factor and limit of detection.

3.5.2   Computation of the Sensitivity

Finding the resonance angle or frequency is important but not sufficient for designing a grating based biosensor. The sensitivity of the sensor is defined as

$$s_{sensitivity} = \frac{\partial\ measurement\ parameter}{\partial\ sensing\ parameter} \quad e.g.\ \frac{\partial\theta}{\partial n_c} \tag{3.14}$$

where the sensing parameter is the parameter under investigation, e.g. the change of the cover refractive index. The measurement parameter is the resonance angle or the wavelength, for either angular and wavelength interrogation, respectively. The goal is to maximize the sensitivity s of the sensor in order to reach a low detection limit. Other transfer functions can be considered such as the signal-to-noise ratio or the disturbance rejection. The signal-to-noise ratio can be improved by maximizing the *SBSR* (sensing layer to bulk volume signal ratio)[5]:

$$s_{SBSR} = \frac{\frac{\partial \theta}{\partial n_l}}{\frac{\partial \theta}{\partial n_c}} \tag{3.15}$$

In this case, any changes in the cover refractive index n_c are considered as background contributions and changes in the refractive index of the adlayer n_l as the quantity of interest. The goal is to have a large sensitivity for the sensing layer and a small one for the cover. The *SBSR* can also be written for changes of the sensing layer thickness, which means that its derivative should be computed. This is done numerically with a first, second or fourth order approximation. The Richardson's formulas have been used to estimate the required step size[18], whereas the second order approximation has proven to be sufficient. In order to find the maximum, again the procedure of Figure 3.5 is used for the calculation of the sensing parameter, which is required for the numerical approximation of the derivative (see Equation (3.14)). Often the sensitivity is expressed for the effective refractive index[5,7,19], but here the sensitivity is directly expressed with the measurement parameter to have a direct relation to experimental data.

The method described above can be used to find the response of a particular sensor. Since the goal is to optimize the design, a geometrical or a material parameter (here called optimization parameter) is varied and the response is computed for each value. From the obtained results, the sensor design can be improved. The optimization parameter can be specified in a table and the sensitivity is computed for all the given values. If the optimization should be done with more than one parameter, then the computation costs are too high with a multi-

dimensional table and a genetic or direct search algorithm is used to find the optimal design. The direct search algorithm has proven to be well-suited for the optimization with one to three variables. A strongly simplified flow chart of the algorithm used to find an optimal biosensor is shown in Figure 3.6. The objective function can be a simple expression as in Equation (3.14) or a more complex one as in (3.15).
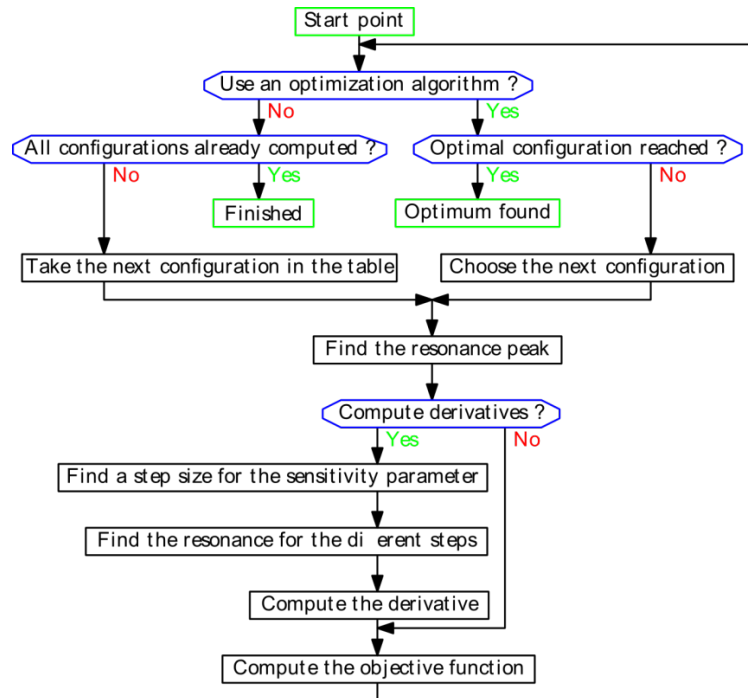

Figure 3.6: Simplified flow chart for finding the optimal sensor sensitivity.

3.6 Results

3.6.1 Film Thickness

The influence of the film thickness h_f on the sensitivity is probably one of the most studied parameters for waveguide grating based biosensors[3,5–8]. Thus, this type of simulation can be used to validate the proposed method. The set values of the individual parameters can be found in Figure 3.1. In the conducted simulations, the film is varied from 90 nm to 254 nm. For all the geometries, the resonance angle (peak position), the peak value (amplitude of the peak), and the derivative of the angle with respect to the refractive index of the sensing layer were computed. The resulting resonance angle and the derivative for FEM

and LIME are plotted in Figure 3.7. The relative energy in the sensing layer has been maximized ($E_{sensing,rel}$ see Equation (3.12)) in order to find the resonance condition (total field FEM). The small differences for the resonance angle can be explained by the fact that the finite grating depth is neglected for the local interference method, resulting in an increased error near the cutoff thickness.

The lower graph of Figure 3.7, the surface sensitivity $\frac{\partial \theta_{res}}{\partial n_I}$ is plotted. For the given parameters, the relative energy is maximal for a film thickness of 121 nm and the sensitivity has a local maximum at 140 nm, implying that the sensitivity is not maximal where the energy is maximal. Again there are some differences near the cutoff due to the lack of accuracy of LIME in this region. For increasing film thicknesses, the difference between FEM and LIME is less than 1% which means that LIME is sufficient if the film thickness is not near the cutoff and if the grating is shallow. Similar results can be found in Refs. 3,5,7 and thus indicates that the proposed method for computing the sensitivity with FEM is valid. The peaks near 186 nm (in Figure 3.7) arise at normal incidence. These erroneous sensitivity peaks result from the fitting algorithm with two Lorentzian peaks and is clearly a weakness of the presented method at normal incidence.
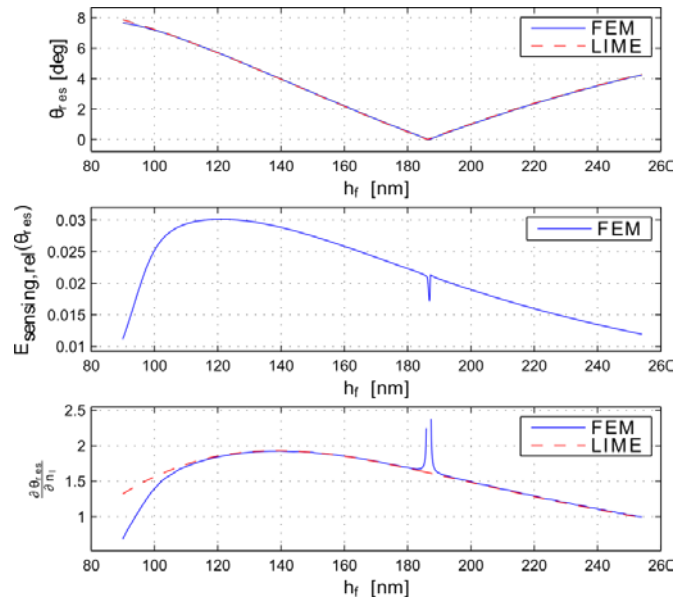

Figure 3.7: Sensitivity for different film thicknesses obtained with FEM and LIME.

3.6.2 Grating Depth

The grating depth has only a small influence on the resonance angle. The sensitivity variation is less than 1% for grating depth from 1 nm to 20 nm. The most important impact of the grating depth is on the full width at half maximum of the resonance peak. This can be seen in Figure 3.8, where the complete peaks are plotted for several different grating depths.

A peak with a narrow full width at half maximum is preferable because it allows an accurate detection of the resonance during the experiments. However, in order to efficiently couple light into the waveguide, a finite grating depth is required. Both, the grating depth and duty-cycle can be used as tuning parameters for the resonance peak shape. These parameters are decoupled since there is no influence of the duty-cycle on the resonance position or the sensitivity. Even if the grating is geometrically shallow, the grating depth should be considered when calculating the sensor response. The grating depth is not the only parameter that has an influence on the peak width, the number of periods[6,17] and the losses also have a significant impact.
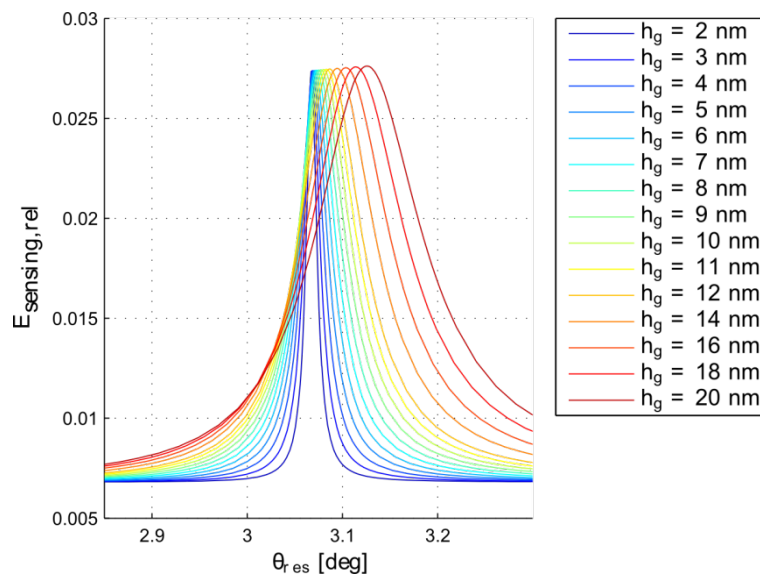

Figure 3.8: Resonance peaks (Lorentzian fits) for different grating depths.

3.6.3 Film Losses

Losses in the cover and the substrate have less influence on the sensor response than losses in the film, which is obvious due to the field distribution of the propagating mode. To simulate inherent waveguide losses, a complex refractive index was introduced, whereas its imaginary part is the extinction coefficient k. The problem is to find an adequate value for the extinction coefficient. Measurements are possible (for example with prism couplers or ellipsometry), but were not available for the investigated chip. It is difficult to find an appropriate value in the scientific literature because the extinction coefficient strongly depends on the production processes (temperature, pressure and film thickness) and on the wavelength of the propagating light.

For Ta_2O_5, the reported k-values vary between $< 10^{-4}$ [20] and 0.02[1]. As explained in Ref. 20, there are also losses at the substrate-film and the film-cover interface. A resulting value of $k = 0.001$ has been chosen for the simulation to compute the resulting peak for the transmission coefficient and total field. Considering losses, the full width at half maximum is no longer 0.001° but about 0.045°, which is a more realistic value. The results are exactly the same with the scattered field formulation. Consequently, an accurate measurement of the losses would be required to faithfully simulate the resonance peak. On the other hand, the resonance angle is not strongly dependent on the losses (less than 0.001°). This implies that the sensitivity can be computed with the model without losses as done above, but is an important parameter to reconstruct the sensor's FWHM.

3.7 Conclusions

A new algorithm, based on FEM, TLTMM and model-based search, has been presented to calculate the sensitivity of a grating based dielectric biosensor. The proposed FEM-based solution scheme has proven its validity by comparing the simulated results with established methods such as LIME and the latter's limitations for large grating depths were shown. For shallow gratings, the two methods are in

very good agreement. The error between the different numerical methods for the position of the resonance angle is smaller than 10^{-5} °.

The presented application examples show that the influence of the grating depth and the film losses can be neglected for the computation of the resonance position and the sensitivity. On the other hand, both have a considerable impact on the FWHM.

A more complex method also exists for the simulation of band gap dielectric frequency-selective surfaces[21]. A similar method combined with the proposed procedure for obtaining the sensitivity could lead to a faster algorithm. Another solution would be to use the multiple scattering approach[9].

Extension of the method for aperiodic gratings and surface roughness has successfully been implemented, for total field and scattered field combined with TLTMM. The only difference for aperiodic gratings is that PMLs are added instead of Floquet periodicity. For the total field formulation, the mode equation is solved (without the grating) and the results are set as the injection boundary condition (simulation of an output coupler). The total field model could probably be adapted to compute more complex excitation schemes than a plane wave.

Additionally, most of the sensor parameters can be taken into account and a global optimization of the chip is possible with a procedure is rather easy to implement with standard simulation software. Since one of the key advantages of grating based biosensors is the number of tuning parameter, the ability to simulate the impact of each design variable is critical.

3.8 References

1.   Schmitt, K., Oehse, K., Sulz, G. & Hoffmann, C. Evanescent field Sensors Based on Tantalum Pentoxide Waveguides – A Review. *Sensors* **8,** 711–738 (2008).

2.   Schmitt, K. & Hoffmann, C. in S*pringer Ser. Chem. sensors Biosens.* (Zourob, M. & Lakhtakia, A.) **7,** 29 (Springer Berlin Heidelberg, 2009).

3.   Cottier, K. Advanced Label-free Biochemical Sensors Based on Integrated Optical Waveguide Gratings. (2004).

4.   Cottier, K., Wiki, M., Voirin, G., Gao, H. & Kunz, R. E. Label-free highly sensitive detection of (small) molecules by wavelength interrogation of integrated optical chips. *Sensors Actuators, B Chem.* **91,** 241–251 (2003).

5.   Kunz, R. E. & Cottier, K. Optimizing integrated optical chips for label-free (bio-)chemical sensing. *Anal. Bioanal. Chem.* **384,** 180–90 (2006).

6.   Kunz, R. E., Dübendorfer, J. & Morf, R. H. Finite grating depth effects for integrated optical sensors with high sensitivity. *Biosens. Bioelectron.* **11,** 653–667 (1996).

7.   Tiefenthaler, K. & Lukosz, W. Sensitivity of grating couplers as integrated-optical chemical sensors. *J. Opt. Soc. Am. B* **6,** 209 (1989).

8.   Cottier, K., Kunz, R. E. & Herzig, H. P. Efficient and Practical Modeling of Finite Waveguide Grating Couplers. *Jpn. J. Appl. Phys.* **43,** 5742–5746 (2004).

9.   Moreno, E., Erni, D., Hafner, C., Kunz, R. E. & Vahldieck, R. Modeling and optimization of non-periodic grating couplers. *Opt. Quantum Electron.* **34,** 1051–1069 (2002).

10.   Chen, C. *Foundations for guided-wave optics*. (John Wiley & Sons, Inc., 2006).

11.   Loewen, Erwin G and Popov, E. *Diffraction gratings and applications*. (CRC Press, 1997).

12.   COMSOL. Plasmonic Wire Grating.

13.   Fernandez, F. & Lu, Y. *Microwave and optical waveguide analysis by the finite element method*. (John Wiley & Sons, Inc., 1996).

14.   COMSOL. RF Module User's Guide.

15.   Oraizi, H. Analysis of planar dielectric multilayers as FSS by transmission line transfer matrix method (TLTMM). *Prog. Electromagn. Res.* 217–240 (2007).

16.   Oraizi, H. & Afsahi, M. Transmission Line Modeling And Numerical Simulasion For The Analysis And Optimum Design Of Metamaterial Multilayer Structures. *Prog. Electromagn. Res. B* **14,** 263–283 (2009).

17.   Brazas, J. & Li, L. Analysis of input-grating couplers having finite lengths. *Appl. Opt.* **34,** (1995).

18.   Maron, M. & Lopez, R. Numerical analysis: a practical approach. (1982).

19.   Horvath, R. *et al.* Analytical and numerical study on grating depth effects in grating coupled waveguide sensors. *Appl. Phys. B* **81,** 65–73 (2005).

20.   Escoubas, L., Tisserand, S. & Gatto, A. Le bilan des pertes dans les couches minces optiques par mesures d'absorption et d'atténuation à la propagation guidée. *J. Opt.* (1998).

21.   Coves, A. *et al.* Analysis and applications of dielectric frequency-selective surfaces under plane-wave excitation. *IEEE Antennas Propag.* **2,** (2003).

3.8 References

4 Experimental Validation of the Sensitivity of Waveguide Grating Based Refractometric (Bio)-sensors[§]

4.1 Abstract

Despite the fact that the theoretical foundations of the sensitivity of waveguide grating based (bio)sensors are well-known, understood and their implications anticipated by the scientific community for several decades, to our knowledge, no prior publication has experimentally confirmed waveguide sensitivity for multiple film thicknesses, wavelengths and polarization of the propagating light. In this chapter, the bulk refractive index sensitivity versus waveguide thickness of said refractometric sensors is experimentally determined and compared with predictions based on established theory. The effective refractive indices and the corresponding sensitivity were determined via the sensors' coupling angles at different cover refractive indices for transverse electric as well as transverse magnetic polarized illumination at various wavelengths in the visible and near-infrared. The theoretical sensitivity was calculated by solving the mode equation for a three layer waveguide.

4.2 Introduction

Waveguide grating based sensors are highly sensitive optical transducers, mainly applied for bulk refractometric or label-free (bio)sensing, to accurately determine the refractive index of a fluid or to detect the interaction, presence and concentration of (bio)molecules[1]. The application areas range from medicine, biotechnology and pharmaceutical industry to food, feed and environmental monitoring[2–7].

Evidently, a key parameter of such a sensor is its sensitivity. It is, therefore, important for the development of a new sensor to choose its overall design and the individual design parameters for a maximized sensitivity. Numerous different, highly sensitive planar waveguide sensor designs have been demonstrated (an overview can be found in Refs. 8–10) and other publications focused on maximizing sensitivity and developing design rules for optimal sensors[1,10–14]. The aim of this chapter is therefore neither to theoretically assess the sensitivity of said sensors nor to maximize it, but to provide experimentally measured data to verify well-established theory regarding the sensitivity of dielectric waveguide grating based (bio)chemical and refractometric sensors. These results have been anticipated for several decades but lack of a systematic experimental verification.

In its simplest configuration, a planar, step-index waveguide grating coupler exhibits a 3-layer structure consisting of the supporting substrate S, a high refractive index waveguide layer F and the investigated cover layer C (Figure 4.1)[2,15,16]. A corrugated grating region in the waveguide acts both as a light coupling element into the waveguide by means of diffraction as well as the sensitive element of the sensor. The sensing principle of a grating coupler can be illustrated by the resonance condition for light coupling into or out of the waveguide via the grating[1,17]:

$$n_{C/S} * sin(\theta_C) = n_{eff} - \frac{m_g \lambda}{\Lambda} \qquad (4.1)$$

where $n_{c/s}$ denotes the refractive index of the cover or the substrate, depending from which side the sample is illuminated, θ_c the coupling angle, m_g the grating diffraction order, λ the vacuum wavelength of the incident light, Λ the grating period and

$$n_{eff} = f(n_c,\, n_f,\, n_s, h_f,\, h_g,\, D,\, \lambda,\, \rho,\, m) \tag{4.2}$$

the effective refractive index of the waveguide, which itself depends on the cover-, waveguide- and substrate refractive indices, the waveguide thickness h_f, the depth h_g and duty-cycle D of the corrugated grating, the wavelength λ and polarization ρ of the incident light, which can either be transverse electric (TE) or transverse magnetic (TM), as well as the mode number m of the propagating wave. Hereinafter, the influence of h_g and D on n_{eff} are neglected as only shallow and, therefore, weak gratings with $h_g << \lambda$ and two conformally corrugated waveguide sides with $D \approx 0.5$ are considered[13].
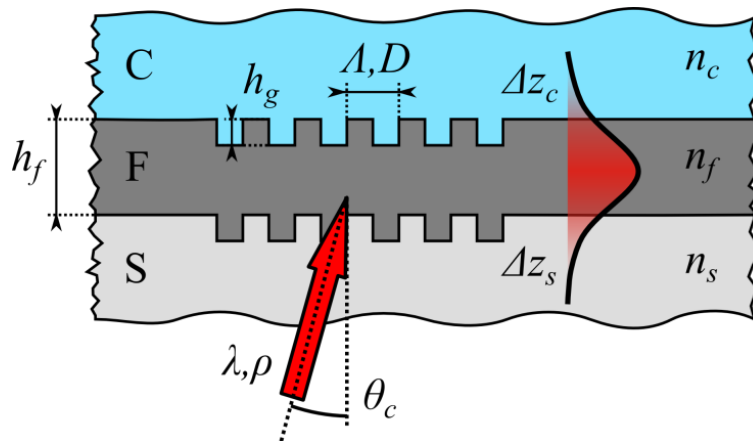

Figure 4.1: Schematic representation of a waveguide grating coupler, consisting of a substrate S, waveguide film F with a layer thickness of h_f and cover layer C with refractive indices n_s, n_f and n_c, respectively. A corrugated grating with a depth of h_g, period Λ and duty-cycle D acts as a coupling element for coherent light with wavelength λ, polarization ρ incident at an angle θ_c, thereby creating a guided mode with evanescent tails with penetration depths Δz_c and Δz_s.

As the coupling angle θ_c depends on n_{eff} (Equation (4.1)), which itself depends on the cover refractive index n_c (Equation (4.2)), changes of the cover refractive index n_c can be monitored by observing the in- or out-coupling angle[1]. As the sensing is accomplished by the evanes-

cent tail of the propagating waveguide mode, the adsorption of molecules can be measured as the cover refractive index is altered in close proximity to the sensor surface, since in general, the adsorbed molecules exhibit a different refractive index than the displaced surrounding cover medium. Thus, a grating coupler can be employed as a (bio)chemical sensor[2]. To enhance the coupling capacity of chemical species to the sensor surface, hydrophilic and open hydrogel matrices with adlayer thicknesses h_{ad} of a few hundreds of nanometers are commonly anchored to the latter[18], thereby covering the entire extent of the evanescent field. In this common case, the sensitivity for surface sensing can be approximated by the sensitivity for homogeneous sensing, where the entire bulk refractive index of the cover changes.

As a consequence of the above, the sensitivity s towards changes in the cover refractive index of said sensor can be expressed as the change of the effective refractive index with respect to the change of the bulk refractive index of the cover medium as defined in Equation (4.3).

$$s = \frac{\partial n_{eff}}{\partial n_c} \approx \frac{\Delta n_{eff}}{\Delta n_c} \tag{4.3}$$

where Δn_c denotes the difference in the refractive index of the cover material and Δn_{eff} the resulting difference in the effective refractive index, which can be calculated with Equation (4.1) from experimentally determined coupling angles.

The sensitivity of a slab waveguide towards cover refractive index changes depends on the fraction of the total power P of the guided mode with respect to the power fraction in the cover P_c[1]:

$$\frac{P_{c/s}}{P} = \frac{n_f^2 - n_{eff}^2}{n_f^2 - n_c^2} \frac{\Delta z_{c/s}}{h_{eff}} \tag{4.4}$$

where $\Delta z_{c/s}$ are the penetration depths of the evanescent field into the cover and substrate layer, respectively, and h_{eff} the effective waveguide thickness:

$$h_{eff} = h_f + \Delta z_c + \Delta z_s \tag{4.5}$$

whereas the penetration depths depend on the polarization ρ of the propagating mode ($\rho = 0$ for TE and $\rho = 1$ for TM modes):

$$\Delta z_{c/s} = \frac{\lambda}{2\pi} (n_{eff}^2 - n_{c/s}^2)^{-\frac{1}{2}} \left[\left(\frac{n_{eff}}{n_f}\right)^2 + \left(\frac{n_{eff}}{n_{c/s}}\right)^2 - 1 \right]^{-\rho} \tag{4.6}$$

After some calculations (as further described in Ref. 1) we can express the sensitivity toward cover refractive index changes as:

$$s = \frac{\partial n_{eff}}{\partial n_c} = \left(\frac{n_c}{n_{eff}}\right)\left(\frac{P_c}{P}\right)\left[2\left(\frac{n_{eff}}{n_c}\right)^2 - 1\right]^{\rho} \tag{4.7}$$

As aforementioned, the goal of this study is to experimentally validate and reconstruct the well-known, theoretical sensitivity plots $s(h_f)$ of waveguide grating couplers for various waveguide thicknesses h_f, wavelengths λ and polarization ρ of the incident light. These can be obtained by numerically solving the transcendental three layer mode equation for n_{eff} and inserting the obtained values in Equation (4.7), as explained in more detail in Subchapter 4.3.2.

4.3 Materials and Methods

4.3.1 Sample Preparation and Measurement of the Refractometric Sensitivity

To determine the sensitivity of a given chip design, the in-coupling angles into the waveguide gratings were measured for different waveguide thicknesses h_f, wavelengths λ and polarization ρ of the incident light as well as cover refractive indices n_c. From the measured in-coupling angles, which were corrected with Snell's law for the change in angle upon refraction at the transition from substrate to air, the effective refractive indices (Equation (4.1)) and the corresponding sensitivity s of the sensor towards change of the bulk refractive index were calculated (Equation (4.3)). In this study, only the case most often met in practice, where $n_c < n_s$, corresponding to an aqueous cover solution and a glass substrate, was considered.
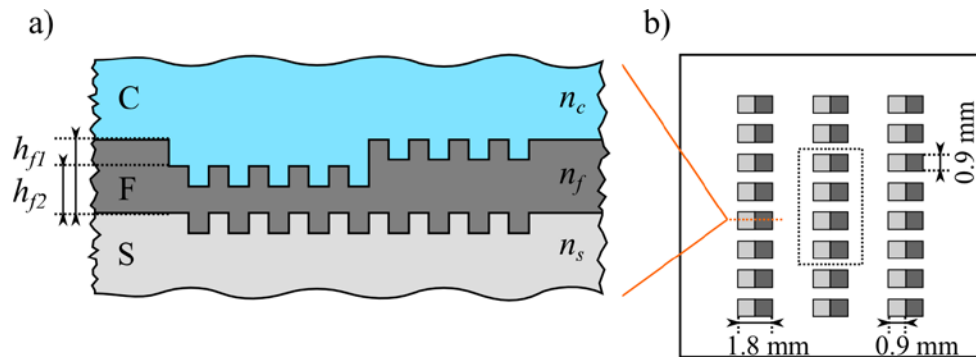
Figure 4.2: Schematic drawing of the investigated waveguide grating chips. (**a**) Cross section (not to scale); (**b**) Top view: Chip with 24 gratings with waveguide thickness h_{f1} and h_{f2}, respectively, whereas the central eight gratings (four of each height) have been considered per measurement per chip.

The waveguide of the investigated sensor consists of a Ta_2O_5 film on a structured glass substrate (D263T by Schott, Mainz, Germany), as schematically depicted in Figure 4.2. To facilitate coupling via the substrate, a broadband anti-reflective coating was deposited on its reverse side. In a second production step, a rectangular grating (0.9 mm by 0.9 mm) was structured into the glass substrate using interference photolithography and reactive ion etching (RIE) in a CHF_3/Ar plasma (Figure 4.3). The developed photoresist was removed by O_2 plasma stripping and subsequently, a first layer of Ta_2O_5 was magnetron sputtered onto the substrate, followed by the deposition of a sacrificial photoresist layer in the regions where a thinner waveguide thickness was desired. A second layer of Ta_2O_5 was sputtered onto the sample thereafter and the production was completed with a lift-off process to uncover the thinner waveguide regions. Average waveguide thicknesses h_f ranging from 83.0 nm ± 0.6 nm to 329.63 nm ± 0.08 nm with a root mean square (RMS) surface roughness of approximately 1.2 nm were produced. The waveguide thicknesses were measured using a spectrometer (Lambda 800, PerkinElmer, Waltham, MA, USA), as well as with a prism coupler (Model 2010, METRICON, Pennington, NJ, USA). The rectangular gratings were produced with a grating depth h_g of 12 ± 2 nm and a grating period Λ of 360 ± 0.1 nm.
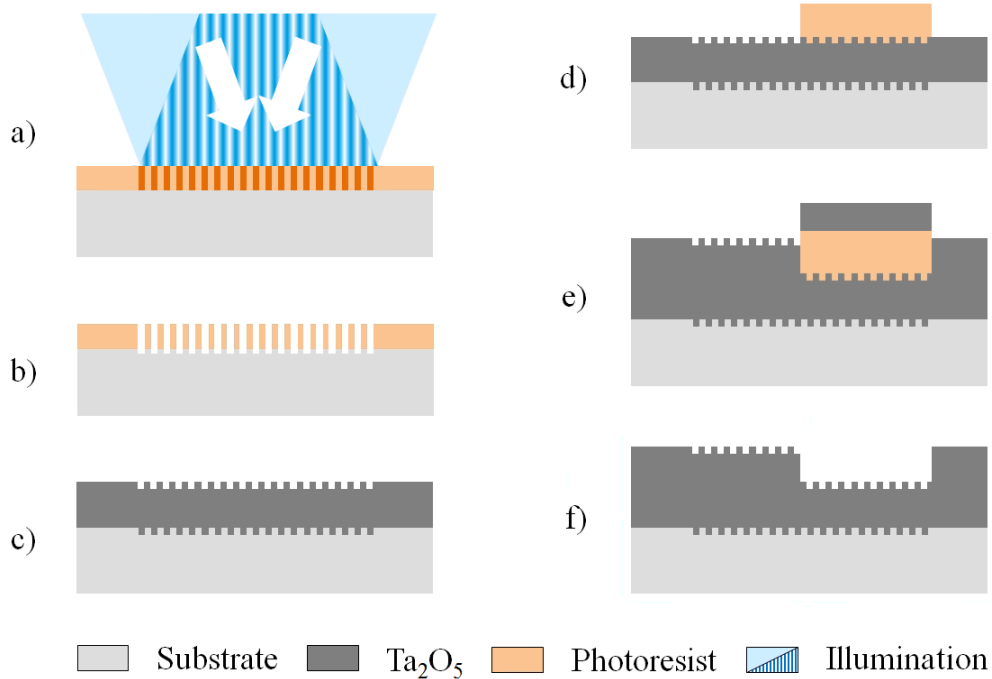
Figure 4.3: Chip production sequence: (**a**) exposure of the deposited photoresist to interference lithography; (**b**) photoresist development and subsequent etching of the substrate by reactive ion etching (RIE); (**c**) O_2 plasma stripping of the photoresist and sputtering of a first Ta_2O_5 layer; (**d**) deposition and structuring of a sacrificial photoresist; (**e**) sputtering of a second Ta_2O_5 layer and (**f**) lift-off of the additional Ta_2O_5 by removing the sacrificial photoresist.

Several samples were examined by atomic force microscopy (AFM) to measure the RMS surface roughness as well as to ensure the envisaged grating structure and confirm the conformity of the two corrugated interfaces *S-F* and *F-C*, which was inherently granted due to the grating's small aspect ratio ($h_g << \Lambda$) (Figure 4.4). This particular chip design with two different waveguide thicknesses is based on the WIOS sensor[19,20], a standard product at Optics Balzers, with the advantage of the production process being readily available, stable and well understood. Whereas the configuration with two adjacent waveguide regions with two different thicknesses is a prerequisite for the WIOS sensor, it was not a requirement for the measurements conducted in the framework of this study, but still beneficial, as two different thicknesses could be investigated at once.
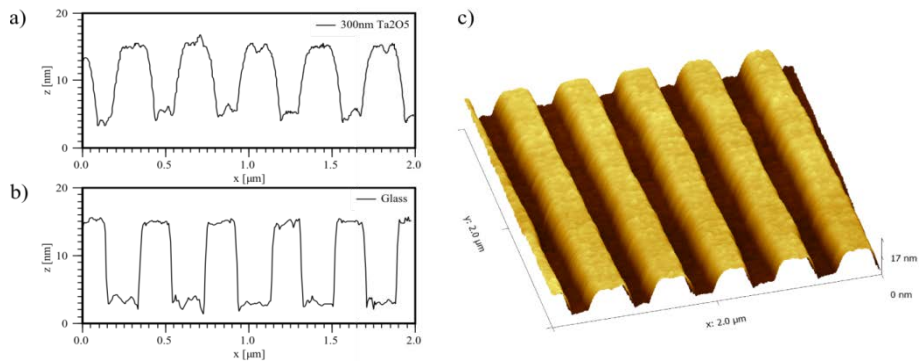
Figure 4.4: By atomic force microscopy (AFM) measured profile of the grating after (**a**) and before (**b**) deposition of ~300 nm Ta_2O_5, together with a topographical scan of the grating (**c**) after deposition. Due to the small aspect ratio of the grating ($h_g << \Lambda$), the structure of the grating is mostly conserved also for thicker Ta_2O_5 layers.

The experimental setup, similar to the one featured in Ref. 21 to study final grating length effects, is sketched in Figure 4.5. The sensor chips were mounted in a transparent PMMA sample holder and different cover media were applied to the corrugated Ta_2O_5 surface. The investigated media included air, purified water (Milli-Q™, EMD Millipore, Billerica, MA, USA) and index matching liquid (Series A, n = 1.52, Cargille Laboratories, Cedar Grove, NJ, USA). The mounted samples were placed on a motorized rotary stage with encoder (CR1/M-Z7, Thorlabs, Newton, NJ, USA) with an angular repeatability of less than 0.017° and an angular resolution of $6 \cdot 10^{-4}$ °. Afterwards, the samples were illuminated through the substrate with linearly polarized light at wavelengths of 532.3 ± 0.2 nm (CW532, Roithner LaserTechnik, Vienna, Austria), 632.8 ± 0.2 nm (1103P, Uniphase, Mateca, CA, USA), 779.7 ± 0.2 nm (LDM780/3LJ, Roithner LaserTechnik, Vienna, Austria) and 845.1 ± 0.2 nm (LDM850/3LJ, Roithner LaserTechnik, Vienna, Austria), according to the available laser sources within the investigated wavelength range. The emission spectra of the laser sources were previously measured with an optical spectrum analyzer (AQ6373, Yokogawa, Musashino, Japan). To determine the in-coupling angle, the angle dependent light transmission through the grating region was measured with a CCD camera combined with a telecentric lens (Guppy F-033B by Allied Vision Technologies, Stadtroda, Germany and 0.5× TML 63074 by Ed-

mund Optics, Barrington, NJ, USA). For every combination of wave-guide thickness, cover refractive index as well as polarization and wave-length of the incident light, 4 out of 24 individual grating regions per chip (Figures 4.2b and 4.6a) were measured in parallel to allow for an accuracy estimate of the determined coupling angles. The angle of inci-dence was swept by turning the mounted sample on the rotary stage, which was controlled via a MATLAB[†] script from an external computer. At the in-coupling angle, the intensity of the transmitted light was de-creased as a part of the incident light was coupled into the waveguide, resulting in a dip in the measured transmitted light intensity versus angle.
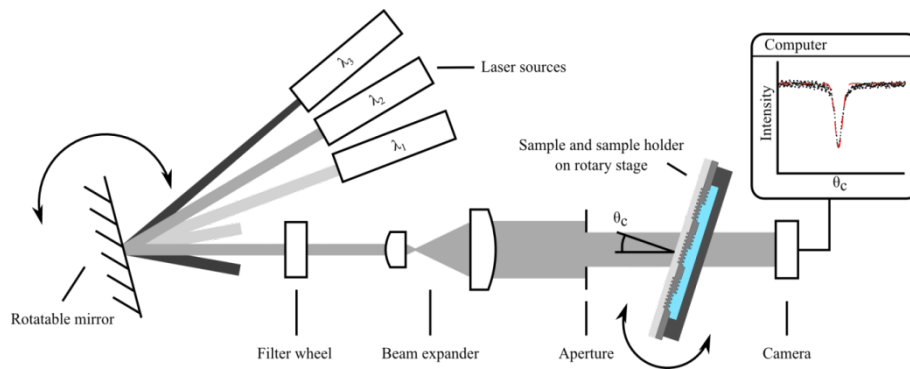

Figure 4.5: Experimental setup to determine the coupling angles consisting of various laser sources, rotatable mirror for source selection, filter wheel with po-larizers for TE and TM polarization selection, beam expander, aperture, the mounted sample on a motorized rotation stage as well as a CCD camera for signal recording.

A typical example of such a measurement is shown in Figure 4.6. Subsequently and in good approximation to the curve, a Gaussian fit was applied to the inverse of the dip and the center of the fit was defined as the in-coupling angle[21]. Since coupling into the waveguide occurs symmetrically around the angle of normal light incidence onto the waveguide (see Equation (4.1)), measurements were performed while turning the rotary stage clockwise (+) as well as counter-clockwise (−) from the angle of normal incidence of the light onto the sample. By evaluating the difference between the resulting positive and

---

[†] MATLAB Release R2010b; The MathWorks, Inc.: Natick, MA, USA, 2010.

negative coupling angles, it was thus possible to precisely calculate the angle of normal light incidence onto the sample and therefore to correct the measured in-coupling angles for an offset.

From the measured in-coupling angles, the effective refractive indices were calculated with Equation (4.1) and subsequently the sensitivity with Equation (4.3) for two different cases; in the first case, the difference Δn_{c1} between air and water, and in the second the difference Δn_{c2} between water and the index matching liquid was evaluated. These measurements were performed with TE and TM polarization of the incident light. Furthermore, only the first two diffraction orders $m_g = \pm 1$ of the grating and excitation of the waveguide's fundamental mode was investigated, according to the coupling condition in Equation (4.1).
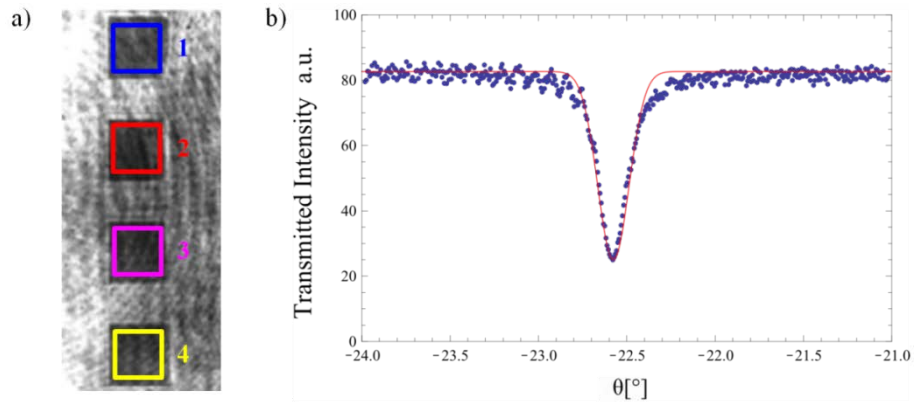

Figure 4.6: Typical measurement of the transmitted light intensity at the coupling angle: (**a**) CCD camera image with the four measurement regions. (**b**) Measured intensity and inverted Gaussian fit for one region to determine the coupling angle. The intensity oscillations are caused by Fresnel reflections at cover and substrate. Configuration: $\lambda = 532.3 \pm 0.2$ nm, $h_f = 122.8 \pm 0.8$ nm, $n_c = 1.5247$.

4.3.2   Calculation of the Theoretical Sensitivity

The theoretical sensitivity was calculated by numerically solving the transcendental three-layer mode equation (Equation (4.8)) to compute n_{eff}

$$\frac{2\pi}{\lambda} \sqrt{n_f^2 - n_{eff}^2}\, h_f + \varphi_c + \varphi_s - m\pi = 0 \qquad (4.8a)$$

where

$$\varphi_{c/s} = -tan^{-1}\left[\left(\frac{n_f}{n_{c/s}}\right)^{2\rho}\frac{\sqrt{n_{eff}^2 - n_{c/s}^2}}{\sqrt{n_f^2 - n_{eff}^2}}\right] \qquad (4.8b)$$

and $m = 0$ for the considered fundamental modes. The measured wavelengths of the incident light were directly fed into Equation (4.8) along with the corresponding refractive indices listed in Table 1. The refractive indices of the liquids were either provided by the manufacturer (for the index matching liquid) or by literature[22]. The refractive index of air was set to $n_{air} = 1.0003$ for all investigated wavelengths[23], whereas the refractive indices of the substrate and the Ta_2O_5 film were determined with the aforementioned prism coupler. With these input parameters the effective refractive indices n_{eff} were calculated for the three different cover refractive indices. Together with the cover refractive index difference, the corresponding sensitivity was calculated with Equation (4.3).

Table 4.1. Refractive Indices of the Sensor Materials at the Investigated Wavelengths.

λ [nm]	n_f	n_s	n_{water}	$n_{index\ matching\ liquid}$
532.3	2.1511	1.5264	1.3354	1.5247
632.8	2.1229	1.5213	1.3321	1.5173
779.7	2.1024	1.5168	1.3290	1.5115
845.1	2.0918	1.5157	1.3279	1.5099

4.4 Results and Discussion

Both measured and calculated sensitivities for the investigated waveguide grating based (bio)sensor are displayed in Figure 4.7 for all measured waveguide thicknesses, wavelengths and polarizations of the incident light. There is a good agreement between the measured data

and the numerical simulations. To quantitatively express the agreement, the root-mean-square deviation (RMSD) of the measured sensitivities from the simulated ones was calculated for every displayed graph in Figure 4.7. The RMSD represents the deviation of the simulated values from the measured ones, or vice versa. On average, the RMSD was 0.006 ± 0.003, which is equal to the average standard deviation of the measured sensitivities. Thus, the accuracy is most probably limited by the achievable resolution of the current measurement setup. Additionally, the Pearson product-moment correlation coefficients (PPMCC) were calculated for all the graphs in Figure 4.7. The PPMCC were ≥ 0.994, except for $\lambda = 845.1 \pm 0.2$ nm and TM polarization with PPMCCs of 0.973 (Δn_{c1}) and 0.984 (Δn_{c2}), signifying that the measured and simulated sensitivities are almost perfectly correlated. Therefore, it can be concluded, that the good agreement between measurements and simulations is supported by the calculated RMSD's and PPMCC's.

Regarding the measured sensitivity values, one can observe that for TE modes, highest sensitivity is achieved in close proximity to the cut-off thickness of the fundamental mode. By contrast, for TM polarization, waveguide layer thicknesses further away from the cut-off in the range of 100 nm to 170 nm exhibit highest sensitivity towards cover refractive index changes for the investigated range of refractive indices, wavelengths and grating structures. In general, it can be concluded that for homogeneous sensing, the fundamental TM mode exhibits a higher sensitivity over the corresponding TE mode for the investigated case where $n_c < n_s$. This can easily be concluded from Equation (4.7) and is in agreement with the literature[1,11,14,24]. For both polarizations, a general trend of decreasing sensitivity for increasing waveguide thicknesses can be observed. By considering Equations (4.4) and (4.5), this can be explained by the power fraction of the mode overlap of the propagating light protruding into the cover medium, which is inversely proportional to the effective waveguide thickness h_{eff}. Therefore, with increasing h_{eff}, the sensitivity approaches zero as $P_c/P \rightarrow 0$ (Ref. 1). In addition, one can observe that for high refractive indices of the cover materials, in this work the measurement of water-index matching liquid,

the sensitivity is increased compared to using cover media with lower refractive indices. This is a direct consequence governed by Equation (4.6), as the evanescent field in the cover medium Δz_c tends towards infinity as $n_{eff} \rightarrow n_G$ resulting in a maximized fraction of total power in the cover medium ($P_C/P \rightarrow 1$).
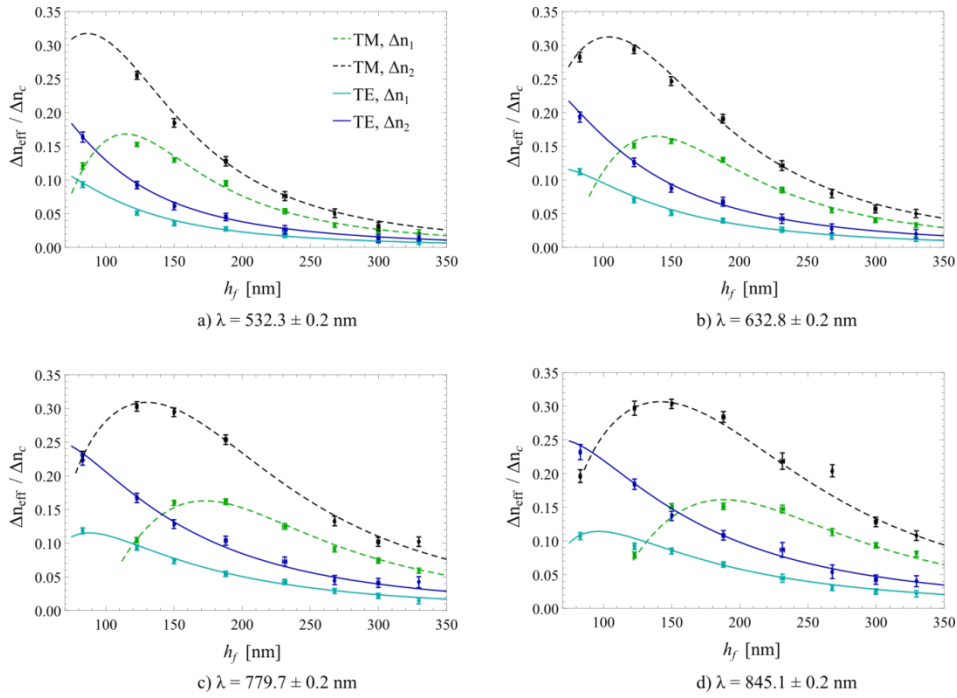

Figure 4.7: Measured (marks) and calculated sensitivities (lines) for transverse magnetic (TM) and transverse electric (TE) polarization at the four investigated wavelengths of the incident light. All error bars (standard deviations of all measured values) were plotted but some are barely discernible due to their small value.

As mentioned in the introduction, the aforesaid findings only hold true for homogeneous, refractometric sensing and for biosensing with 3D immobilization matrices with thicknesses in the range of or bigger than the evanescent field's penetration depth ($h_{ad} \geq \Delta z_c$). The case of surface or thin-layer sensing ($h_{ad} << \Delta z_c$) has been investigated theoretically as well as experimentally in Refs. 1,11,14,25, although the conditions for maximum sensitivity are close to the homogeneous case. A normalized analysis for the sensitivity optimization of waveguide-based sensors can be found in Ref. 14.

It should also be mentioned that the investigated cover refractive index changes are substantially bigger than in typical sensing applications, where the effect of adsorbing biomolecules on the cover refractive index is several orders of magnitude smaller. Nevertheless, this does not contradict the abovementioned calculations. If all parameters are known (which is the case here), the effective refractive index n_{eff} is unambiguously defined via Equation (4.2). For the calculation and measurement of n_{eff} with one cover medium, no parameters of the second cover medium are required. Therefore, these calculations are decoupled and the magnitude of Δn_c has no influence on the accuracy of the determination of the effective refractive indices and the derived sensitivity (Equation (4.3)).

4.5 Conclusions

In this publication, the refractometric sensitivity of waveguide grating sensors was experimentally determined for different waveguide thicknesses, wavelengths and polarizations of the incident light and compared with numerical calculations to verify well-established theory.

A good agreement between theoretically calculated and experimentally measured sensitivity was observed. The RMSD's of the measured values from the simulated values are in the same order of magnitude as the experimental uncertainty of the measured sensitivities. Further, a very good correlation between the measured and simulated sensitivities was observed, yielding PPMCC's above 0.97. Therefore, it can be concluded that the sensitivity of the coupling angle towards change of the bulk refractive index can accurately and reliably be modeled with established theory. Hence, this study aims at filling a gap in the published literature by experimentally reconstructing the sensitivity curves for waveguide grating coupler based sensors and it confirms the validity as well as the accuracy of the theoretical predictions for various illumination wavelengths, polarizations, waveguide thicknesses and refractive indices of the cover medium.

4.6   Acknowledgments

4.7   References

1.   Tiefenthaler, K. & Lukosz, W. Sensitivity of grating couplers as integrated-optical chemical sensors. *J. Opt. Soc. Am. B* **6,** 209 (1989).

2.   Nellen, P. M., Tiefenthaler, K. & Lukosz, W. Integrated optical input grating couplers as biochemical sensors. *Sensors and Actuators* **15,** 285–295 (1988).

3.   Cooper, M. a. Optical biosensors in drug discovery. *Nat. Rev. Drug Discov.* **1,** 515–528 (2002).

4.   Pasche, S. *et al.* Integrated optical biosensor for in-line monitoring of cell cultures. *Biosens. Bioelectron.* **26,** 1478–1485 (2010).

5.   Adrian, J. *et al.* Waveguide interrogated optical immunosensor (WIOS) for detection of sulfonamide antibiotics in milk. *Biosens. Bioelectron.* **24,** 3340–3346 (2009).

6.   Bier, F. F. & Schmid, R. D. Real time analysis of competitive binding using grating coupler immunosensors for pesticide detection. *Biosens. Bioelectron.* **9,** 125–130 (1994).

7.   Vörös, J. *et al.* Feasibility study of an online toxicological sensor based on the optical waveguide technique. *Biosens. Bioelectron.* **15,** 423–429 (2000).

4.7 References

8. Schmitt, K., Oehse, K., Sulz, G. & Hoffmann, C. Evanescent field Sensors Based on Tantalum Pentoxide Waveguides – A Review. *Sensors* **8,** 711–738 (2008).

9. Kozma, P., Kehl, F., Ehrentreich-Förster, E., Stamm, C. & Bier, F. F. Integrated planar optical waveguide interferometer biosensors: A comparative review. *Biosens. Bioelectron.* **58,** 287–307 (2014).

10. Lukosz, W. Integrated optical chemical and direct biochemical sensors. *Sensors Actuators B Chem.* **29,** 37–50 (1995).

11. Kunz, R. E. & Cottier, K. Optimizing integrated optical chips for label-free (bio-)chemical sensing. *Anal. Bioanal. Chem.* **384,** 180–90 (2006).

12. Guillod, T., Kehl, F. & Hafner, C. C. FEM-based Method For The Simulation Of Dielectric Waveguide Grating Biosensors. *Prog. Electromagn. Res.* **137,** 565–583 (2013).

13. Kunz, R. E., Dübendorfer, J. & Morf, R. H. Finite grating depth effects for integrated optical sensors with high sensitivity. *Biosens. Bioelectron.* **11,** 653–667 (1996).

14. Parriaux, O. & Veldhuis, G. J. Normalized analysis for the sensitivity optimization of integrated optical evanescent-wave sensors. *J. Light. Technol.* **16,** 573–582 (1998).

15. Tiefenthaler, K. & Lukosz, W. Grating couplers as integrated optical humidity and gas sensors☆. *Thin Solid Films* **126,** 205–211 (1985).

16. Lukosz, W., Nellen, P. M., Stamm, C. & Weiss, P. Output grating couplers on planar waveguides as integrated optical chemical sensors. *Sensors Actuators B Chem.* **1,** 585–588 (1990).

17. Tamir, T. & Peng, S. T. Analysis and design of grating couplers. *Appl. Phys. A Mater. Sci.* **254,** 235–254 (1977).

18. Löfås, S. & Johnsson, B. A novel hydrogel matrix on gold surfaces in surface plasmon resonance sensors for fast and efficient covalent immobilization of ligands. *J. Chem. Soc.* 1526–1528 (1990).

19. Wiki, M. & Kunz, R. E. Wavelength-interrogated optical sensor for biochemical applications. *Opt. Lett.* **25,** 463–465 (2000).

20.   Cottier, K., Wiki, M., Voirin, G., Gao, H. & Kunz, R. E. Label-free highly sensitive detection of (small) molecules by wavelength interrogation of integrated optical chips. *Sensors Actuators, B Chem.* **91,** 241–251 (2003).

21.   Brazas, J. & Li, L. Analysis of input-grating couplers having finite lengths. *Appl. Opt.* **34,** (1995).

22.   Daimon, M. & Masumura, A. Measurement of the refractive index of distilled water from the near-infrared region to the ultraviolet region. *Appl. Opt.* **46,** 3811–3820 (2007).

23.   Ciddor, P. E. Refractive index of air: new equations for the visible and near infrared. *Appl. Opt.* **35,** 1566–1573 (1996).

24.   Schmitt, K. & Hoffmann, C. in *Springer Ser. Chem. sensors Biosens.* (Zourob, M. & Lakhtakia, A.) **7,** 29 (Springer Berlin Heidelberg, 2009).

25.   Ramsden, J. J., Lvov, Y. M. & Decher, G. Determination of optical constants of molecular films assembled via alternate polyion adsorption. *Thin Solid Films* **254,** 246–251 (1995).

4.7 References

5 Angle Interrogated Optical Sensor (ARGOS): A MEMS-based, Label-free, Waveguide Grating Biosensor System[**]

5.1 Abstract

The presented label-free optical biosensor system relies on a MEMS micro-mirror to interrogate waveguide grating regions at a high repetition rate in the kHz range by scanning the angle of the incident coherent light. The angle-tunable MEMS mirror permits an extended scanning range and offers the flexibility to measure at various wavelengths and optical powers - an interesting feature for an enhanced surface-to-bulk sensitivity ratio and extended, multiplexed sensor arrays.

An excellent refractometric sensitivity with a limit of detection of $\Delta n_{eff} <$ 2 x 10^{-7} and long-term stability ($<10^{-6}$ min^{-1}) is reported, as well as the capability to perform affinity measurements for large (>150 kDa) and small (<250 Da) molecules. With fully-integrated optics, electronics and fluidics, the compact, low-power and affordable sensor unit is well-suited for in-situ environmental monitoring or point-of-care diagnostics.

5.2 Introduction

Label-free, dielectric waveguide based biosensors are well-known integrated-optical transducers to determine the presence, concentration and interaction of surface-bound (bio)molecular species[1]. Said sensors are commonly used in various fields such as the pharmaceutical industry[2], in biomedical and forensic applications, as well as food, feed[3] and environmental monitoring[4]. Miscellaneous interferometric[5] and resonant[6] transducer configurations have been presented. Waveguide grating couplers represent a subcategory of the latter group and different angular and spectral interrogation schemes for in- and output grating couplers are known[7–11]. Here, a novel readout concept based on a scanning MEMS (micro-electro-mechanical system) mirror for the angular interrogation of input grating couplers at a high repetition rate is presented. The main advantages of the introduced configuration are high sensitivity and stability, large, tunable dynamic range, flexibility regarding the interrogating light source, compact size, low weight and comparatively low cost.

After a brief introduction of the theoretical fundamentals of waveguide grating sensors, the interrogation scheme will be described and the properties of the presented configuration will be assessed in greater detail. The practical realization of the sensor device and the conducted experimental characterization will be detailed, which will then be summarized and concluded in the subsequent paragraphs.

Common planar optical waveguides exhibit a three-layer structure with a high refractive index film F between a supporting substrate S and a cover medium C. The waveguide film acts as a conduit for the propagating light by means of total internal reflection. Light can be coupled in and out of the waveguide via diffractive gratings, formed by a periodic corrugation of the waveguide film[12,13]. The guided mode is excited with maximal efficiency if light impinges the grating at the coupling angle θ_c when the coupling condition

$$n_a \cdot sin(\theta_c) = n_{eff} - \frac{m_g \lambda}{\Lambda} \tag{5.1}$$

is fulfilled, where Λ denotes the grating period, λ the vacuum wavelength of the propagating light, m_g the grating diffraction order, n_a the refractive index of the ambient medium and n_{eff} the waveguide's effective refractive index. The effective refractive index n_{eff} depends on various parameters

$$n_{eff} = f(n_c, n_f, n_s, h_f, \lambda, \rho) \tag{5.2}$$

such as the refractive index and thickness of the waveguide film n_f and h_f, the wavelength λ and polarization ρ of the incident light and again the substrate and cover refractive indices n_s and n_c. Any changes in the latter will affect n_{eff} and via Equation (5.1) alter the angle θ_c at which light will be coupled into or out of the waveguide[13]. The grating therefore not only acts as a light coupling element but also as a sensitive, refractometric transducer. Since, in general, (bio)molecules adsorbing to the sensor surface exhibit a different refractive index than the displaced cover medium, waveguide grating couplers can be used as highly sensitive, label-free optical sensors. The described structure and relevant parameters of a common waveguide grating coupler are illustrated in Figure 5.1.
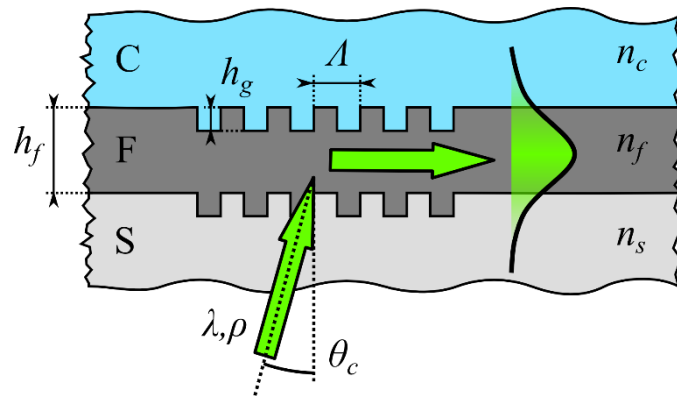

Figure 5.1: Schematic representation of a common waveguide grating coupler, consisting of a substrate S, waveguide film F with a layer thickness of hf and cover layer C with refractive indices n_s, n_f and n_c, respectively. A corrugated grating with a depth of h_g and period Λ acts as a coupling element for the incident coherent light with wavelength λ, polarization ρ impinging at the coupling angle θ_c, thereby creating a guided mode.

5.3 Materials and Methods

The presented system relies on a waveguide grating coupler sensor chip as the optical transducer, produced at Optics Balzers AG (Balzers, Liechtenstein), consisting of a borosilicate glass substrate (D263T by Schott, Mainz, Germany, n_s = 1.53, all refractive indices expressed at λ = 532 nm) and a tantalum-pentoxide Ta_2O_5 waveguide (n_f = 2.15). The sensor chip with an outer dimension of 17.75 x 17.75 x 0.7 mm^3 possesses 24 corrugated grating regions with a grating period Λ of 360 ± 0.1 nm and a grating depth h_g of 12 ± 2 nm, as depicted in Figure 5.2 with a schematic top (a) and side (b) view.
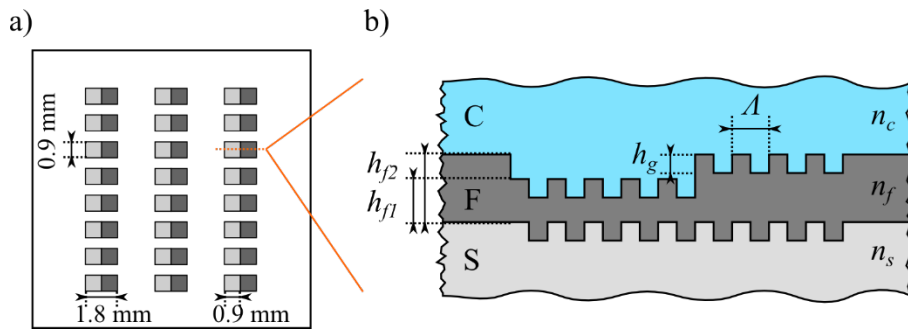

Figure 5.2: Schematic top (**a**) and side view (**b**) of the waveguide grating sensor chip, with a thinner (h_{f1}) in-coupling and thicker (h_{f2}) out-coupling grating region (not to scale).

The grating was produced by interference lithography and directly dry-etched into the substrate by using reactive ion etching (RIE) in a CHF_3/Ar plasma. The developed photoresist was removed by O_2 plasma stripping, followed by the magnetron sputtered deposition of the Ta_2O_5 waveguide[14,15]. The sensitive grating areas are divided in two adjacent regions, each with a lateral extent of 0.9 x 0.9 mm^2, whereas they only differ in the waveguide film thickness h_f. The thinner grating region with a film thickness of h_{f1} = 82 ± 2 nm serves as an in-coupling grating and is designed for maximal sensitivity towards refractive index changes[15–18]. The second grating with a film thickness of h_{f2} = 232 ± 2 nm acts as an out-coupling element for the propagating light. This feature was produced by the deposition of a sacrificial photoresist layer in the regions where a thinner waveguide thickness was desired, followed

by sputtering a second layer of Ta_2O_5 and a subsequent lift-off process to uncover the thinner waveguide regions. By having two different film thicknesses for the two gratings, the out-coupled beam emerges from the chip at a different angle than the otherwise interfering reflection of the in-coupled beam, which could also be solved by having grating regions with different periods[19].

In the here introduced angle interrogated optical sensor (ARGOS) system, the chip is illuminated by a collimated beam with a diameter of 15 mm of a temperature and current stabilized diode pumped solid state laser source at an emission wavelength of 532 nm (DJ532-10, Thorlabs, Newton, NJ, USA). Various lasers with different wavelengths (λ = 532, 633 nm, 780 nm, 850 nm) and optical powers (P_{em} = 0.5 – 20 mW) have been implemented and tested as described by our previous work[15]. The DJ532-10 was chosen due to its favorable combination of spectral stability, narrow linewidth, short wavelength, optical power, compact size and reasonable cost. Impinging at the coupling angle of the in-coupling grating θ_{G}, the incident coherent light is exciting the fundamental transverse magnetic mode (TM_0) of the waveguide, which is subsequently coupled out of the latter through the second grating onto a light sensitive photodiode (SFH250V, Avago Technologies, San Jose, CA, USA). The interrogation principle is illustrated in Figure 5.3.
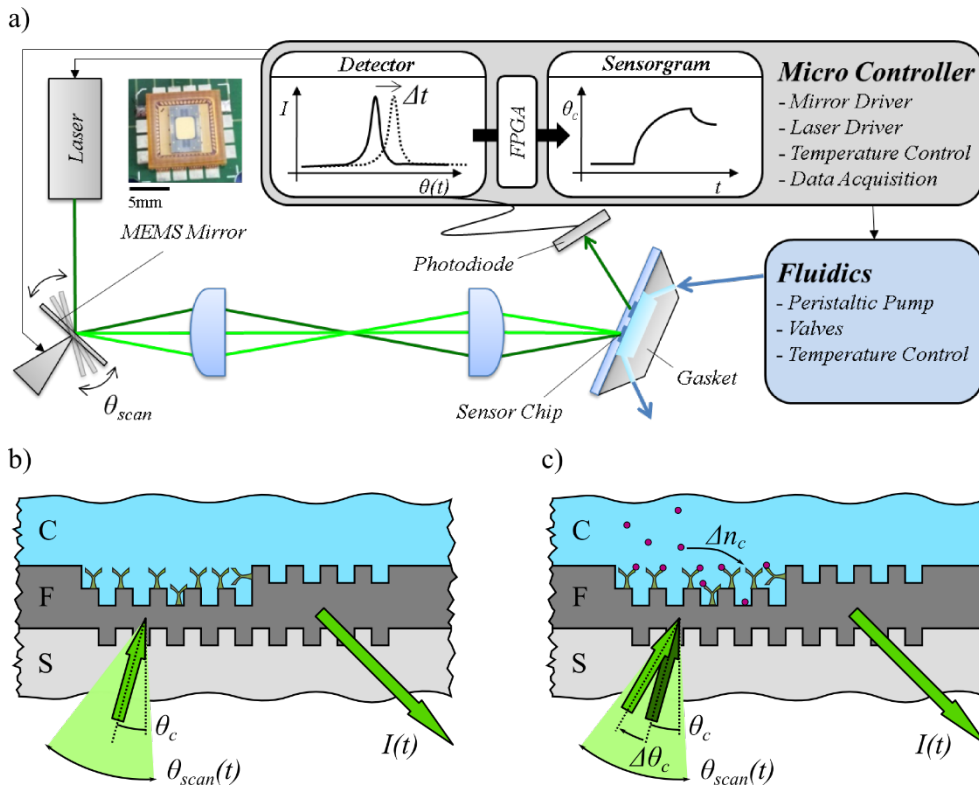
a)

b)   c)

Figure 5.3: The angle of the incident laser light is constantly scanned by an angle of θ_{scan} around the in-coupling angle θ_c by a MEMS mirror (a). A 4f optical system consisting of two plano-convex lenses redirects the collimated beam onto the sensor chip. At $\theta_{scan} = \theta_G$ light couples into the waveguide and exits through the second grating onto a light sensitive photodiode (b), resulting in an intensity peak $I(t)$ on the detector side. Refractive index changes due to the adsorption of molecules on the sensor surface lead to a change in coupling angle $\Delta\theta_G$, which can be monitored by a temporally shifted intensity signal $I(t_i \pm \Delta t)$ (c). Plotting of the resonance peak position over time $\theta_c(t)$ results in the desired sensorgram. Custom electronics control critical components such as the laser, MEMS mirror, pumps and valves to apply the investigated liquid samples and for the acquisition of the sensorgram via FPGA.

For sensing purposes, the in-coupling angle is monitored by constantly scanning the angle of incidence of the impinging light, which is accomplished via an oscillating, electrostatically driven MEMS mirror (2.5 x 3 mm^2, BA0050, Opus Microsystems, Taiwan) and a 4f optical configuration to guarantee beam collimation and expansion to a diameter of 15mm to cover all waveguide grating regions. This time-dependent detuning of the incident angle $\theta_{inc}(t)$

$$\theta_{inc} = \frac{\theta_{scan}}{2} \, sin(2\pi ft) + \theta_0 \qquad (5.3)$$

where θ_{scan} equals the scan range or twice the mirror's oscillation amplitude (typically < 1 degree), which can be tuned by the mirror driving controls, and θ_0 the initial angle of incidence (which is set to θ_c at the beginning of a measurement), results in a time-dependent, varying light intensity profile $I(t)$ (resonance peak) on the detector side. Maximal coupling efficiency I_{max} occurs at $\theta_c = \theta_{inc}(t_i)$, where $t_i = i/(2f)$, with $i \in \mathbb{N}$ enumerating the sampled peaks, whereas f denotes the MEMS mirror's oscillation frequency, typically $f \approx 1$ kHz.

Since the coupling angle depends on the cover refractive index $\theta_c(n_c)$ (Equations 5.1 and 5.2), changes Δn_c in the latter will cause a shift of the coupling angle $\Delta\theta_c$. Due to the fact that the incident angle $\theta_{inc}(t)$ of the interrogating light is a function of time t (Equation 5.3), coupling into the waveguide is temporally shifted to $t_i \pm \Delta t$, which can easily be measured by a time shifted intensity signal $I_{max}(t_i \pm \Delta t)$ of the out-coupled beam. The sinusoidal movement of the mirror and the resulting resonance peak on the detector at $\theta_c = \theta_{inc}$ is plotted in Figure 5.4. The magnitude of Δt is therefore directly related to the cover refractive index change Δn_c and can be approximated as given in Equation (5.4).

$$\Delta n_c = const \cdot \Delta t \qquad (5.4)$$

The constant factor was experimentally deduced as will be described later in the present report. Custom electronics allow to amplify the optical signal and quantify its temporal shift Δt by triggering on the rising and falling edge of the resonance peak with a field programmable gate array (FPGA) at an acquisition rate of 400 MHz. The final system and its components are depicted in Figure 5.5. For the interested readers, the authors would like to refer to a more detailed, technical description of the system and its components in the Chapter's Appendix.
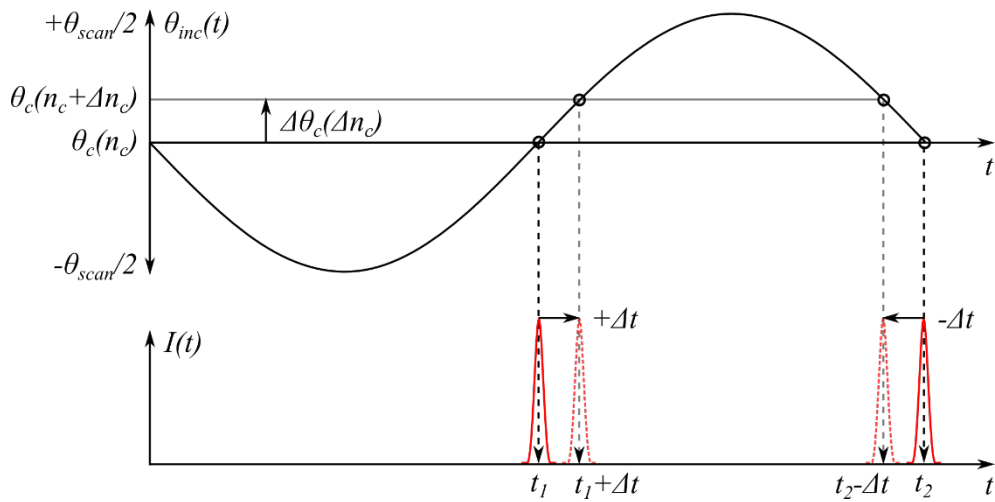
Figure 5.4: Interrogation of the coupling angle θ_c is accomplished by a sinusoidal scan trajectory of the MEMS mirror and the resulting sinusoidal angle change $\pm\, \theta_{scan}/2$ of the incident light θ_{inc} (upper graph). When $\theta_{inc} = \theta_c$ (small circles), light will be coupled into the waveguide and out onto the detector, resulting in a resonance peak (lower graph). Changes in the cover refractive index Δn_c lead to a shift of the resonance angle from $\theta_c(n_c)$ to $\theta_c(n_c+\Delta n_c)$ by $\Delta\theta_c$, which can be monitored by a time-shifted intensity signal $I(t_i \pm \Delta t)$ on the detector side.
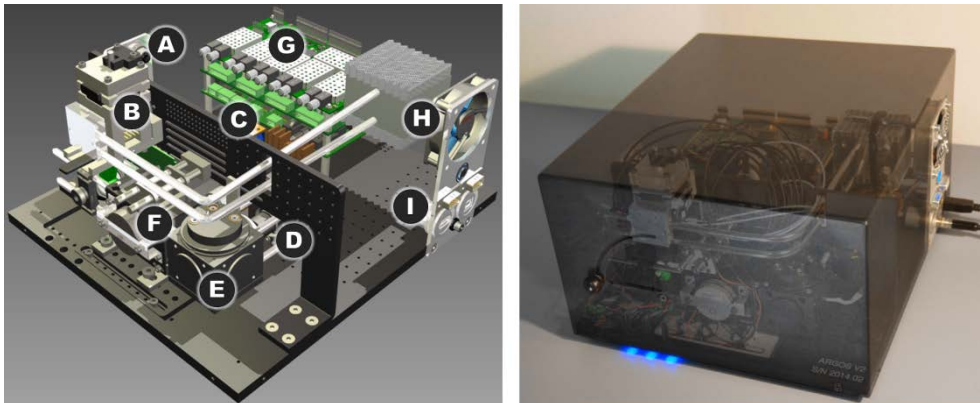

Figure 5.5: ARGOS system overview. **Left**: CAD model with sample inlet (**A**), temperature stabilized chip bay and flow-cell (**B**), T-valves (**C**), laser (**D**), MEMS mirror mounted in optical cage cube (**E**), 4f-optics (**F**), associated electronics for control and acquisition (**G**), thermal management (**H**) and electrical connections (**I**). **Right**: Overlay of two photographs (with and without cover hood) of the ARGOS system.

The sample was applied to the sensor in the liquid phase by an external peristaltic pump (Ismatec IPC, IDEX SA, Switzerland) via a temperature stabilized flow-cell, directly mounted to the chip, as sketched in Figure 5.3. Keeping the sensor at constant temperature (<±0.01°C) is a key requirement, not only to guarantee equal conditions during the measurements, but also to avoid major signal drift due to the thermo-optic coefficient of the sample itself[20] and the transducer's dielectrics[21]. The materials wetted by the sample were inert polymers such as poly-tetrafluoroethylene (PTFE), polyether ether ketone (PEEK), ethylene propylene diene monomer (EPDM) as well as the chip surface itself. The elastic, black EPDM gasket with laser ablated channels was mechanical-ly pressed onto the chip to form two individual flow channels (~100 μm in height, 1 mm wide), one for surface-bound (bio)molecular species measurement and one for signal referencing[22]. The gasket's low albedo reduces interfering reflection and stray light from the transmitted frac-tion of the incident beam.

Successive application of the individual liquid samples through the flow channels onto the sensor element with constant flow is not straightforward, as will be explained hereinafter. Direct contact of the sensor area with air needs to be avoided during the course of a meas-urement due to the associated signal baseline shift. Applying two liq-uids "A" and "B" with corresponding concentrations [A] and [B] con-secutively to the sensor surface in a linear flow channel would entail direct contact of the two fluids. In this case, due to diffusion and Taylor-Aris-dispersion[23–25] at the liquid-liquid interface, an undesired concen-tration gradient would arise at the front-end of the sample inlet, as il-lustrated in Figure 5.6.
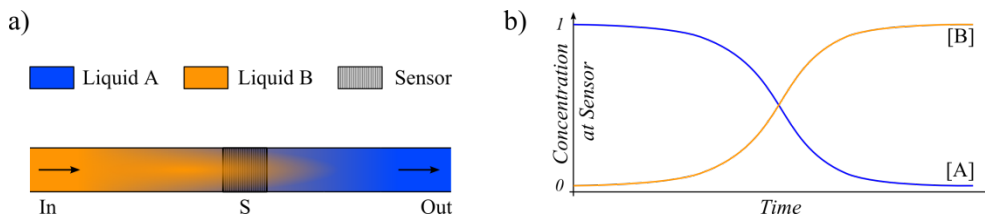

Figure 5.6: Schematic representation of a linear flow channel (**a**) with undesired concentration gradient due to direct contact of liquid A and B (**b**).

5.3 Materials and Methods

....

To adequately deduce the binding kinetics of the adsorbing species to its tethered binding partner on the transducer surface, the fluidic system is required to instantly apply the compounds at their designated and final concentration[1]. The chosen method was to separate the sequent samples by means of an air bubble and by-pass the latter via a waste channel, avoiding direct contact of the air with the sensor area. A T-junction, integrated in the EPDM seal, splits both channels into a measurement and waste channel, which recombine at the back-end with a bi-stable, solenoid driven T-valve. The valve's initial position allows the first sample A to flow via the sensor grating to the outlet. An inline, non-invasive bubble detector (BD_1) registers the separating bubble and switches the valve to redirect the flow via the waste channel. Due to the hydrostatic back pressure and the incompressibility of the liquid sample, the flow is hindered to enter the measurement channel and only a minute mixing of the two samples occurs at the liquid-liquid interface because of the shallow channel. As soon as the air plug by-passes the second bubble detector (BD_2) and sample *B* reaches the latter, the valve automatically switches to its initial position and instantly exposes the sensor to sample *B*. The mechanism's working principle is presented in Figure 5.7

Although the sensor is optimized and designed for maximal response towards thin layer sensing through the adsorption of (bio)molecules onto the sensor surface, system characteristics such as limit of detection (LoD), noise and drift are commonly investigated by bulk refractometric measurements[26]. Instead of binding molecules to the sensor surface, the entire cover medium is replaced by a liquid with a different refractive index. Aqueous solutions of glycerol can be used to vary the cover refractive index from pure water (n_{water} = 1.336) to pure glycerol ($n_{glycerol}$ = 1.474)[27,28]. Besides the well characterized, almost linear dependency of the glycerol concentration on the refractive index for aqueous solutions[29], glycerol does not possess characteristic absorption lines at 532 nm, is not optically active nor is it known to interact with the dielectric waveguide.
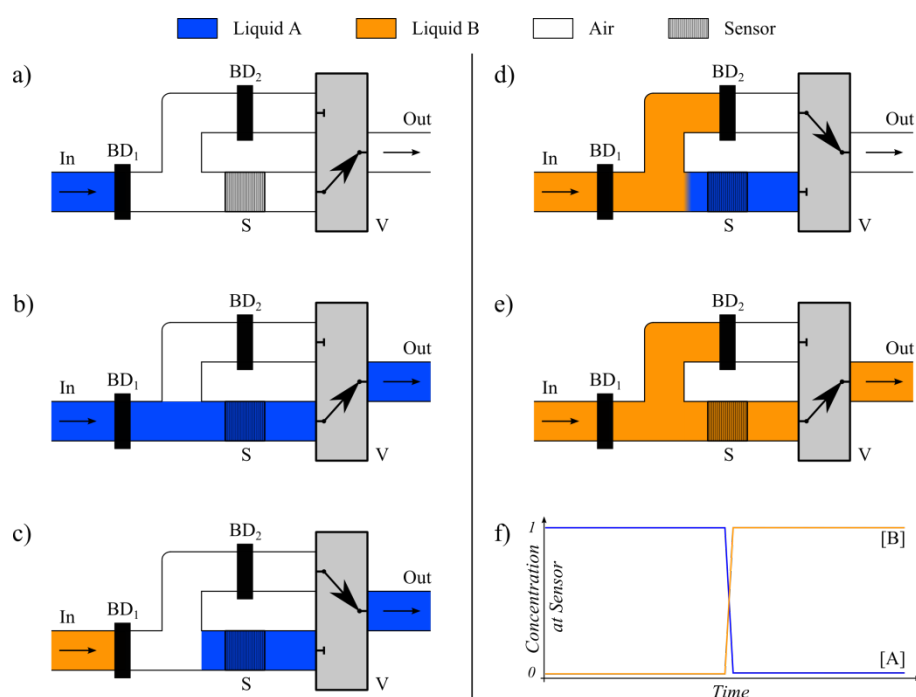
....

Figure 5.7: Sketch of the sample injection mechanism: sample *A* is entering the flow channel (**a**) and is directed by the T-valve *V* to the outlet via the sensor pad *S* (**b**). The air bubble separating the two liquids is detected by the first bubble detector (BD₁) (**c**), hereby switching the valve and redirecting liquid *B* over the by-passing waste channel (**d**). As soon as liquid *B* arrives at the second bubble detector (BD₂), the valve switches back to its initial position and applies liquid *B* on the sensor (**e**), resulting in a fast sample transition (**f**).

Despite the fact that the refractometric and, therefore, physical performance of the sensor system can diligently be characterized by glycerol injections, it has no relevance to actual bioaffinity measurements, namely the binding of, or adsorption to, molecules immobilized on the sensor surface. To convert the instrument's response units into a comprehensible, physical quantity, such as surface mass density $\mathcal{M}$ expressed in pg/mm^2, positively charged PLL-g-PEG-biotin[†] (0.1 mg/ml PLL-g-PEG-biotin in 1 mM HEPES buffer pH 7.3) was adsorbed to the bare, negatively charged Ta_2O_5 surface[30–32]. The resulting peak shift,

---

[†] Poly(L-lysine)-g-poly(ethylene glycol)-biotin. (PLL(20)-g[3.5]- PEG(2) / PEG(3.4)- biotin(18%): PLL(20 kDa) grafted with PEG(2 kDa) and PEG-biotin (3.4 kDa), g = 3.0 to 4.0 (Lys units /PEG chains) and percentage of biotin functionalized PEG is 18%), SuSoS AG, Switzerland.

5.3 Materials and Methods

....

measured in nanoseconds, was compared with the quantified signal response of the OWLS system[33] (MicroVacuum, Hungary) by binding the identical polymer to the same oxide surface.

The specificity to a certain targeted analyte is solely determined by the immobilization of the corresponding receptor molecule to the sensor surface. Consequently, countless binding assays can be realized whenever a specific receptor molecule-analyte couple exists. Here, the system performance was assessed by direct, specific binding assays for a large (Immunoglobulin-G (IgG), approx. 160 kDa) as well as for a small molecule (Acetazolamide (222.2 Da)). For this purpose, the waveguide grating chips were previously coated with a 200 nm thick carboxylic hydrogel (HC200m, XanTec GmbH, Germany). This linear, synthetic polycarboxylate embeds the receptor molecule in a 3-dimensional, tethered sensing layer. Immobilization of the receptor molecule to the latter was accomplished via amine coupling to the hydrogel's carboxylic groups upon activation with a mixture of 0.4 M EDC / 0.1 M NHS in 50 mM MES buffer, pH 5.0 (EDC: N-ethyl-N'-(dimethylaminopropyl) carbodiimide hydrochloride, NHS: N-hydroxysuccinimide, MES: 2-(N-morpholino) ethane sulfonic acid. All from XanTec)[34]. For all bioassays, sensors with a waveguide layer thickness at the in-coupling grating of 150 nm (standard product at Optics Balzers) were used.

To detect a representative of the group of large molecules, 0.2 mg/ml of mouse-IgG (Jackson ImmunoResearch Europe Ltd., United Kingdom) in deionized water were applied and covalently immobilized to the aforementioned, activated surface. DI-water was chosen for the immobilization step to prevent the electrostatic shielding of charged groups by dissolved ions. After a brief washing step with DI-water, the remaining activated carboxylic groups were saturated with a quenching buffer (1 M ethanolamine hydrochloride, pH 8.5) for 20 min. Subsequently, various concentrations of goat-anti-mouse-IgG (Jackson, UK) in PBS (Phosphate buffered saline, pH 7.4, Sigma-Aldrich, United States) ranging five orders of magnitude from 500 pM to 5 μM were applied to

....

88

the sensor surface. Regeneration of the receptor molecule was attained by washing for 15 min with 20 mM glycine/HCl.

The enzyme carbonic anhydrase II (CAII, Sigma-Aldrich) was chosen as a target protein to detect small molecules. Sulfonamide-based inhibitors of this enzyme, such as acetazolamide, are commonly used to treat diseases such as epilepsy and glaucoma and thus represent a realistic model for drug studies with small molecules[35]. Additionally, the CAII model has extensively been used in label-free affinity studies[36,37]. Analogue to the immobilization of the IgG antibody, 0.2 mg/ml of CAII in DI-water were immobilized to an HC200m coated sensor chip via EDC/NHS chemistry and subsequently quenched by ethanolamine. Again, the analyte was directly dissolved in PBS running buffer in various concentrations, ranging from 1 nM to 1 µM. No regeneration was required as the bound complexes dissociated within a reasonable time frame. All samples for bioaffinity measurements were applied at a constant flow-rate of 50 µl/min. All subsequently presented data have been referenced with a second referencing channel.

5.4 Results

A typical injection response of a refractometric measurement can be seen in Figure 5.8, starting with water as a baseline, injection of 1 wt% glycerol in water and subsequent washing with water to reach the baseline again. Various glycerol concentrations covering five orders of magnitude, from 10 wt% to 0.001 wt% or a cover refractive index change Δn_c ranging from approximately $1.2 \times 10^{-2} - 1.2 \times 10^{-6}$ in respect to pure water, were applied to the sensor chip via the flow-cell.
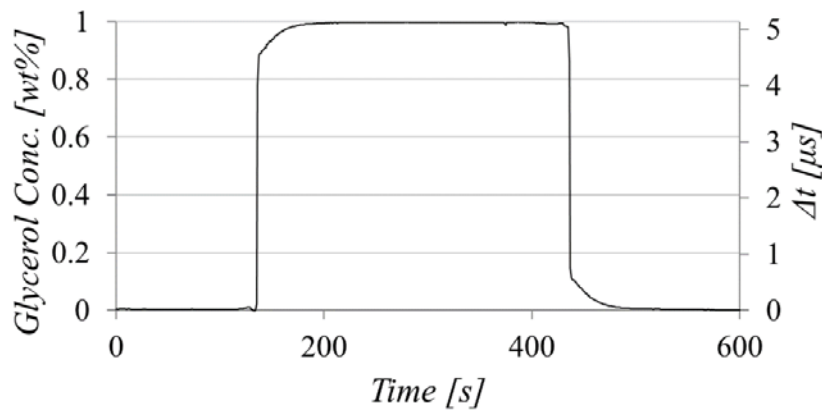

Figure 5.8: Response curve for the injection of 1 wt% glycerol in water, resulting in a signal peak shift Δt of approximately 5 µs.

Based on the collected data, the system sensitivity $\Delta t/\Delta n_{eff}$ could be deduced. The system noise was determined to $\sigma_t = 0.95$ ns (standard deviation of the signal baseline over two minutes) or $\sigma_{n,eff} = 4.2 \times 10^{-8}$ in effective refractive index units. Applying the commonly used 3-σ criterion, the LoD for effective refractive index changes Δn_{eff} is approximately 1.3×10^{-7}. The system exhibits a high degree of linearity ($R^2 = 1.00$) and repeatability, even over an extended measurement range, as can be seen in Figure 5.9. Consecutive injections of seven different glycerol concentrations between 1 wt% and 0.001 wt% (number of injections N = 12 – 34, total 148) resulted in an average effective refractive index standard deviation of only 9×10^{-7} for all samples (Figure 5.9). Additionally, the response curves reveal a very fast replacement of the investigated sample, reaching approximately 90% of the final concentration after 2 s, as depicted in Figure 5.8.
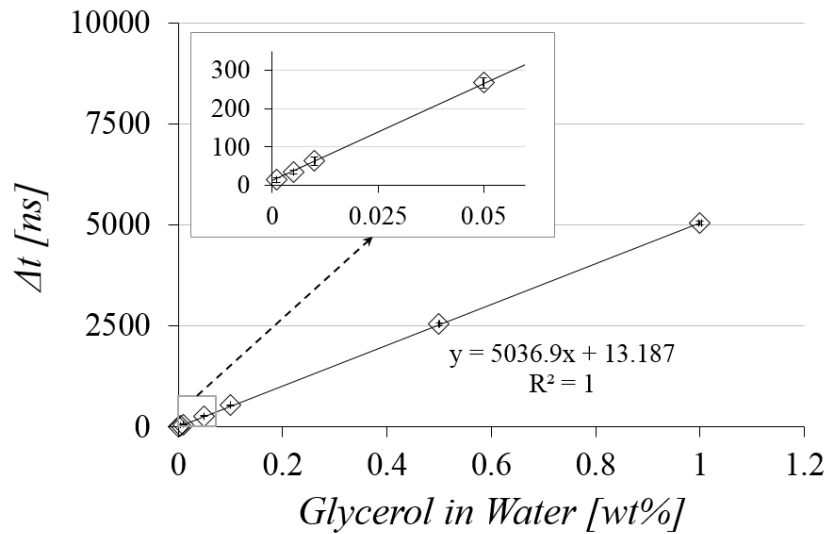
Figure 5.9: Linear plot for 148 injections of glycerol concentrations from 1 wt% and 0.001 wt% (equals a Δn_c of approximately $1.2 \times 10^{-3} - 1.2 \times 10^{-6}$) versus resulting signal shift Δt including error bars, underlining the system's linearity, repeatability and extended dynamic range.

The long-term stability of the sensor was assessed by measuring the baseline drift over a time period of 30 min and resulted in an effective refractive index drift of 7.8×10^{-8} min^{-1}, which is only slightly above the noise level. The glycerol measurements were conducted at a flow-rate of 100 µl/min and with a parallel reference channel, which is a second grating region in close proximity to the measurement grating, but with its own fluidics channel. For refractometric measurements, the reference channel was kept under a continuous flow of the running buffer (in this case water), whereas the glycerol solutions were only introduced to the measurement channel. Subtracting the reference from the measurement channel decreases drift and noise since both grating regions are interrogated by the same single MEMS mirror and laser in parallel and are, therefore, subject to the same system instabilities such as mirror or laser fluctuations, mechanical vibrations or temperature drift. In (bio)chemical sensing applications, the reference channel is mainly used to discriminate between specific and non-specific interactions.

The adsorption of 0.1 mg/ml PLL-g-PEG-biotin in 1 mM HEPES buffer to a bare Ta_2O_5 waveguide surface, performed with the OWLS instrument, resulted in surface loading of 1'875±106 pg/mm^2 and a mean signal peak shift of 21.8±2.2 µs in the ARGOS instrument, resulting in a conversion factor $\Delta t \rightarrow \Delta \mathcal{M}$ of 85.9±5 fg/(mm2·ns), which is depicted in Figure 5.10. Based on these measurements, a LoD (three times standard deviation) for surface adsorption of 0.5 pg/mm^2 could be deduced, which is a comparable LoD for best in class, waveguide based sensor systems[5,38].
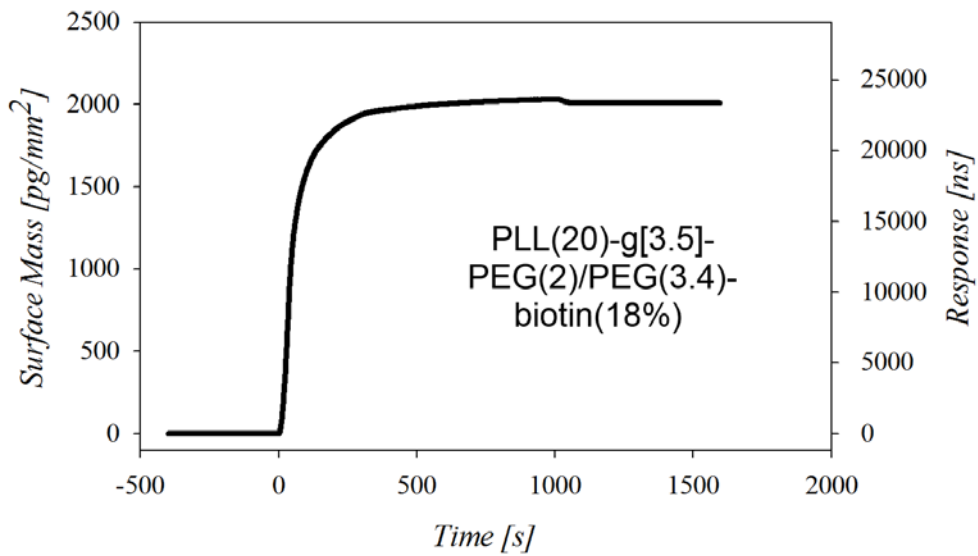

Figure 5.10: Signal response curve for the adsorption of 0.1mg/ml PLL-g-PEG-biotin in 1 mM HEPES buffer to a bare Ta_2O_5 ARGOS chip, resulting in a calibration factor to convert peak shift Δt (right y-axis) to change in surface mass density $\Delta \mathcal{M}$ (left y-axis) of 85.9±5 fg/(mm2·ns).

Various concentrations ranging from 500 pM to 5 µM of goat anti-mouse IgG were applied at a constant flow-rate to the functionalized surface, as described in Subchapter 5.3. An overlay of the sensorgrams is plotted in Figure 5.11 and the resulting dose-response curve in Figure 5.12. After the injection at t = 0 s, a distinct adsorption of the goat-anti-mouse IgG molecules to the immobilized mouse IgG receptors is evident. Around t = 900 s, the dissociation phase is initiated by flushing with the running buffer. The regeneration of the chip surface is not shown in Figure 5.11. Unfortunately, no saturation could be reached

as no higher concentrations of the analyte compound were available. The LoD was calculated conservatively according to Loock and Wentzell[39], resulting in 2.5 nM for this assay, as represented in Figure 5.15, left.
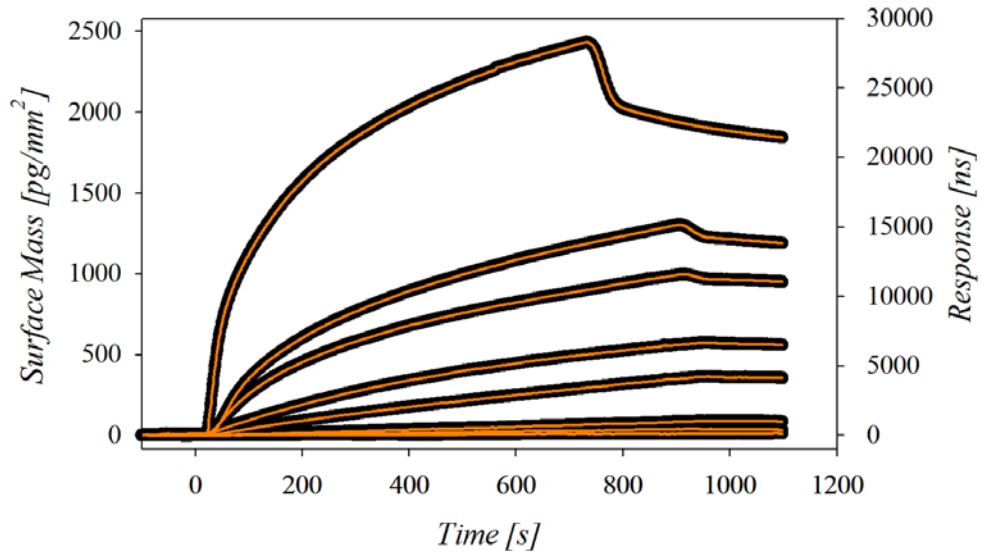

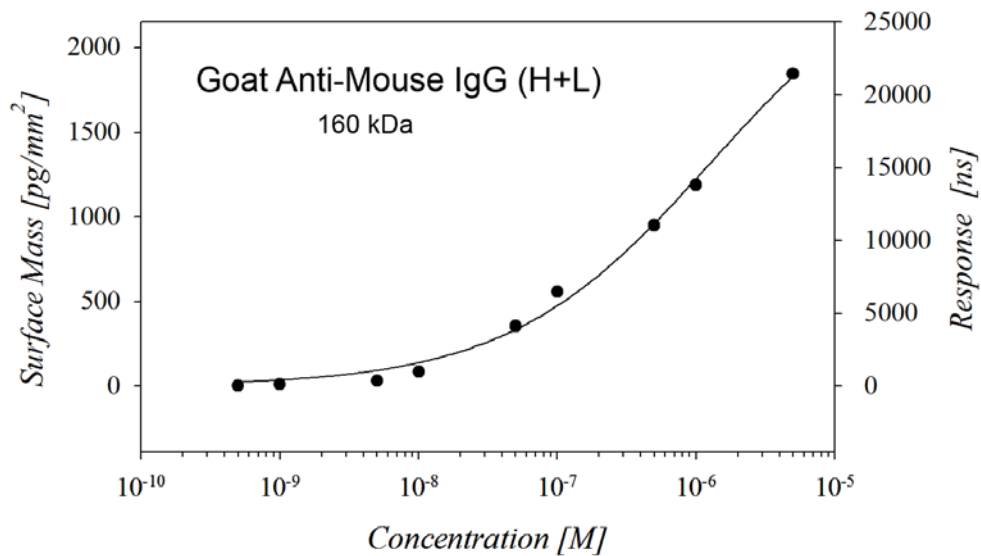**Figure 5.11:** Sensorgram overlay of goat anti-mouse IgG injections at 1, 5, 10, 50, 100, 500, 1000 and 5000 nM.

Figure 5.12: Dose response curve for goat anti-mouse IgG.

5.4 Results

....

Representative sensorgrams as well as the resulting dose-response curve for the small ligand acetazolamide, binding to its immobilized counterpart CAII, can be seen in Figure 5.13 and Figure 5.14. After a fast association phase, a steady-state equilibrium is reached for higher concentrations, resulting in a zero net binding rate. Subsequent application of the running buffer dissociated the analyte from the receptor. No regeneration buffer was required. Raw data fitting and analysis was done with Biacore's BIAevaluation™ software, followed by a 5-parameter logistic fit for the deduction of the dose-response curve. According to Loock and Wentzell[39], the LoD for acetazolamide was 40.5 nM. as plotted in Figure 5.15, right.
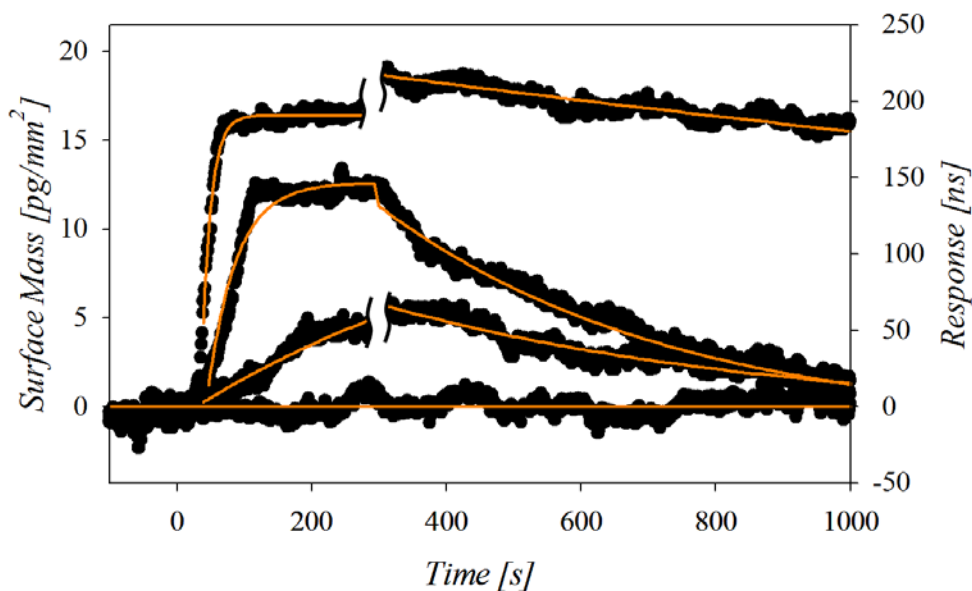

Figure 5.13: Sensorgrams for the injection of 0, 50, 500, 1000 nM acetazolamide (Dissociation phase has temporally been aligned for 50 and 1000 nM).
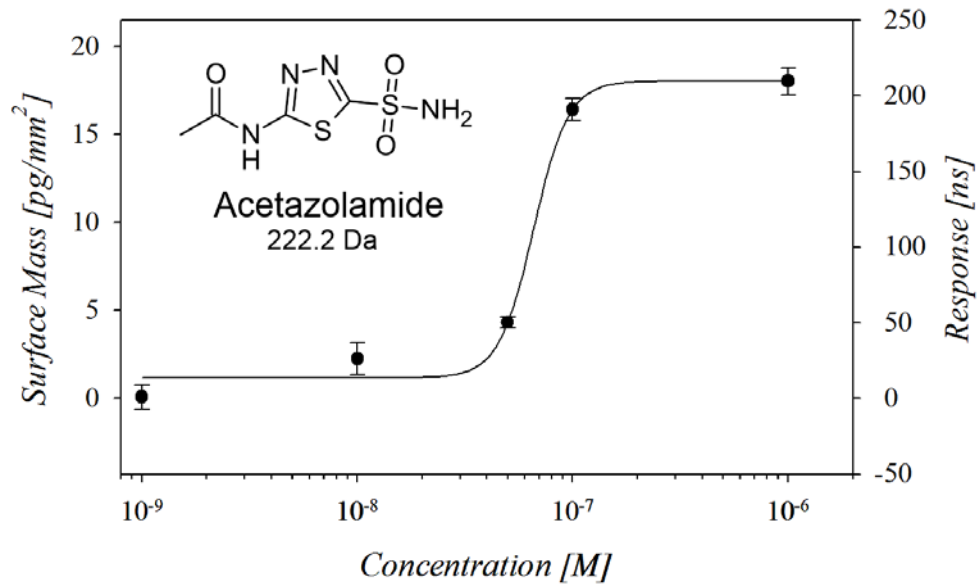
....

Figure 5.14: Dose response curve for acetazolamide.
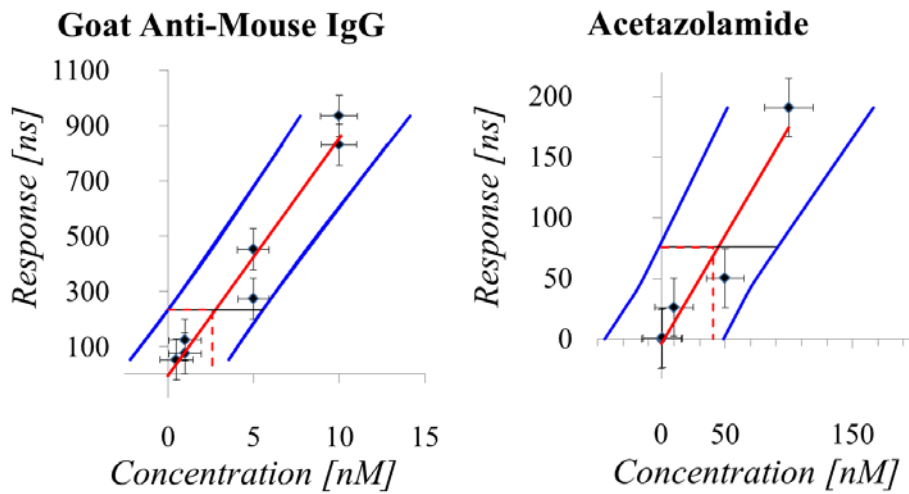

Figure 5.15: Calculation of the LoD according to Loock and Wentzell[39], resulting in 2.5 nM for goat anti-mouse IgG and 40.5 nM for acetazolamide (red: linear fit, blue: 99% confidence intervals, calculated as ±3σ, red dashed: resulting LoD).

5.5 Discussion and Conclusion

In addition to the common advantages of label-free sensors, such as the marker-free, continuous measurements, the authors are convinced that the presented ARGOS system possesses some distinct advantageous features. The high interrogation and signal acquisition rate in the kHz and MHz range, respectively, can hardly be reached by angular interrogation schemes where either the entire laser source or the sensor chip including flow-cell is tilted[9,40]. Increasing the scanning and also the acquisition rates would potentially further decrease the standard deviation of the measurement setup as more samples could be acquired at the same resolution per unit of time. On the other hand, increased scanning frequencies would lead to shorter, less pronounced resonance peaks on the detector side, which would increase amplitude noise on the latter and therefore the LoD. Replacing the light source with a more powerful laser could circumvent said problem. Nonetheless, the authors abandoned such efforts since the system's refractometric LoD was mainly limited by the fluidics and temperature controls. Other sensing schemes, such as wavelength interrogation[10,41], indeed allow for high sampling frequencies, but the vertical-cavity surface-emitting laser diodes (VCSELs) used for this purpose have a very limited wavelength tuning range of approximately 2 nm, often not sufficient to cover a required measurement dynamic range. However, by angular interrogation, the measurement range can easily be adapted and extended by simply increasing the angular oscillation amplitude of the MEMS mirror. Additionally, the tuning of the VCSELs emission wavelength is accomplished via the applied driving current, hereby also influencing the emission intensity and potentially introducing instabilities in the light source, such as cavity mode hops or polarization flips. In contrast, the laser source in the ARGOS system can be kept at constant power and wavelength. Moreover, the limited optical power of current tunable VCSEL diodes might be an issue at high interrogation frequencies or if larger sensing arrays are monitored, e.g. for multiplexed high-throughput screening, whereby the power of light available for detec-

tion is either temporally or spatially reduced. Interrogation at short wavelengths has the advantage of increased refractive index contrasts and, therefore, an overall higher sensitivity as well as an increased surface-to-bulk sensitivity ratio in particular[42] (Appendix 5.8). Since current commercially available VCSELs generally emit at wavelengths >650 nm, the full potential of the waveguide grating chip towards thin layer sensing cannot be exploited in the case of wavelength interrogation. Due to the high flexibility towards the implemented laser source in the ARGOS system, both power and wavelength ranges are vast and the appropriate light source can be chosen according to the specific application or measurement configuration.

Refractometric measurements confirmed the extended dynamic range, high linearity and sensitivity of the ARGOS system. The LoD is comparable with costly, bulky, best-in-class commercial biosensors. The advanced sample injection system allows for fast replacement and application of consecutive samples onto the sensor surface, even at low flow rates. Approximately 90% of the final concentration was reached after 2 s, compared to several minutes in case of a linear flow channel with directly adjacent liquid samples. The remaining 10% are most likely caused by dead-corners at the T-junctions.

Direct adsorption of PLL-g-PEG-biotin was used to convert and express the systems' relative units in pg/mm^2, with an approximate LoD of 0.5 pg/mm^2. The capability of the ARGOS sensor to detect large (>150 kDa) as well as small (<250 Da) molecules has been demonstrated by the direct detection of an IgG antibody and the CAII inhibitor acetazolamide. The authors are confident that the LoDs can further be decreased by systematic assay development, which was beyond the scope of this work.

The shoe-box sized ARGOS biosensor, depicted in Figure 5.5, houses the custom-made electronics to drive the system components, computational power and optoelectronics to acquire and process the data, valves and temperature controlled flow-cell for eight sensor channels. The continuously measured data can either be stored locally

on an internal solid-state memory (e.g. for long-term monitoring) or be transferred directly in real-time to an auxiliary computer. With the relatively low costs (compared to similar systems) of < 5'000 US dollars for the prototype, which can be estimated to decrease significantly in series production, its relatively compact size (172 mm x 277.5 mm x 320 mm), weight (6.6 kg) and an average power consumption of <8 W, the system is also suitable for battery powered field measurements, such as environmental monitoring or point-of-care diagnostics.

5.6   Acknowledgments

5.7 APPENDIX 5.A: Self-Referenced Waveguide Grating Biosensor[‡]

5.7.1 Introduction

Adverse effects causing signal drift or noise in label-free biosensor systems are manifold. To mention a few, variations in temperature, changes in the emission wavelength of the laser source, mechanical perturbations, e.g. through unsteady, pulsating flow of the injected liquid or external shock, influence the temporal position of the resonance peak. In addition to these physical disturbance sources, the latter can also arise from surface chemical effects such as non-specific binding. To reduce the contribution of these adverse effects, a differential measurement with at least one measurement channel and one reference channel is commonly performed[22]. Due to the spatial separation of the measurement and reference channel and their independent flow-chamber (depending on the configuration), the physical referencing is often insufficient. Self-referencing of the sensor is therefore desired and has been presented previously[43,44]. The big dynamic measurement range of the ARGOS sensing principle allows for a simple but effective self-referencing method. Partial coating and therefore locally passivating the waveguide grating area with an additional dielectric (e.g. SiO_2) or polymeric cladding layer with a refractive index n_R discriminable from the one of the measured aqueous medium n_c results in a corresponding second resonance peak ("reference peak"). Whereas adverse effects affect both resonances, changes in the cover refractive index Δn_c only result in a shift of the "measurement peak" (Figure 5.16).

[‡] The content of this Appendix has been presented at the 1st Label Free Technologies Conference, November 1-3, 2012, Amsterdam, The Netherlands. *Self-Referencing Label-Free Waveguide Grating Sensor For Remote Surveillance Of Toxins And Pollutants*. F. Kehl, P. Büchel, M. Gross, S. Follonier, J. Vörös.
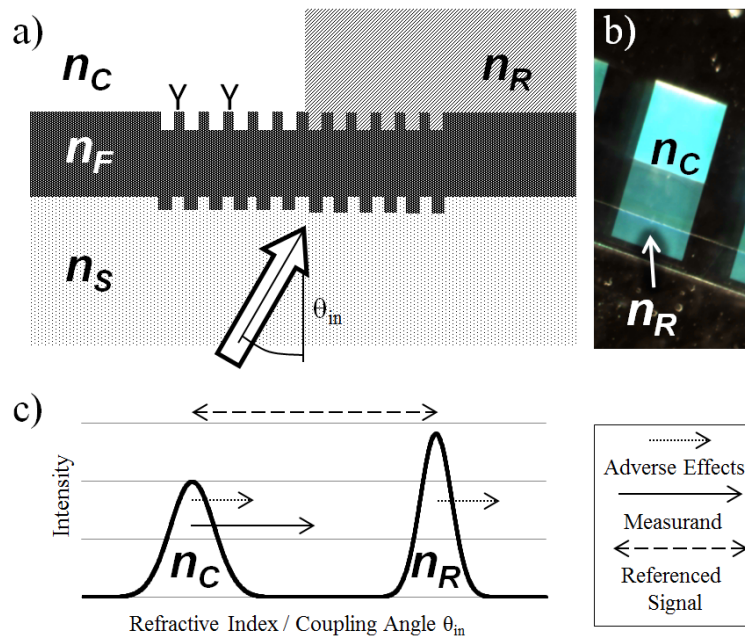
Figure 5.16: Self-referencing waveguide grating sensor by partial coating of the waveguide grating with a material exhibiting a different refractive index n_R than the aqueous cover solution n_C (schematic representation (**a**) and dark-field image (**b**)). Whereas adverse effects cause a shift in both resonance peaks, measurand induced cover refractive index changes Δn_c only affect the corresponding peak (**c**).

5.7.2   Materials and Methods

For an initial proof-of-concept, approximately 50% of the sensitive area of the waveguide grating chip was covered with an UV curable polymer (MY-132, MyPolymers, Nes Ziona, Israel; n_R = 1.32) by photolithographic means. The non-treated chip has been investigated previously regarding its coupling angle with the same optical setup as described in Chapter 4 at λ = 633nm, TM, exposing 100% of the waveguide grating surface to ambient air with a cover refractive index $n_{C,100}$ = 1. The observed single resonance peak is depicted in Figure 5.17. Partial coating of the grating area resulted in a secondary resonance peak, corresponding to the resonance angle with $n_{R,50}$ = 1.32. The uncoated region was again exposed to air with a refractive index $n_{C,50}$ = 1, therefore overlapping with the resonance peak of the unstructured chip. The peak broadening was most likely introduced by impurities on the chip surface during the structuring process.
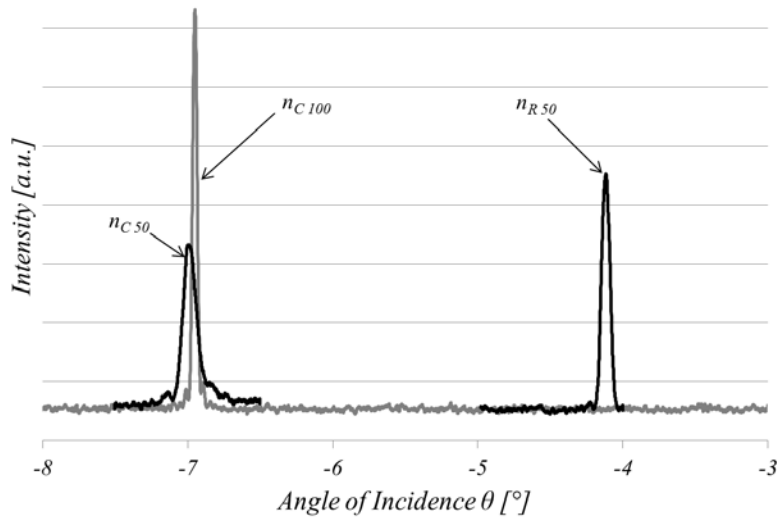
Figure 5.17: Coupling efficiencies towards angle of incidence: single resonance peak when 100% of the sensor grating is exposed to the cover medium n_C (gray). Partly covering the sensing area with a cladding material with n_R gives rise to an additional resonance peak (black).

Based on the promising results, a second batch of self-referencing waveguide grating chips was produced. Because of the low adhesion of the polymer to the chip surface and solubility in organic solvents, the cladding material was replaced by an inert, dielectric layer of SiO$_2$ ($h_{SiO2} \approx 200$ nm, $n_{SiO2} = 1.47$). The passivating SiO$_2$ layer was deposited by magnetron sputtering and structured via lift-off processing. The final, partly coated chips were mounted in the ARGOS system and the differential measurement approach was investigated towards its capability to reduce signal noise and external influences such as vibration/shock, induced temperature drift and disturbances due to sample injection.

5.7.3   Results & Discussion

The effect on the baseline noise is presented in Figure 5.18. Subtracting the normalized noise contribution of the reference peak from the measurement peak resulted in a 2.9 times smaller standard deviation compared to the non-referenced signals. High-frequency fluctuations in the range of the acquisition rate, presumably mainly caused by laser and MEMS mirror instabilities, can thus successfully be reduced.
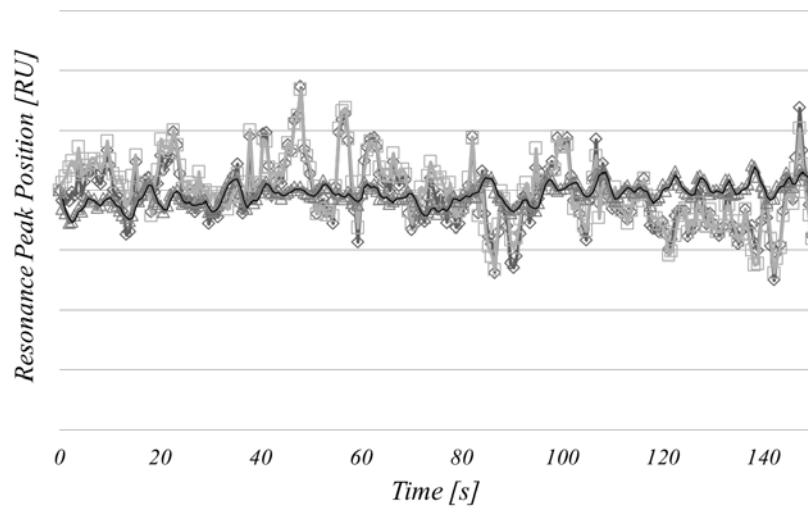
....

Figure 5.18: Normalized noise contributions of the measurement (◊) and reference (□) peak versus time, which could be reduced by a factor of 2.9 due to differential measurement (Δ).

Resistance to vibrations and mechanical shocks is a key requirement for a portable, in-situ measurement unit. The ability to compensate for mechanical perturbations was investigated by manually tapping against the sensor unit while constantly recording the baseline of an aqueous solution. As depicted in Figure 5.19, mechanical perturbations were introduced three times with increasing magnitude at $t = 50$ s, 140 s and 175 s. Whereas the first incident only caused a temporary signal shift of the acquired measurement and reference peak signals, the latter were permanently offset for the subsequent incidents. This was probably caused due to minute angular displacement of the sensor chip, laser or other optical components. Nonetheless, the differential measurement method and the resulting signal thereof successfully compensated for these adverse events.
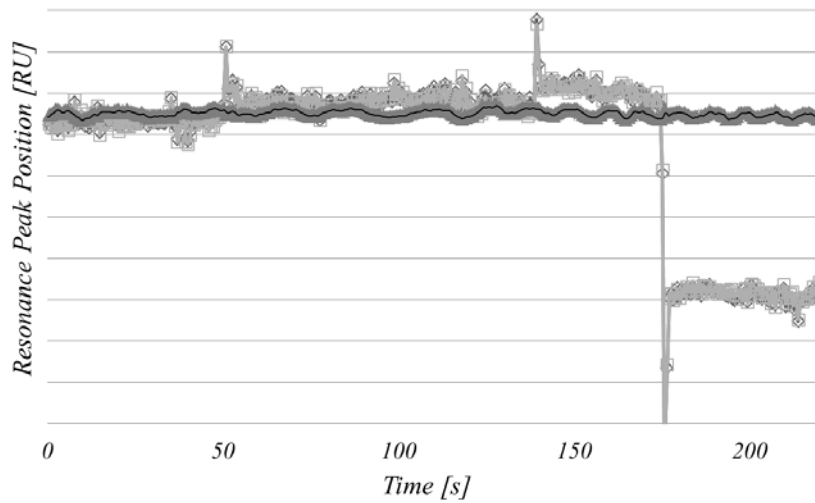
Figure 5.19: Response to mechanical perturbations at t = 50 s, 140 s and 175 s: measurement (◊), reference (□) and differential (▲) trace.

Unstable thermal conditions are a main reason for physical drift during a measurement. Advanced temperature stabilization is often power consumptive and requires a substantial thermal mass, both un-desired for portable systems. Thus, internal referencing of temperature induced drift represents an interesting feature for label-free biosensors. The robustness of the investigated, self-referencing waveguide grating coupler was qualitatively assessed by locally increasing the flow-cell temperature by means of a heat gun by a few degrees C. The sudden temperature increase led to an instant shift of the measurement and reference channel resonance peak, both settling back to their initial position after shutting down the external heat source (Figure 5.20). The differential measurement of the normalized shifts of the two peaks drastically reduces the effect of fast as well as slow temperature chang-es. However, normalization of the signal shift is a key requirement be-cause, in general, the thermo-optical coefficients $\frac{\partial n_C}{\partial T}$ and $\frac{\partial n_R}{\partial T}$ differ for the cover and reference materials.

Depending on the measurement configuration, samples can ei-ther be introduced into the fluidics chamber by constant flow or by sample injection and replacement, followed by a stagnant measure-ment phase. These sudden injections often give rise to unwanted injec-

....

tion peaks. This effect is shown in Figure 5.21 due to the injection of 1 %wt glycerol in water, followed by a second injection back to pure water. The effect arises from increased pressure in the flow channel and the mechanical load exerted on the waveguide grating chip. Since mechanical perturbation can reliably be compensated as detailed above, injection peaks can also be eliminated with the presented method, leading to a smooth transition between the exchanged samples.
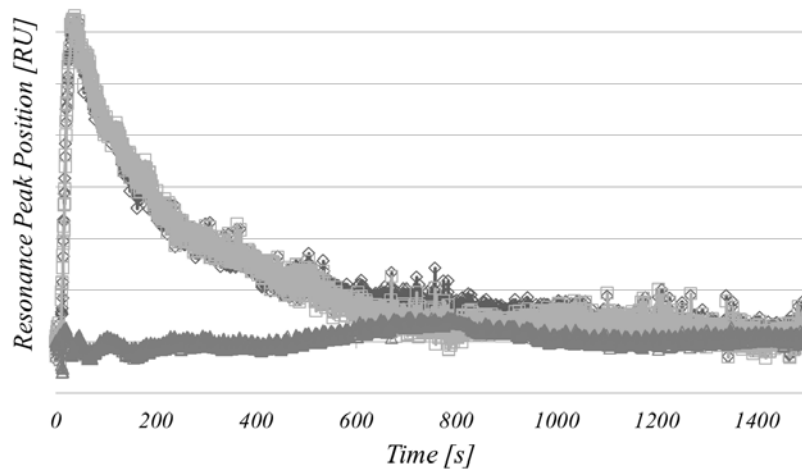
Figure 5.20: Response to thermal perturbation: measurement (◊), reference (□) and differential (Δ) trace.
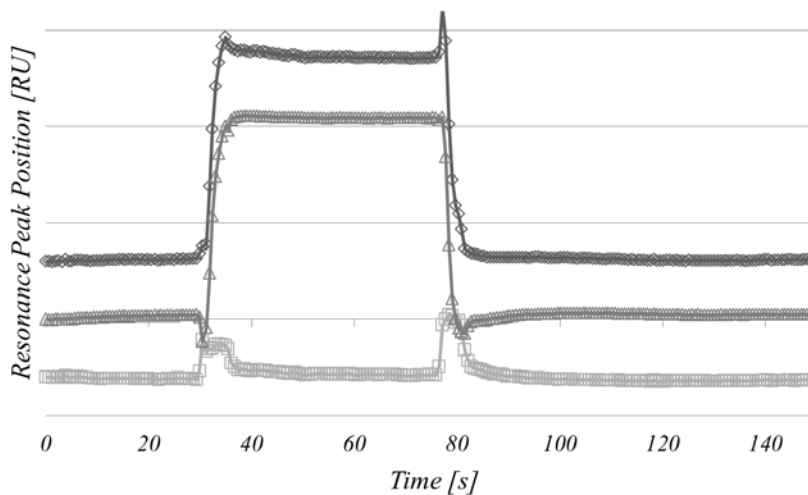
Figure 5.21: Response to injection of 1 %wt glycerol in water: measurement (◊), reference (□) and differential (Δ) trace.

....

5.7.4 Conclusion

A self-referencing waveguide grating sensor has been introduced, fabricated and qualitatively investigated towards prevalent physical perturbations. The direct proximity of the sensing and reference area within a common flow channel and the need of only one detector unit is an advantage over the conventional referencing via a second sensor element. However, the presented configuration does not allow for chemical referencing such as discrimination between specific and non-specific binding of chemical species.

5.8 APPENDIX 5.B: Enhanced Surface-to-Bulk Sensitivity Ratio by Angular Interrogation at Short Wavelengths[§]

As mentioned before, label-free, waveguide grating based biosensors are sensitive to effective refractive index changes, caused by both the adsorption of biomolecules onto the sensor surface as well as due to refractive index changes of the bulk solution[16]. As these changes can only be sensed within the penetration depth of the evanescent field of the propagating mode, the so-called surface-to-bulk sensitivity ratio (SBSR) can be optimized by changing the wavelength of the interrogating light source. Since short wavelengths lead to a shallower penetration into the bulk solution but to higher field densities in close proximity to the sensor surface, molecular binding events to the surface can be measured with enhanced sensitivity, while adverse refractive index changes of the bulk solution are suppressed[17,42]. Additionally, the higher refractive index contrast at shorter wavelengths leads to an increased sensitivity. Due to the high flexibility regarding the implemented laser source of the ARGOS system, the interrogating wavelength can be chosen in order to optimize the SBSR.
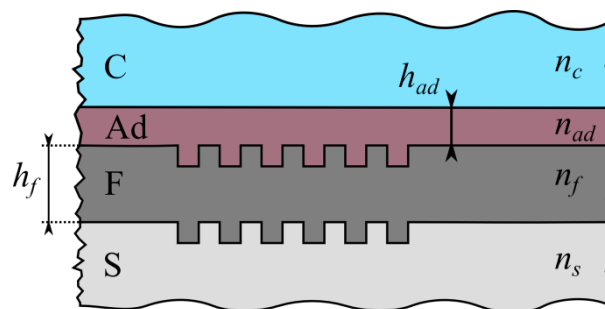

Figure 5.22: Schematic representation of a waveguide grating coupler with adsorbed adlayer with refractive index n_{ad} and thickness h_{ad}.

The angular sensitivities regarding bulk refractive index changes of the entire cover medium $\partial\theta_c/\partial n_C$ and for refractive index changes within a thin adlayer $\partial\theta_c/\partial n_{ad}$ was simulated for three different wavelengths (λ = 532 nm, 633 nm, 780 nm; TM mode). As detailed in Figure 5.23, the angular bulk refractive sensitivity is largest for λ = 780 nm for the investigated wavelengths, caused by the increased penetration depth of the evanescent wave compared to the two shorter wavelengths. The slightly higher bulk refractive sensitivity of interrogation at λ = 532 nm over 633 nm can be explained by the increased refractive index difference between waveguide and cover medium for shorter wavelengths.

Figure 5.23: Simulated angular bulk refractive index sensitivity $\partial\theta_c/\partial n_C$ versus waveguide thickness h_f for λ = 532 nm, 633 nm and 780 nm.

Thin layer sensing was simulated by assuming the adsorption of an adlayer with a thickness h_{ad} = 20 nm and differentiating its refractive index n_{ad}, but keeping the overlying cover refractive index n_c constant. The increased angular surface sensitivity for λ = 532 compared to longer wavelengths is evident in Figure 5.24.
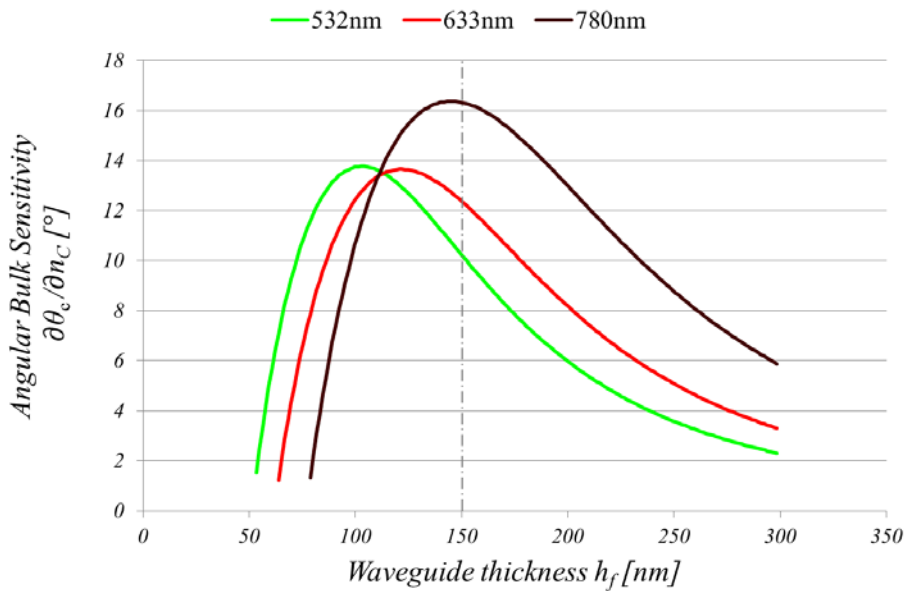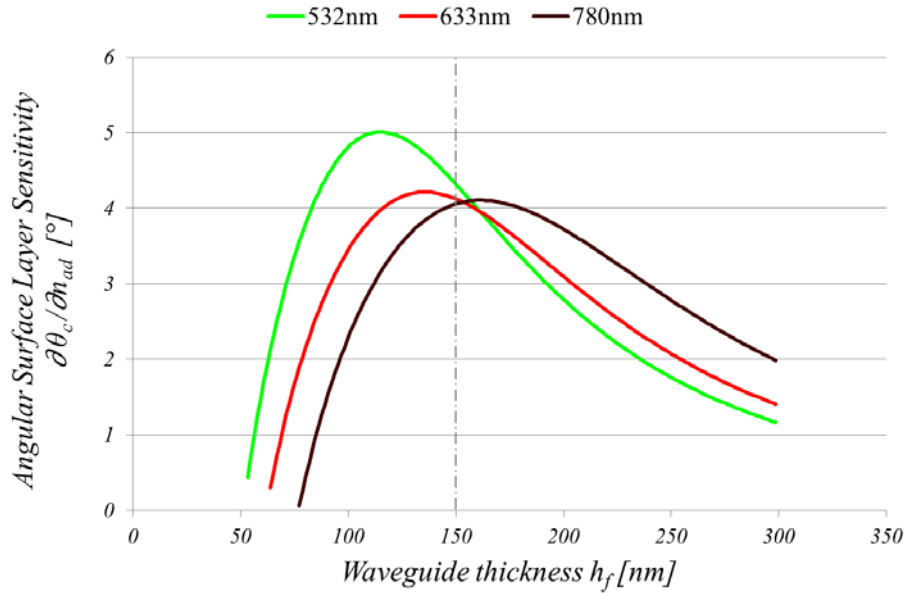
Figure 5.24: Simulated angular surface layer refractive index sensitivity $\partial\theta_c/\partial n_{ad}$ versus waveguide thickness h_f for λ = 532 nm, 633 nm and 780 nm.

Since, in general, the two effects take place simultaneously and hence, also for thin layer sensing, bulk effects beyond the adlayer exert an adverse effect on the measurement. As refractometric changes in the cover refractive index can be regarded as background noise and drift sources for thin layer sensing, it is hence desired to optimize the SBSR = $\frac{\partial\theta_c}{\partial n_{ad}} \Big/ \frac{\partial\theta_c}{\partial n_C}$.

To experimentally investigate the simulations, the coupling angle shift $\Delta\theta$ upon the change of the cover refractive index n_C (water to 10 %wt glycerol in water) and upon the adsorption of a protein layer (10 % fetal bovine serum (FBS) in PBS, Sigma-Aldrich, USA) for the aforementioned waveguide grating coupler (h_f = 150 nm, dashed lines in Figure 5.23 and Figure 5.24) was measured for the three said wavelengths. In agreement with the simulations, the measured shift induced by the cover refractive index change decreased for shorter wavelengths (Figure 5.25, left), whereas the shift due to the absorption of a protein layer was similar for all investigated wavelengths at the given waveguide layer thickness h_f (Figure 5.25, middle). Thus, it is concluded that short wavelengths exhibit an increased SBSR (Figure 5.25, right).
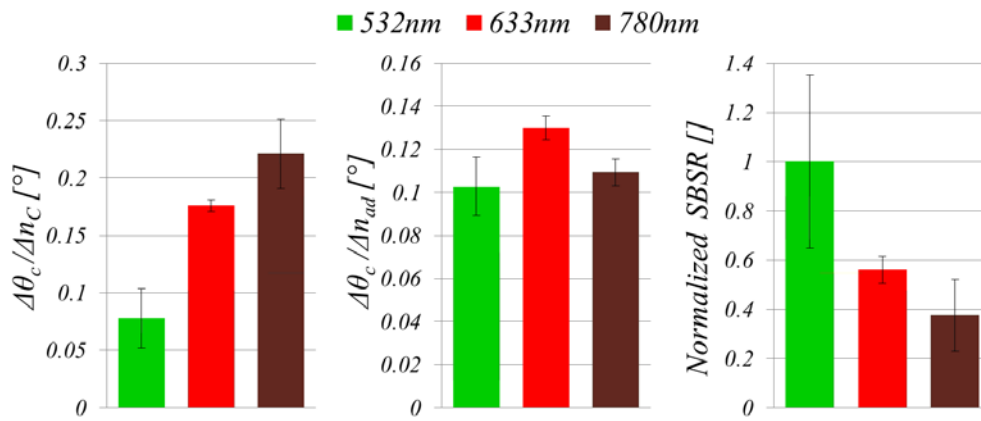
Figure 5.25: Measured bulk (**left**) and surface layer refractive index sensitives (**center**) with normalized SBSR (**right**) for λ = 532 nm, 633 nm and 780 nm.

5.9   APPENDIX 5.C: Technical Details of the ARGOS System

The ARGOS system can be divided into five functional subunits, namely the system's mechanical structure, optics unit, electronics suite, fluidics and thermal management. A mechanical drawing of the system and its components is detailed in Figure 5.26, highlighting the individual subunits in different colors. The respective constituents will be explained in more detail in the following sections.

5.9.1   Mechanical Design

The custom-made mechanical structure acts as both housing and structural support for the individual system components. The latter are fixed on a sturdy aluminum ground plate and covered by a demountable casing. The casing possesses two openings for the insertion and docking of the sensor chip in the measurement bay as well as oblong vents, serving as inlets for cooling air. The electrical, as well as fluidics connections, are mounted on two side panels attached to the ground plate, hereby allowing the removal of the cover casing without disconnection of cables or tubings. All critical mechanical components are black anodized to reduce stray light within the optical compartment. The outer dimensions of the ARGOS sensor measure 172 mm x 277.5 mm x 320 mm, with a total weight of 6.6 kg.

Figure 5.26: Mechanical drawing of the ARGOS sensor system (top and side view), highlighting the individual system constituents: optics module (red), fluidics (blue), electronics (green), thermal management (purple) and mechanical structure (gray).

5.9 APPENDIX 5.C

....

5.9.2 Optics

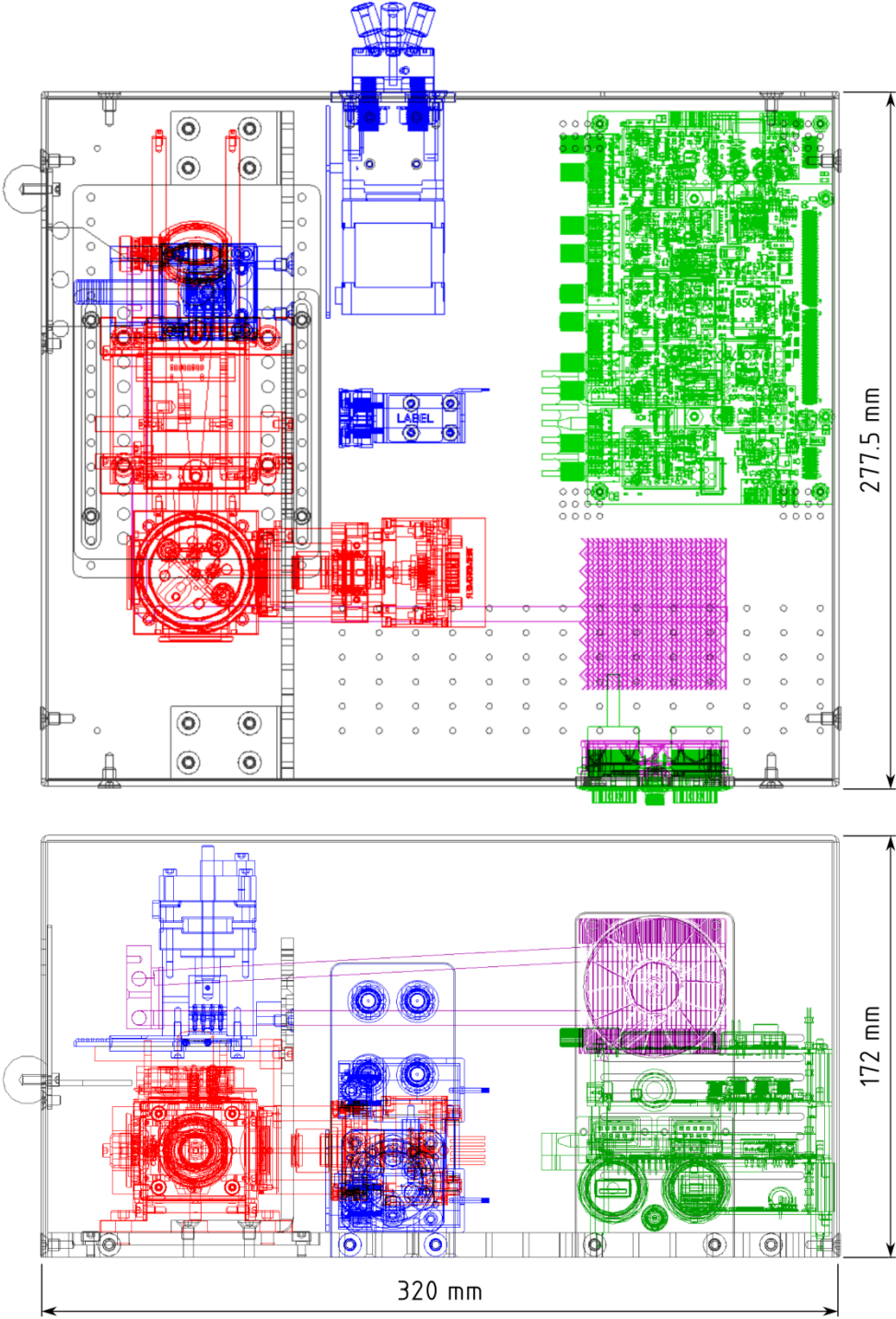The interrogating optical module consists of off-the-shelf, commercially available components from Thorlabs, Inc. (Newton, NJ, USA) and is illustrated in Figure 5.27.
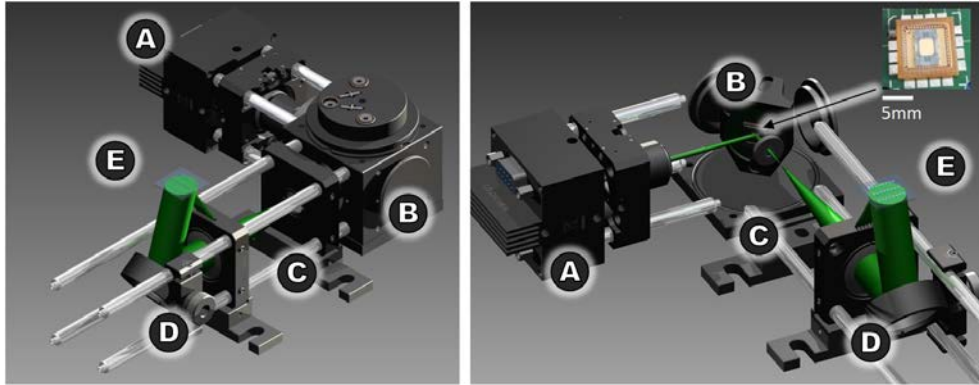
Figure 5.27: Optical module consisting of laser mount (**A**), kinematic MEMS mirror mount (**B**), Keplerian beam expander (**C**), pivoting mirror (**D**) and sensor chip (**E**).

A diode-pumped solid state (DPSS) laser (DJ532-10) including collimation and beam shaping optics is mounted in a temperature stabilized housing (LDM21) and its beam is directly impinging the scanning MEMS mirror under an angle of 45 degrees. The MEMS mirror is mounted within a C6W 30mm cage cube on a kinematic B4C/M platform for alignment purposes. Both laser current and temperature, as well as the scanning of the MEMS mirror, are driven by custom electronics (not depicted), which are described in the subsequent section. Upon deflection, the beam enters a Keplerian beam expander (4f-optics consisting of two plano-convex spherical N–BK7 lenses with F_1 = 10 mm (LA1116-A) and F_2 = 75 mm (LA1608-A), Figure 5.28), thereby expanding the previously 2.5 mm wide beam with width w_{in} by a factor of F_2/F_1 = 7.5 to w_{out} to simultaneously illuminate all eight measurement and reference pads on one chip. While expanding the beam 7.5 times, the angle of deflection decreases by the inverse ratio of the outgoing beam. Since the mirror performs more stable at increased deflection amplitudes, the latter can be operated at angles 7.5 times bigger than actually required for the waveguide grating interrogation (approximately 15° resulting in 2° scan range on the chip), thus also decreasing an-

....

112

gular deviations, e.g. due to vibrations, by the same factor. Before ultimately reaching the sensor chip at a distance F_2 from the second plano-convex lens, the beam is deflected by a pivoting mirror to impinge the sensor chip under the resonance angle θ_c. The out-coupled beams are picked up by eight individual optical fibers and led to the optoelectronic signal amplifiers (not depicted).
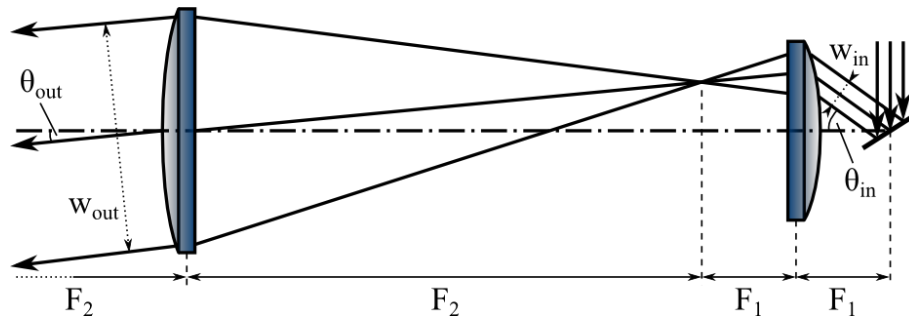
Figure 5.28: Keplerian beam expander: A collimated beam with width w_{in} gets deflected by the (scanning) MEMS mirror (**right**) and enters the beam expander through a first plano-convex lens with a focal length F_1 under an angle θ_{in}. A second plano-convex lens with a focal length F_2 expands the beam width to $w_{out} = F_2/F_1 \cdot w_{in}$. The re-collimated beam impinges the sample at a distance F_2 from the latter lens under an angle $\theta_{out} = F_1/F_2 \cdot \theta_{in}$.

5.9.3   Electronics Suite

The instrument's electronics is responsible for controlling all system subunits, acquiring, processing and storing the measurement data and allows direct communication with the operator via a software-based user interface. In the presented system, the electronics is composed of four stackable circuit boards (Figure 5.29), which will be described in more detail below.

5.9.3.1 CPU Board

The central processing unit (CPU) board houses the computational power (ATMEL AT32UC3C0512, 32-bit, 66 MHz, 512 kB Flash/64 kB RAM)) and essential auxiliary components such as non-volatile memory (FRAM and microSD card), real time clock, reference voltage, USB interface and data flash (8 MB). The CPU board controls all three ancillary circuit boards, establishes the bidirectional communication to

the user interface and either locally saves or transmits the acquired data to an external computer.
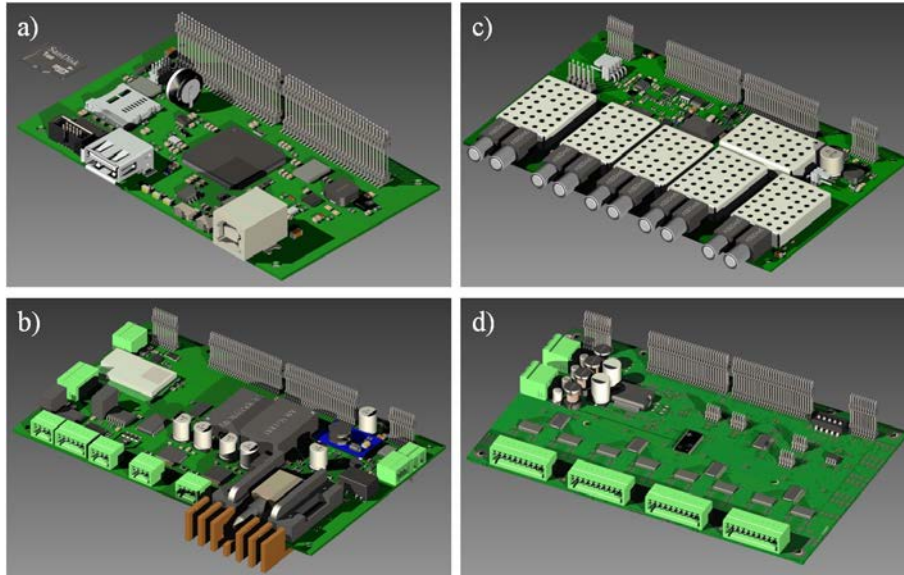
Figure 5.29: System electronics: (**a**) CPU board, (**b**) basis board, (**c**) analogue board, (**d**) digital board.

5.9.3.2 Basis Board

Keeping the laser at constant power or current (CP and CC options available), controlling stepper motors (e.g. for the automated docking of the sensor chip), establishing the RS-232 serial connection for debugging purposes and accessing external devices such as pumps or selector valves, are tasks accomplished by the basis board. Additionally, temperature and humidity sensors are monitoring potential overheating or leakages in the fluidic system. Depending on the implemented laser source, optionally a fiber coupled 14-pin butterfly laser diode with internal temperature control (±0.005°C) and feedback photodiode for CP mode can be mounted on the corresponding socket.

5.9.3.3 Analogue Board

The eight out-coupled signals from the sensor chip are guided separately via optical fibers to the photodiodes on the analogue board and subsequently fed into individual pre-amplifiers. The signal amplitudes are quantified by an analogue-digital-converter (ADC), automatically adjusted by programmable gain amplifiers and the temporal peak

positions are analyzed in parallel by a field programmable gate array (FPGA, Altera EP4CE6F17C6) at 400 MHz. The resulting, measured time shift is then transferred to the CPU board and eventually plotted in the sensorgram. A fast, CPU internal analogue-digital-converter (1 MS/s, 16-bit) allows individual sampling of the resonance peaks to verify the merit of the acquired signal. Additionally, the analogue board houses the driving electronics (90V DC/DC buck-boost converter) for the MEMS mirror actuation.

5.9.3.4 Digital Board

The digital board possesses 16 programmable digital inputs/outputs (DIOs) to drive the internal T-valves, status LEDs and optionally also internal motors/pumps via pulse-width-modulation (PWM). Two independent 25 W temperature controllers thermally stabilize the laser as well as the fluidics chamber.

5.9.4 Fluidics

The working principle of the fluidics system is schematically described in more detail in Subchapter 5.3. In the current system, the liquid is introduced by external pumps, such as peristaltic or syringe pumps into one inlet for the measurement and the reference channel respectively. The effluents of the two channels can be collected in a waste container at the two fluidic outlets. The waveguide grating sensor chip is mounted on a black polyoxymethylene copolymer (POM-C) holder, which can be inserted into the measurement system and the temperature stabilized chip bay through an opening in the cover casing. A linear motor subsequently presses a gimbaled piston with the surface mounted, laser ablated microfluidic EPDM gasket onto the sensor chip, thereby forming the fluidic channels (Figure 5.30).
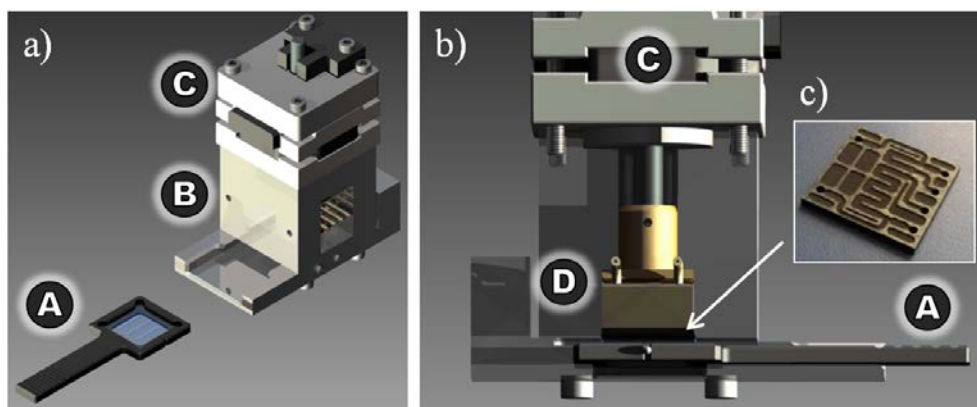
Figure 5.30: System fluidics: **a**) mounted chip (**A**) to be manually inserted into chip bay (**B**). **b**) Cross section of chip bay with linear motor (**C**) pressing piston (**D**) on chip surface. **c**) Laser ablated EPDM gasket.

Four optical, non-invasive bubble detectors notice air separating the injected liquids at the in- and outlet of the two channels, triggering the two downstream, bi-stable T-valves (WLB-3-1/4U5-1, Takasago Electric, Inc., Japan) to allow for automated sample injection. For automated sample loading, an optional selector valve can be implemented additionally within the ARGOS (e.g. C62-3186I, Vici AG, Switzerland).

5.9.5 Graphical User Interface (GUI)

All vital and low-level system commands are directly implemented in the microcontroller and FPGA. Therefore, the system can be operated autonomously without the necessity of an external computer. Data acquisition and processing is directly accomplished by the dedicated, internal electronics and only the final results as well as system commands are transferred from and to the LabView (National Instruments, USA) based GUI, keeping traffic and external computational power at a minimum.
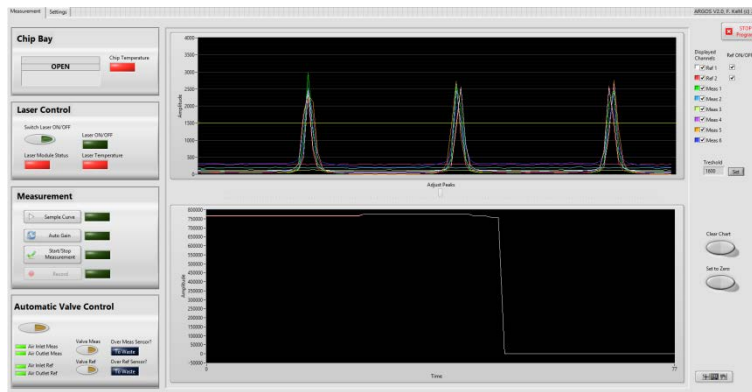
Figure 5.31: LabView based end user GUI with detector signal in upper and sensorgram in lower graph.
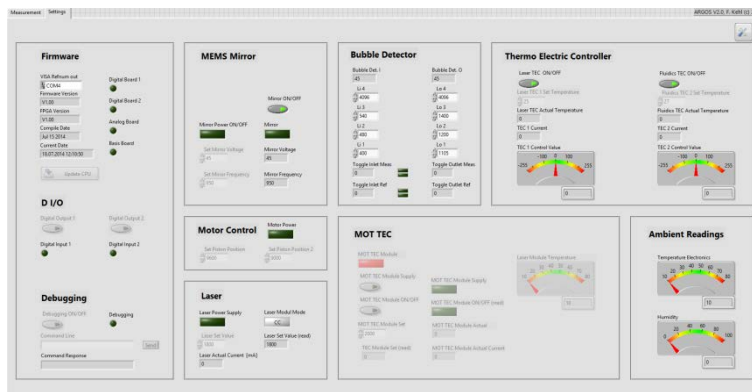
Figure 5.32: Settings tab to read and control system parameters.

....

5.10 References

1. Cooper, M. Label-free biosensors: techniques and applications. *Cambridge University Press* (2009).

2. Cooper, M. a. Optical biosensors in drug discovery. *Nat. Rev. Drug Discov.* **1,** 515–528 (2002).

3. Adrian, J. *et al.* Waveguide interrogated optical immunosensor (WIOS) for detection of sulfonamide antibiotics in milk. *Biosens. Bioelectron.* **24,** 3340–3346 (2009).

4. Piehler, J., Brandenburg, A., Brecht, A., Wagner, E. & Gauglitz, G. Characterization of grating couplers for affinity-based pesticide sensing. *Appl. Opt.* **36,** 6554–6562 (1997).

5. Kozma, P., Kehl, F., Ehrentreich-Förster, E., Stamm, C. & Bier, F. F. Integrated planar optical waveguide interferometer biosensors: A comparative review. *Biosensors and Bioelectronics* **58,** 287–307 (2014).

6. Ciminelli, C., Campanella, C. E. C. M., Dell'Olio, F., Campanella, C. E. C. M. & Armenise, M. N. Label-free optical resonant sensors for biochemical applications. *Prog. Quantum Electron.* **37,** 51–107 (2013).

7. Nellen, P. M., Tiefenthaler, K. & Lukosz, W. Integrated optical input grating couplers as biochemical sensors. *Sensors and Actuators* **15,** 285–295 (1988).

8. Clerc, D. & Lukosz, W. Integrated optical output grating coupler as refractometer and (bio-) chemical sensor. *Sensors Actuators B Chem.* **11,** 461–465 (1993).

9. Vörös, J. *et al.* Optical grating coupler biosensors. *Biomaterials* **23,** 3699–3710 (2002).

10. Wiki, M. & Kunz, R. E. Wavelength-interrogated optical sensor for biochemical applications. *Opt. Lett.* **25,** 463–465 (2000).

11. Fattinger, C. The bidiffractive grating coupler. *Appl. Phys. Lett.* **62,** 1460–1462 (1993).

12. Tamir, T. & Peng, S. T. Analysis and design of grating couplers. *Appl.*

....

Phys. A Mater. Sci. **254,** 235–254 (1977).

13.   Tiefenthaler, K. & Lukosz, W. Grating couplers as integrated optical humidity and gas sensors☆. *Thin Solid Films* **126,** 205–211 (1985).

14.   Kunz, R. E. Grating couplers in tapered waveguides for integrated optical sensing. *Proc. SPIE* **2068,** 313–325 (1994).

15.   Gartmann, T. E. & Kehl, F. Experimental Validation of the Sensitivity of Waveguide Grating Based Refractometric (Bio)sensors. *Biosensors* **5,** 187–198 (2015).

16.   Tiefenthaler, K. & Lukosz, W. Sensitivity of grating couplers as integrated-optical chemical sensors. *Journal of the Optical Society of America B* **6,** 209 (1989).

17.   Kunz, R. E. & Cottier, K. Optimizing integrated optical chips for label-free (bio-)chemical sensing. *Anal. Bioanal. Chem.* **384,** 180–90 (2006).

18.   Guillod, T., Kehl, F. & Hafner, C. C. FEM-based Method For The Simulation Of Dielectric Waveguide Grating Biosensors. *Prog. Electromagn. Res.* **137,** 565–583 (2013).

19.   Cottier, K., Kunz, R. E., Voirin, G. & Wiki, M. Thickness-modulated waveguides for integrated optical sensing. in *International Symposium on Biomedical Optics* (ed. Gannot, I.) 53–63 (International Society for Optics and Photonics, 2002).

20.   Hawkes, J. B. & Astheimer, R. W. The temperature coefficient of the refractive index of water. *J. Opt. Soc. Am.* **38,** 804–6 (1948).

21.   Chu, a. K., Lin, H. C. & Cheng, W. H. Temperature dependence of refractive index of Ta2O5 Dielectric Films. *J. Electron. Mater.* **26,** 889–892 (1997).

22.   Dübendorfer, J. & Kunz, R. E. Reference pads for miniature integrated optical sensors. *Sensors Actuators B Chem.* **38,** 116–121 (1997).

23.   Taylor, G. Dispersion of Soluble Matter in Solvent Flowing Slowly through a Tube. *Proc. R. Soc. A Math. Phys. Eng. Sci.* **219,** 186–203 (1953).

24.   Aris, R. On the Dispersion of a Solute in a Fluid Flowing through a Tube. *Proc. R. Soc. A Math. Phys. Eng. Sci.* **235,** 67–77 (1956).

5.10 References

25. Bae, A. J., Beta, C. & Bodenschatz, E. Rapid switching of chemical signals in microfluidic devices. *Lab Chip* **9,** 3059–3065 (2009).

26. Kuhn, K. Evaluation of a planar optic waveguide as a platform for evanescent field chemical sensor development. 521–600 (1993).

27. Birkhoff, R. D., Painter, L. R. & Heller, J. M. Optical and dielectric functions of liquid glycerol from gas photoionization measurements. *J. Chem. Phys.* **69,** 4185 (1978).

28. Kedenburg, S., Vieweg, M., Gissibl, T. & Giessen, H. Linear refractive index and absorption measurements of nonlinear optical liquids in the visible and near-infrared spectral region. *Opt. Mater. Express* **2,** 1588 (2012).

29. Hoyt, L. F. New Table of the Refractive Index of Pure Glycerol at 20°C. *Ind. Eng. Chem.* **26,** 329–332 (1934).

30. Huang, N., Michel, R., Voros, J. & Textor, M. Poly (L-lysine)-g-poly (ethylene glycol) layers on metal oxide surfaces: surface-analytical characterization and resistance to serum and fibrinogen adsorption. *Langmuir* **17(2)**, 489-498 (2001).

31. Huang, N. P., Vörös, J., De Paul, S. M., Textor, M. & Spencer, N. D. Biotin-derivatized poly(L-lysine)-g-poly(ethylene glycol): A novel polymeric interface for bioaffinity sensing. *Langmuir* **18,** 220–230 (2002).

32. Kenausis, G. L. *et al.* Poly(l -lysine)- g -Poly(ethylene glycol) Layers on Metal Oxide Surfaces: Attachment Mechanism and Effects of Polymer Architecture on Resistance to Protein Adsorption †. *J. Phys. Chem. B* **104,** 3298–3309 (2000).

33. Kurrat, R., Textor, M., Ramsden, J. J., Böni, P. & Spencer, N. D. Instrumental improvements in optical waveguide light mode spectroscopy for the study of biomolecule adsorption. *Rev. Sci. Instrum.* **68,** 2172–2176 (1997).

34. Johnsson, B., Löfås, S. & Lindquist, G. Immobilization of proteins to a carboxymethyldextran-modified gold surface for biospecific interaction analysis in surface plasmon resonance sensors. *Anal. Biochem.* **198,** 268–277 (1991).

35. Supuran, C. T. Carbonic anhydrases: novel therapeutic applications for inhibitors and activators. *Nat. Rev. Drug Discov.* **7**, 168–181 (2008).

36. Myszka, D. G. Analysis of small-molecule interactions using Biacore S51 technology. *Anal. Biochem.* **329**, 316–23 (2004).

37. Papalia, G. a *et al.* Comparative analysis of 10 small molecules binding to carbonic anhydrase II by different investigators using Biacore technology. *Anal. Biochem.* **359**, 94–105 (2006).

38. Fan, X. *et al.* Sensitive optical biosensors for unlabeled targets: A review. *Anal. Chim. Acta* **620**, 8–26 (2008).

39. Loock, H.-P. & Wentzell, P. D. Detection limits of chemical sensors: Applications and misapplications. *Sensors and Actuators B: Chemical* **173**, 157–163 (2012).

40. Kunz, R. & Dübendorfer, J. Novel miniature integrated optical goniometers. *Sensors and Actuators A: Physical* **60**, 23–28 (1997).

41. Cottier, K., Wiki, M., Voirin, G., Gao, H. & Kunz, R. E. Label-free highly sensitive detection of (small) molecules by wavelength interrogation of integrated optical chips. *Sensors and Actuators B-chemical* **91**, 241–251 (2003).

42. Ganesh, N., Block, I. D. & Cunningham, B. T. Near ultraviolet-wavelength photonic-crystal biosensor with enhanced surface-to-bulk sensitivity ratio. *Appl. Phys. Lett.* **89**, 023901 (2006).

43. Yuen, P. K. *et al.* Self-referencing a single waveguide grating sensor in a micron-sized deep flow chamber for label-free biomolecular binding assays. *Lab Chip* **5**, 959–965 (2005).

44. Krol, M. Self-referencing waveguide grating sensors. *US Pat. 7,203,386* (2007).

5.10 References

6 Design of a Label-Free, Distributed Bragg Grating Resonator Based Dielectric Waveguide Biosensor [††]

6.1 Abstract

In this work, we present a resonant, dielectric waveguide device based on distributed Bragg gratings for label-free biosensing applications. The refractive index sensitive optical transducer aims at improving the performance of planar waveguide grating sensor systems with limited Q-factor and dynamic range by combing the advantages of resonant cavities, such as a multitude of resonance peaks with high finesse, with the manageable complexity of waveguide grating couplers. The general sensor concept is introduced and supported by theoretical considerations as well as numerical simulations based on Coupled Mode Theory. In contrast to a single Bragg grating reflector, the presented Fabry-Pérot type distributed Bragg resonator exhibits an extended measurement range as well as relaxed fabrication tolerances. The resulting, relatively simple sensor structure can be fabricated with standard lithographic means and is independent of expensive light-sources and/or detectors, making an affordable but sensitive device, potentially suitable for point-of-care applications.

6.2 Introduction

Biosensors are widely used in various fields such as pharmaceutical industry, healthcare, biotechnology, food, feed and environmental monitoring to detect the interaction, presence and concentration of (bio)molecules and exist in numerous configurations. Dielectric waveguide based sensors represent a subgroup of highly sensitive optical transducer elements, mainly applied for label-free biosensing[1–4]. Compared to labelled methods, such as fluorescent based sensing methods, in label-free detection the molecules do not have to be functionalized with a marker element, which is a benefit since the functionalization with fluorescent labels can be expensive, laborious and can alter the structure and hence the molecules' characteristics. Yet still, in general, label-free methods are less sensitive than labelled ones[5].

To overcome this disadvantage, many promising and highly sensitive interferometers as well as resonator based integrated optical transducers have been presented to increase the sensitivity and lower the limit of detection of label-free devices. Countless examples can be found in Refs. 6–10. Sophisticated micro-sphere, disc and ring resonator sensors with low limit of detection (LoD) and high quality factors (Q-factor) have been realized but seem not to be suitable for volume production due to their high level of complexity regarding fabrication and light coupling. In contrast, grating based waveguide sensors can be batch produced by standard lithographic means and light can easily be coupled via the diffractive grating itself, but exhibit lower Q-factors and, therefore, higher LoD[11]. In this work, we introduce a distributed Bragg grating resonator waveguide biosensor, combining the simplicity of grating couplers with a high finesse and extended dynamic range of resonant cavities. Compared to fiber Bragg gratings (FBG), the presented planar structure can be fabricated as well as read-out in parallel at a higher integration density, important drivers regarding price and multiplexing.

6.2.1 Background and Motivation

In its simplest configuration, a planar waveguide sensor has a three-layer structure with a high refractive index film F between the optically less dense supporting substrate S and the investigated cover medium C. The high refractive dielectric waveguide film acts as a conduit of the propagating light by means of total internal reflection. Light will be guided if the propagating mode fulfils the following condition[12]:

$$2kh_f\sqrt{n_f^2 - n_{eff}^2} + \varphi_{fc} + \varphi_{fs} = 2\pi m_{wg} \tag{6.1}$$

where $k = 2\pi/\lambda$ is the wavenumber, λ the wavelength of the propagating light, h_f and n_f the waveguide film height and refractive index, respectively, the effective refractive index n_{eff}, which is defined as $n_{eff} = c/v_p$ with v_p denoting the phase velocity of the guided mode and c the vacuum speed of light, φ_{fc} and φ_{fs} the Fresnel reflection phase shifts at the film-cover and film-substrate interface, respectively, and the waveguide mode number m_{wg}. Depending on the waveguide configuration, only a discrete number of guided modes $m_{wg} = 0,1,2,...$ is supported within the structure. For single-mode waveguides, the right-hand side of Equation (6.1) reduces to zero. As the Fresnel reflections phase shifts φ_{fc} and φ_{fs} differ for transverse electric (TE) and transverse magnetic (TM) waves, n_{eff} is polarization dependent and is directly proportional to the propagation constant of the guided mode. Due to the mode overlap (evanescent field) of the propagating light into the cover and substrate in close proximity to the waveguide interface, any refractive index change at the sensor surface alters the phase velocity of the guided mode and therefore n_{eff}, which can be detected by optical transducers as described below.

In the case of a waveguide grating coupler, a periodically corrugated grating region in the waveguide can be used as a light coupling region, for both in and out-coupling from the waveguide (Figure 6.1). This coupling region is very sensitive to refractive index changes and is often used as a sensor[13]. Changes in the cover refractive index n_c in close proximity to the sensor surface, e.g., by the adsorption of

....

(bio)molecules with unequal refractive index than the displaced aqueous medium, alter the effective refractive index n_{eff}. Since the coupling condition is defined as

$$n_{c/s} \cdot \sin(\theta_c) = n_{eff} - \frac{m_g \lambda}{\Lambda} \qquad (6.2)$$

with the grating period Λ, grating diffraction order m_g and $n_{c/s}$ the refractive indices of the cover or substrate, respectively, depending on which side of the waveguide is considered, any changes in n_{eff} can be monitored by changes in the coupling angle $\Delta\theta_c$ or a wavelength shift $\Delta\lambda_{shift}$ [13]. Various interrogation schemes for waveguide grating sensors have been reported based on angular as well as spectral detuning.

While Equation (6.2) holds true for infinitely extended and shallow gratings illuminated by a perfect plane wave, actual sensors with finite grating depth and length exhibit broadened resonances and, therefore, a limited Q-factor[14,15]. For these finite structures, an effective grating length L_{eff} can be defined, which is inversely proportional to the spectral broadening $\delta\lambda_{FWHM}^{CG}$ of the resonance peak of waveguide grating couplers[15,16]:

$$\delta\lambda_{FWHM}^{CG} = \frac{\lambda \cdot \Lambda}{\pi} \cdot \frac{1}{L_{eff}} \qquad (6.3)$$

The resulting resonance curve with a finite width can, for instance, be interrogated by a narrowband, vertical cavity surface emitting laser diode (VCSEL) by constantly tuning the wavelength of the in-coupled light and subsequent out-coupling via a second grating onto a photosensitive detector, as applied in Ref. 17 (Figure 6.1). Due to the VCSEL's limited tuning range $\Delta\lambda_{VCSEL}$ of approximately 2 nm, the measurement range is also limited within rather narrow bounds, often not sufficient for the detection of larger refractive index shifts, such as caused by larger molecules or sandwich immunoassays.
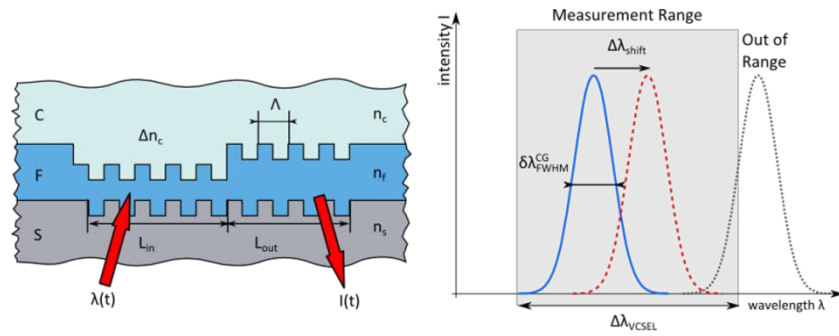
....

Figure 6.1: Schematic representation of a wavelength interrogated waveguide grating coupler and the associated sensing principle: a coherent beam is coupled into the waveguide *F* via a first grating with period *Λ* and length L_{in} and coupled out of the latter via a subsequent grating (**left**). The resonance condition is interrogated via spectral tuning of the light source and monitoring of the corresponding intensity of the out-coupled light. Refractive index changes Δn_c in the cover medium C lead to a shift of the resonance curve by $\Delta\lambda_{shift}$. Vertical cavity surface emitting laser (VCSEL) interrogated waveguide grating couplers exhibit a limited spectral width $\delta\lambda_{FWHM}^{CG}$ as well as a limited measurement range (**right**).

An approach to overcome the first limitation of waveguide grating couplers, namely the limited finesse, is to decouple the angular contribution of the resonance condition from the spectral, e.g., by Bragg gratings. Planar Bragg grating waveguide sensors possess an analogous structure, but instead of coupling light in or out of the waveguide, a certain spectral region of the propagating mode will be reflected within the waveguide, again depending on n_{eff} [18]. The refractive index changes, induced by the quantity to be measured, can be monitored either by the wavelength shift of the entire stop-band or a sharp fringe at its edge by measuring the reflected or transmitted light[19]. Spectral interrogation of such a structure can again be accomplished either by a wide-tunable laser and a photodiode or a broadband light source in combination with a spectrum analyzer. The downside of both approaches is the relatively high initial costs for above-mentioned equipment, a hurdle for point-of-care or handheld devices. Even though the tunable light source could consist of an inexpensive VCSEL, its limited tuning range would require stringent manufacturing

tolerances to the sensor to ensure spectral overlap of the laser's tuning range and the Bragg grating's stop-band edges.

Here, we present the concept and numerical simulations of a Fabry-Pérot type distributed Bragg resonator (DBR) waveguide biosensor with a multitude of high-Q resonance peaks within a broad stop-band. As we shall show, the additional resonance peaks, with free spectral range smaller than the tuning range of the laser, ease the manufacturing tolerances, decrease production costs and increase the dynamic range of the sensor element. The optical transducer is designed as such that no additional effort is required to directly replace the sensor chip of current wavelength interrogated waveguide grating sensors and hereby improving the overall system performance.

6.3   Sensor Elements and Design Considerations

The proposed sensor consists of a light source, a waveguide, two grating couplers, a Fabry-Pérot resonator between two Bragg grating reflectors (DBR's) and finally a photosensitive detector (Figure 6.2). A similar, silicon-based structure has been introduced by Grieco *et al.* as a bistable optical element[20], but not for sensing purposes. Hereinafter, only the DBR sensor and its elements are described in more detail, since the coupling gratings do not act as the sensitive elements but only facilitate the coupling of the light into the waveguide. Despite the increased sensor performance, the structure can be fabricated by the same, standard lithographic means as applied for waveguide grating couplers, which is described in more detail in Ref. 17. The design is driven by considering a tunable VCSEL as interrogating light source.
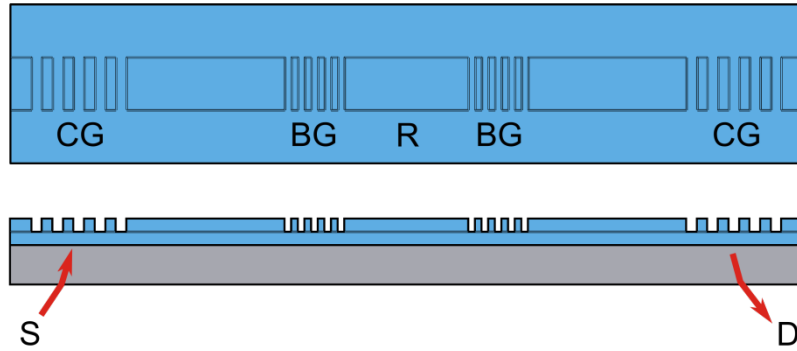
Figure 6.2: Schematic representation of the sensor (top and side view), comprising a coherent source (S), coupling gratings (CG), Bragg gratings (BG), a resonator (R) and a detector (D).

6.3.1   Bragg Grating

Fiber Bragg gratings are optical elements with spatially, periodically varying refractive indices and are extensively used in telecommunication, but also as temperature, strain, pressure, current and (bio)chemical sensors[21]. Said variation of the effective refractive index can be accomplished, e.g., by direct writing of photo-induced, local refractive index changes or waveguide surface. Bragg gratings are not limited to optical fibers but can also be integrated in planar waveguide structures at a high integration density. Contrary to grating couplers, Bragg gratings back-reflect a certain wavelength within the waveguide instead of coupling it in our out. This so-called Bragg wavelength λ_b is defined as[18]:

$$q_b \lambda_b = 2n_{eff} \Lambda \qquad (6.4)$$

where q_b accounts for the Bragg order (for sensing applications, usually $q_b = 1$). Effective refractive index changes Δn_{eff} can therefore directly be measured by a Bragg wavelength shift $\Delta \lambda_b$. A schematic illustration of such a device and a typical transmission spectrum with Bragg wavelength λ_b, stop-band and its side lobes is depicted in Figure 6.3.

As mentioned in the introduction, to measure refractive index shifts, the interrogation of the entire stop-band requires relatively costly equipment or entails stringent manufacturing tolerances to design the

sensor as such that the interrogation laser's wavelength matches the Bragg wavelength respectively the edge of the first side lobe of the gratings spectral response. The proposed structure thus envisages the implementation of a subsequent, secondary Bragg grating, hereby forming an optical cavity or Fabry-Pérot resonator.
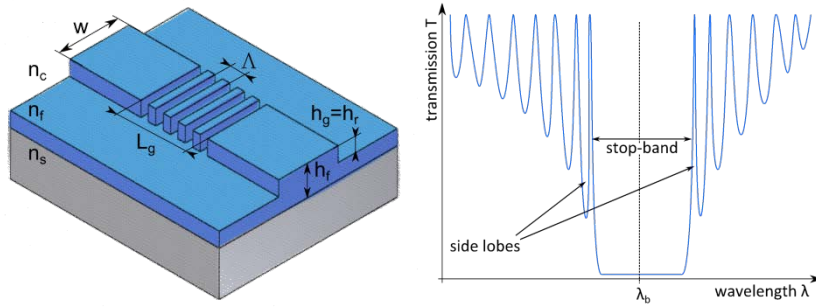
Figure 6.3: Schematic representation of the considered, planar waveguide based Bragg grating reflector (**left**) with the rib width w and height h_r, substrate, film and cover refractive indices n_s, n_f, n_c, grating length L_g, period Λ and depth h_g, respectively. A typical transmission spectrum of a Bragg reflector at Bragg wavelength λ_b is plotted on the right-hand side, highlighting the stop-band and its side lobes.

6.3.2 Fabry-Pérot Resonator

A Fabry-Pérot resonator is an optical oscillator and consists of two spaced reflectors[22]. In the proposed sensor design, the reflectors comprise of corrugated Bragg gratings and the resonator in between of an unstructured waveguide (Figure 6.4). Due to the high reflectivity of the reflectors, incident light is reflected forwards and backwards within the resonator, thereby creating a stationary wave within the cavity which gives rise to a multitude of resonance peaks within the stop band. The spectral distance between the resonance peaks is called free spectral range (FSR) and the spectral width of the peak can be express via the full width at half maximum (FWHM). The resonator's FSR and FWHM can be calculated as follows:

$$\Delta \lambda_{FSR} = \frac{\lambda_0^2}{2 n_{eff}^r d}$$

(6.5)

$$\delta\lambda^{FP}_{FWHM} = \frac{\lambda_0^2}{2\pi n^r_{eff} \, d} \cdot \frac{1-R}{\sqrt{R}} \qquad (6.6)$$

with the resonator's effective refractive index n^r_{eff} and reflectance R.

A characteristic value of a resonator is its finesse $\mathcal{F}$, which is defined as the quotient of the abovementioned FSR between the resonance peaks and the FWHM of the latter.

$$F = \frac{\Delta\lambda_{FSR}}{\delta\lambda^{FP}_{FWHM}} = \pi \frac{1-R}{\sqrt{R}} \qquad (6.7)$$

Whereas the finesse $\mathcal{F}$ describes 2π times the number of back and forth reflections within the resonator cavity, the quality factor or Q-factor represents the optical energy stored in the device, particularly 2π times the ratio of the stored over the dissipated energy per round-trip of the oscillating mode and is defined as the resonance wavelength λ_m of the corresponding mode m divided by its resonance width:

$$Q = \frac{\lambda_m}{\delta\lambda_m} \qquad (6.8)$$

For high sensor performances and low LoDs, high Q-factors are favored since resonant modes with narrower linewidth are more efficient in filtering spectral noise[23]. According to White *et al.*, the standard deviation of the resulting spectral variation σ can be approximated by:

$$\sigma \approx \frac{\delta\lambda_{FWHM}}{4.5(SNR^{0.25})} \qquad (6.9)$$

with the signal-to-noise ratio (SNR) of the resonance peak. Still, the smallest detectable wavelength shift $\Delta\lambda_{min}$ and therefore the experimental LoD is depending on the measurement setup, e.g., its spectral resolution and thermal stability, as explained in more detail in the subsequent section and in Ref. 23. A thoroughly elaborated contribution on the LoD can be found in Ref. 24.
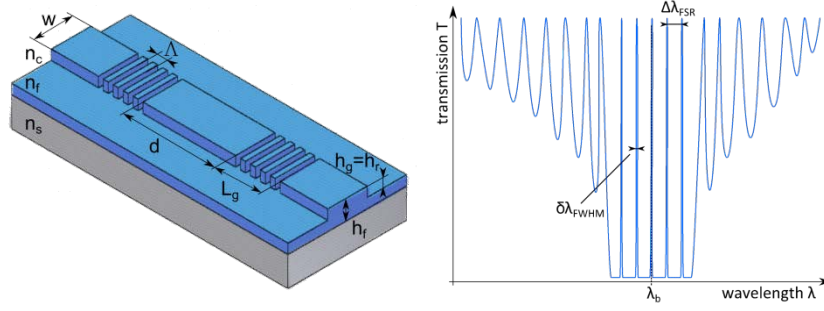
Figure 6.4: Schematic representation of the introduced, planar waveguide based Bragg grating resonator structure (**left**) with the resonator length d, rib width w and height h_r, substrate, film and cover refractive indices n_s, n_f, n_c, grating length L_g, period Λ and depth h_g, respectively. The desired transmission spectrum of the Bragg grating resonator at Bragg wavelength λ_b is illustrated on the right-hand side, highlighting the free spectral range $\Delta\lambda_{FSR}$ and full width at half maximum (FWHM) $\delta\lambda_{FWHM}$.

Compared to a waveguide grating coupler or a single Bragg grating reflector, the implementation of a second grating and the formation of an optical cavity have the advantage to introduce a multitude of resonance peaks with a high finesse within the stop-band of the Bragg grating (Figure 6.4). The FSR of said peaks can easily be defined by the resonator length (Equation (6.5)). Preferably, the FSR should be smaller than the tunable range of the interrogating laser source. Additionally, the Q-factor of the cavity can easily be tuned via the Bragg grating length, as evinced by Equations (6.6) and (6.8).

6.3.3 Sensor Sensitivity

The goal is to design a sensor with maximal sensitivity but small FWHM. As described by Ciminelli *et al.*[6], the minimal detectable bulk refractive index change Δn_{min} is

$$\Delta n_{min} = \frac{m}{2d}\left(\frac{\partial n_{eff}}{\partial n_c}\right)^{-1}\Delta\lambda_{min} \qquad (6.10)$$

and for surface sensing, the minimal detectable mass $\Delta\mathcal{M}_{min}$, where $\mathcal{M} = \Gamma A h_{ad}$, Γ the surface mass density, A the sensor surface area and the adsorbed molecule layer thickness h_{ad},

$$\Delta M_{min} = \Gamma A \frac{m}{2d} \left(\frac{\partial n_{eff}}{\partial h_{ad}} \right)^{-1} \Delta\lambda_{min} \tag{6.11}$$

Since the ratio $m/2d$ is constant at a given wavelength, the minimal detectable refractive index change Δn_{min} is independent of the resonator length d due to the linear scaling with the cavity mode order m [25]. On the other hand, the minimal detectable mass ΔM_{min} depends on the sensing area A. Therefore, the smaller the sensing area A and hence the resonator length d of the device, the smaller the minimal detectable mass ΔM_{min}.

Nonetheless, to ensure overlap of the device spectrum with the tuning range of the proposed interrogating VCSEL laser $\Delta\lambda_{VCSEL}$ and considering Equations (6.5) and (6.11), the optimal resonator length d_{opt} is given by

$$d_{opt} = \frac{\lambda_b^2}{2n_{eff}^r \Delta\lambda_{VCSEL}} \tag{6.12}$$

Together with Equations (6.9)–(6.11) it becomes evident that a low LoD is the result of the combination of large wavelength shifts $\Delta\lambda_{shift}$ per cover refractive index change Δn_c (or more general the sensitivity $s = \Delta\lambda/\Delta n_c$) in combination with a small FWHM. The higher the sensitivity and the Q-factor, the lower the LoD. In order to compare the different designs, the figure of merit (FoM) value can be calculated with

$$FoM = \frac{\Delta\lambda_{shift}}{\Delta n_c \cdot \delta\lambda_{FWHM}^{FP}} = \frac{s}{\delta\lambda_{FWHM}^{FP}} \tag{6.13}$$

High FoMs lead to lower LoDs since smaller spectral shifts can be detected due to the narrow linewidth [6,23]. The LoD can be expressed as the ratio between the sensor resolution σ and its sensitivity s, multiplied by a confidence factor f_c (usually $f_c = 3$):

$$LoD = f_C \frac{\sigma}{s} \tag{6.14}$$

Whereas the sensitivity s is an inherent property of the sensor chip itself, the spectral resolution σ highly depends on the interrogating

reader platform and its individual noise contributions, such as spectral variations induced due to amplitude noise (Equation (6.9)), temperature induced noise as well as the finite spectral resolution of the detector[23]. Since the presented optical transducer is designed to be interrogated by the same measurement platform as the waveguide grating coupler introduced in Ref. 17, therefore with identical thermal and detector noise contributions, the improved finesse directly lowers the spectral variation and hence the LoD of the sensor system.

In general, the complexity as well as the demands on fabrication tolerances and light sources increase with increasing Q-factors. With the proposed DBR approach and a FSR in the range of a cost effective light source, this issues can be overcome, although the fabrication of the devices is not more demanding than for waveguide grating couplers.

6.4   Materials and Methods

Based on the aforementioned statements and considering state-of-the-art, high volume manufacturing capabilities, commercially available VCSEL lasers and dielectric waveguide materials, the DBR sensor design has been optimized by numerical simulations using Coupled Mode Theory (CMT[†])[26]. The input parameters for the calculation of the envisaged design were a VCSEL laser at 850 nm central emission wavelength, with a bandwidth $\delta\lambda_{VCSEL}$ of 100 MHz and a laser tuning range $\Delta\lambda_{VCSEL}$ of 2 nm, a glass substrate with a refractive index of n_s = 1.5156 (Schott D263®eco, Schott AG, Mainz, Germany), a tantalum-pentoxide Ta_2O_5 waveguide film with a refractive index of n_f = 2.097 (Optics Balzers AG, Balzers, Liechtenstein) and a cover refractive index of n_c = 1.329[27], assuming an aqueous cover solution, all at 850 nm. All dielectric materials were considered to be lossless media. The choice of materials and the related refractive indices are based on the waveguide

---

[†] using the RSoftTM module GratingMODTM from Synopsys® (Mountain View, United States)

grating coupler described in Ref. 17, a standard product of the co-authoring company Optics Balzers, to directly compare its performance with the investigated, novel structure. Besides Ta_2O_5 and amongst others, suitable waveguide materials would include titanium-dioxide TiO_2, silicon nitride Si_3N_4 or silicon. The sensitivity towards homogeneous sensing of the devices was evaluated by numerically increasing the cover refractive index Δn_c by 0.005 and investigating the magnitude of the corresponding spectral shift $\Delta\lambda_{shift}$.

6.5 Results

6.5.1 Sensitivity and Figure of Merit

A standard waveguide grating coupler as described in Ref. 17 with a film thickness h_f of 150 nm, refractive indices as abovementioned in Chapter 3 and listed in Table 1 and a grating period Λ of 360 nm illuminated at 850 nm (TM polarization) has been simulated. The spectral shift due to a cover refractive index increase Δn_c by 0.005 resulted in $\Delta\lambda_{shift}$ = 379 pm. Therefore, together with a spectral width (Equation (6.3)) of $\delta\lambda_{FWHM}^{CG}$ = 108 pm, the FoM for this waveguide grating coupler is approximately 702.

Subsequently, considering the aforementioned design criteria and the configuration depicted in Figure 6.3, a rib-waveguide based single-mode TM structure with a single Bragg grating with its central wavelength at 850 nm was simulated, resulting in a grating period Λ of 274.5 nm. The remaining parameters of the sensor design a result of a multi-parameter scan and are listed in Table 1 and illustrated in Figure 6.3. The presented sensor design underlines the basic concept and does not claim to be most sensitive configuration. The resulting transmission spectrum of the single Bragg grating reflector sensor for two different cover refractive indices is shown in Figure 6.5 (left). Increasing the cover refractive index Δn_c by 0.005 resulted in a calculated shift $\Delta\lambda_{shift}$ of the first stop-band edge peak of 512.9 pm. With a spectral side lobe peak-width $\delta\lambda_{FWHM}$ of 346.2 pm, the presented design exhibits a simulated FoM of 296. The result has been validated by numerical-

....

ly confirming the measurements from Pham *et al.* [19], whose presented device possesses (based on our calculations) a FoM of 730, therefore a similar FoM as for waveguide grating couplers.

Table 6.1: Input Parameters for Simulation of the BG Reflector and Resonator.

Parameter	Symbol	BG Reflector	BG Resonator
Rib width	w	1 µm	1 µm
Rib height	h_r	40 nm	40 nm
Waveguide thickness	h_f	160 nm	160 nm
Grating length	L_g	**100 µm**	**2 × 50 µm**
Grating width	w	1 µm	1 µm
Grating depth	h_g	40 nm	40 nm
Grating period	Λ	274.5 nm	272 nm
Resonator length	d	-	**100 µm**
Refractive index of substrate	n_s	1.5156	1.5156
Refractive index of waveguide	n_f	2.097	2.097
Refractive index of cover (water)	n_c	1.329	1.329
Refractive index change of cover	Δn_c	0.005	0.005

The next step was then to introduce a second Bragg grating to form a resonant cavity, whereas the resonator length d was given by Equation (6.12), while keeping all the other parameters fixed to the one of the previous model with only a single Bragg reflector. The outcome of the simulation can be seen in Figure 6.5 (right). As desired, the device's spectral response reveals the additional, high-Q resonance peaks within the stop-band with a FSR $\Delta\lambda_{FSR}$ of 1.96 ± 0.02 nm, which is smaller than tuning range $\Delta\lambda_{VCSEL}$ of the laser as desired, and a FWHM $\delta\lambda_{FWHM}$ down to 3.9 pm for the central peak. The shift of the resonance peaks due to the rise of cover refractive index Δn_c of 0.005 was calculated to be 624.2 pm. Hence, the resulting FoM of the proposed resonant design is approximately 32'010.

....
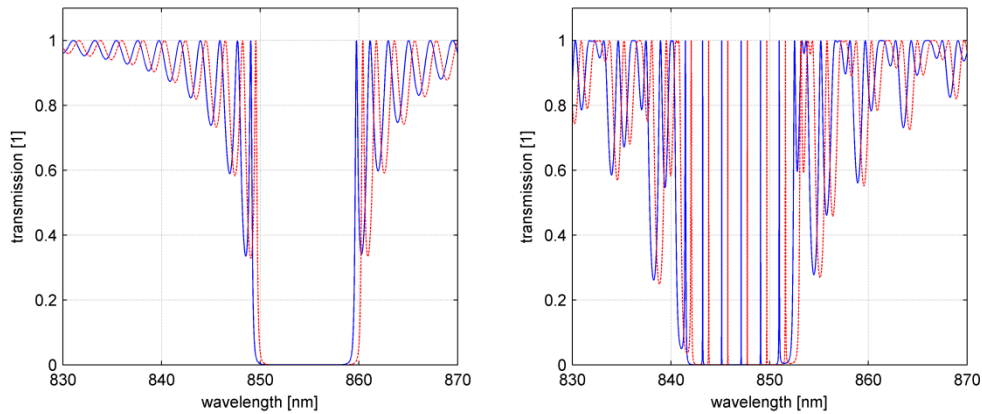
Figure 6.5: Calculated transmission spectra of the Bragg grating reflector (**left**) and Bragg grating resonator (**right**) structure and the associated spectral shift due to a cover refractive index change Δn_c of 0.005 (blue, solid line: n_c = 1.329, red, dashed line: n_c = 1.335).

6.5.2 Measurement Range and Fabrication Tolerances

Besides the higher FoM due to the increased finesse and sensitivity for the resonator compared to the single reflector design, the additional resonance peaks within the stop-band help, on the one hand, to bridge the 2 nm tuning range of the VCSEL laser and therefore increase the transducers dynamic range (Figure 6.6). On the other hand, fabrication tolerances of the sensor chip can be eased since any of the resonance peaks can be present within the tuning range of the VCSEL laser and not strictly the one of side lobes of the stop band, as it is the case for the single reflector. This not only affects the chip but also the VCSEL tolerances due to a relatively large batch to batch variation regarding the central emission wavelength.

The theoretical dynamic range regarding cover refractive index of the Bragg grating reflector has been calculated to span from Δn_c = 1.329 – 1.347 = 0.018. At any higher or lower cover refractive index, the edge of the stop-band is out of the tuning range of the considered laser diode. In the case of the proposed Bragg grating resonator, an adjacent resonance peak will appear in the wavelength range under investigation as soon as the first one is about to leave the latter. Due to this feature, the dynamic range towards cover refractive index reaches from Δn_c = 1.305 – 1.400 = 0.095, or 528% of the single Bragg reflector.

....

Regarding the fabrication tolerances of the Bragg grating reflector, the film thickness h_f for instance needs to be within a narrow and for volume production critical window of 160 nm to 164 nm or within 4 nm, if all the other parameters are regarded as constant and exact. Not only the waveguide thickness, but also its refractive index n_f is subject to some batch to batch variation. For the Bragg reflector type, the acceptable film refractive index ranges from 2.097 to 2.102 and needs to be therefore within rather demanding 0.005. For the Bragg grating resonator, a traceable resonance peak would still be within the detection window even if the film thickness h_f varies between 157.5 nm to 175.0 nm or within 17.5 nm or if the film refractive index spans from 2.084 to 2.102 or within 0.018. The same holds true for the Bragg grating period. With a fabrication tolerance of ±0.2nm for the grating period Λ by interference lithography, the calculated grating period Λ of 274.5 nm as listed in Table 1 for the Bragg grating reflector would require to be within a challenging range of 0.6 nm to ensure the presence of a stop-band side lobe within the interrogation spectrum of the laser source. Due to the multiple, traceable peaks of the resonant Bragg grating sensor, the tolerance for the grating period Λ could be relaxed to 2.8 nm.
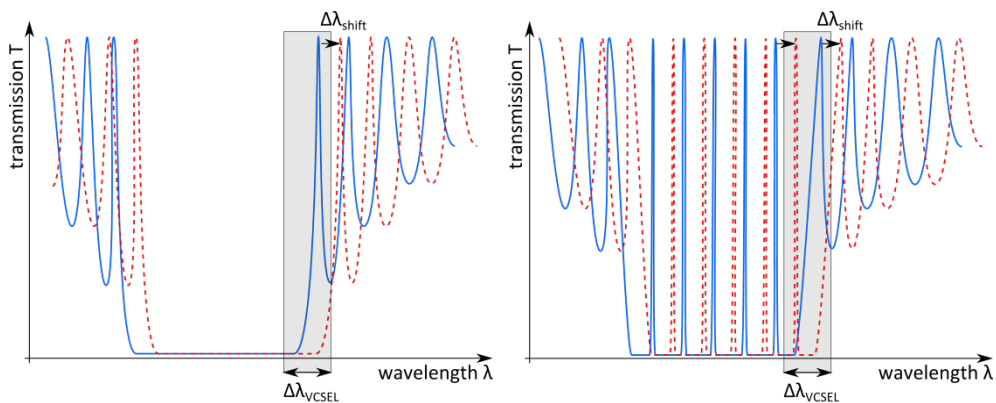
Figure 6.6: The additional resonance peaks within the stop-band help to bridge the 2 nm tuning range of the VCSEL laser $\Delta\lambda_{VCSEL}$ increase the transducers dynamic range and ease the fabrication tolerances. Whereas large spectral shifts $\Delta\lambda_{shift}$ may not be measured with the Bragg grating reflector since the peak shifts out of the detection window (**left**), an adjacent peak appears in the lasers' tuning range in case of the Bragg grating resonator (**right**).

....

6.6 Discussion

The goal of the present study was to introduce and simulate a Bragg grating based waveguide biosensor with manageable fabrication efforts and independence of expensive interrogation equipment by formation of a resonant cavity. The numerical results clearly support the envisaged sensor features, namely a multitude of resonant cavity modes with a higher finesse and sensitivity then waveguide grating couplers in combination with a smaller FSR than the tuning range of the laser. The extended dynamic range of the sensor can be regarded as an additional benefit, as an adjacent resonance peak will appear in the tuning range of the laser if the monitored peak shifts out of the latter due to a significant refractive index change (Figure 6.6). Additionally, besides the abundance of tunable VCSEL lasers at 850 nm, interrogation at shorter wavelengths (850 nm instead of 1550 nm like Pham *et al.* [19]) benefit from an increased surface to bulk sensitivity ratio[28].

Compared to other resonant devices, not only fabrication but also light coupling is rather easy and therefore suitable to substitute current waveguide grating coupler chips in wavelength interrogated sensing systems. Furthermore, due to its linear structure, the waveguide is not subject to neither bending losses and nor to any bus waveguide noise. Nonetheless, high-quality monomode waveguides will be crucial since losses due to scattering as well as absorption might lower the device's Q-factor and hence its FoM.

6.7 Conclusion

The concept, design and numerical simulations of a label-free, distributed Bragg grating resonator biosensor have been introduced. With the disclosed structure, certain shortcomings such as limited dynamic range and finesse, e.g., for waveguide grating couplers, or stringent fabrication tolerances for high-Q waveguide based sensors can be avoided, which is a result of a linear; distributed Bragg grating based resonator structure with a multitude of narrow resonance peaks with

6.8 Author Contributions

....

extended measurement range. Standard lithographic means for sensor production, as well as independence of expensive light-sources and/or detectors, make up an interesting concept for an affordable but sensitive device and are also potentially suitable for point-of-care applications.

6.8 Author Contributions

The presented work is a product of the intellectual environment of the whole team and all members have contributed in various degrees to the conducted research. Florian Kehl conceived the initial sensor concept and wrote the manuscript, David Bischof and Mirjad Keka jointly performed the numerical simulations of the devices, whereas Markus Michler and Ross Stanley contributed to the work through their scientific expertise and by critically reviewing its content.

6.9 Acknowledgements

....

140

6.10 APPENDIX 6.A: Experimental Characterization

6.10.1   Introduction

Several samples were produced according to the aforementioned specifications and characterized regarding their desired geometry as well as spectral response. In addition to the structures previously detailed in this chapter, several design variations of the DBR sensor were realized for gradual device characterization. These structures include: TE waveguides, with a different film thickness and grating depth (h_f = 85 nm, h_g = 15 nm) compared to the TM analogue, DBR waveguides with no coupling grating for end-fire coupling to rule out adverse effects from the latter and slab DBRs without lateral confinement.

6.10.2   Materials and Methods

For the manufacturing of the resonant waveguide chips, the procedure described in Chapter 4 had to be adapted only slightly: the structure required to sputter the waveguide on the substrate in a first step, followed by dry-etching the gratings and rib directly into the Ta_2O_5. The resulting waveguide chip topology was confirmed via AFM measurements (Figure 6.7).
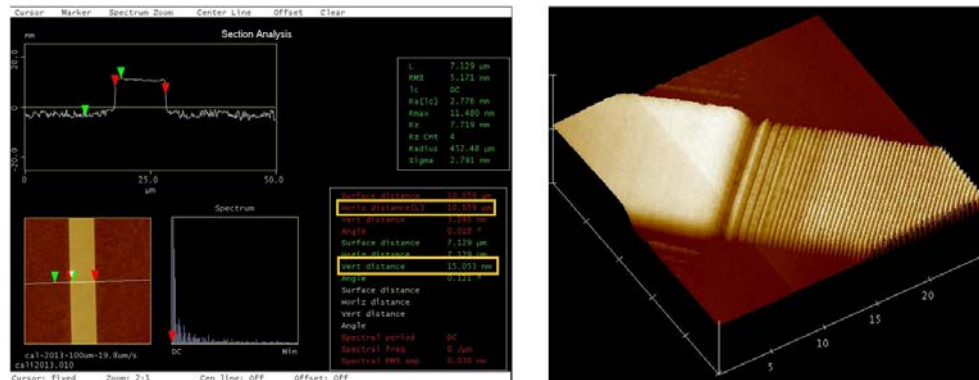

Figure 6.7: Section analysis of a TE rib waveguide section (**left**) and a topographical scan of the rib-Bragg grating-transition (**right**).

As an initial proof-of-concept, the preliminary spectral characterization was based on two DBR configurations, which are detailed in Table 6.2:

....

1. Rib waveguide (TE) with DBR structure without coupling gratings.
2. Slab waveguide (TM) with DBR structure and coupling gratings.

Table 6.2: Design Parameters of Experimentally Characterized DBR Structures.

Parameter	Symbol	1. Rib TE	2. Slab TM
Rib width	w	10 μm	-
Rib height	h_r	15 nm	-
Waveguide thickness	h_f	85 nm	160 nm
Bragg grating length	L_g	2 × 50 μm	2 × 50 μm
Bragg grating width	w	10 μm	-
Bragg grating depth	h_g	15 nm	40 nm
Bragg grating period	Λ	272 nm	272 nm
Resonator length	d	100 μm	100 μm
Coupling grating	CG	no	yes

The rib/TE waveguide was investigated by free-space coupling of a superluminescent, light-emitting diode (SLED, EXS210068-01, Exalos AG, Switzerland) with a central emission wavelength λ_{em} = 855.8 nm and a 3 dB spectral width of 55.6 nm to cover the entire spectral range of the resonator. Coupling was accomplished via a polarization maintaining fiber (PM104509, Thorlabs Inc., Newton, United States), a fiber collimator CFC-5X-B (Thorlabs) and subsequent focusing via a 20x plan achromat objective (RMS20X, Olympus, Japan), as sketched in Figure 6.8. After propagation through the waveguide and the DBR, the light was out-coupled by end-firing and picked up with an achromatic lens (AC080-010-B-ML), a second fiber collimator (F810FC-780) and fed via a multimode fiber (M31L02, all Thorlabs) into an optical spectrum analyzer (OSA, AQ6373, Yokogawa, Japan).
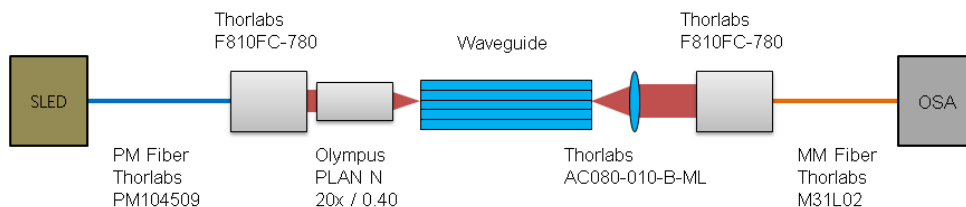

Figure 6.8: Optical setup for the characterization of the rib waveguide DBR chip via end-fire coupling of a SLED and subsequent spectral analysis.

....

The second structure was characterized by coupling the collimated coherent light into the waveguide via the in and out-coupling gratings, as initially envisaged and sketched in Figure 6.2. Its realization is depicted in Figure 6.9. After initial validation of the device's overall resonance spectrum, the SLED and OSA were replaced by a simple, wavelength tuned VCSEL (850-PM-PL-S46XZP, Ulm Photonics, Germany) and a photodiode.
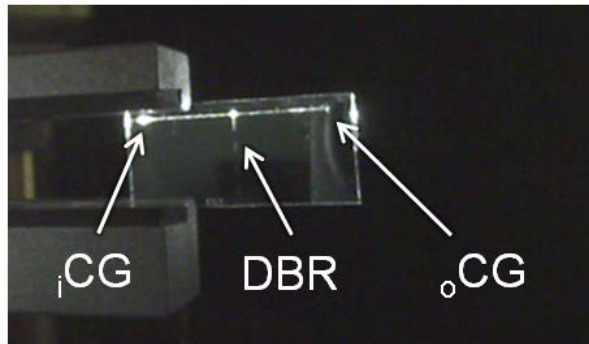

Figure 6.9: The incident beam couples into the slab waveguide via the in-coupling grating ($_i$CG), propagates through the DBR structure and finally couples out via the out-coupling grating ($_o$CG).
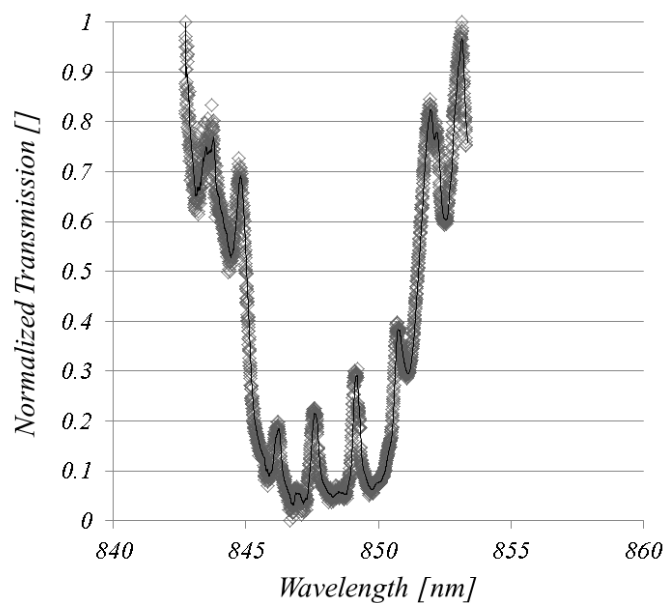

Figure 6.10: Normalized transmission spectrum for structure 2 (slab waveguide, TM). n_c = 1.329 (water).

....

6.10.3 Results

For both investigated cases, a distinct stop-band around λ_b = 850 nm was observable (Figure 6.10) with indications of multiple resonance peaks within the latter when water (n_c = 1.329) was applied to the DBR region. Central stop-band wavelengths were 840.2 nm for the TE, rib waveguide and 848.2 nm for the TM, slab waveguide configuration. For the TE design, an average FSR of 1.70±0.06 nm between the five DBR resonance peaks with a mean FWHM of 89.1±45.5 pm (minimum $\delta\lambda_{FWHM}$ = 52 pm) were measured (Table 6.3). Average FSR of 1.47±0.14 nm and FWHM of 277±9.9 pm resulted for the TM DBR chip. Changing the cover refractive index of the TE waveguide from water to 15 %vol glycerol in water (n_c = 1.351) led to an average peak shift of $\Delta\lambda_{shift}$ = 2.47±0.12 nm, therefore 560.65±27.85 pm for a cover refractive index increase of Δn_c = 0.005. Unfortunately, no conclusive data could be acquired for the TM configuration.

Table 6.3: Resonance Peak Positions, FWHM, FSR and Q-Factor for TE DBR design.

Res. Peak No.	λ_{peak} [nm]	$\delta\lambda_{FWHM}$ [nm]	FSR [nm]	Q-Factor
1	836.808	0.1563	-	5353.86
2	838.408	0.0654	1.600	12819.69
3	840.136	0.056	1.728	15002.43
4	841.864	0.052	1.728	16189.69
5	843.596	0.116	1.732	7272.38

A representative transmission curve of the grating coupled TM waveguide illuminated by the VCSEL source can be seen in Figure 6.11. The cover refractive index was chosen as such that one resonance peak was visible within the tuning range of the VCSEL. In this case, the FWHM of the resonance peak was approximately 70 pm.
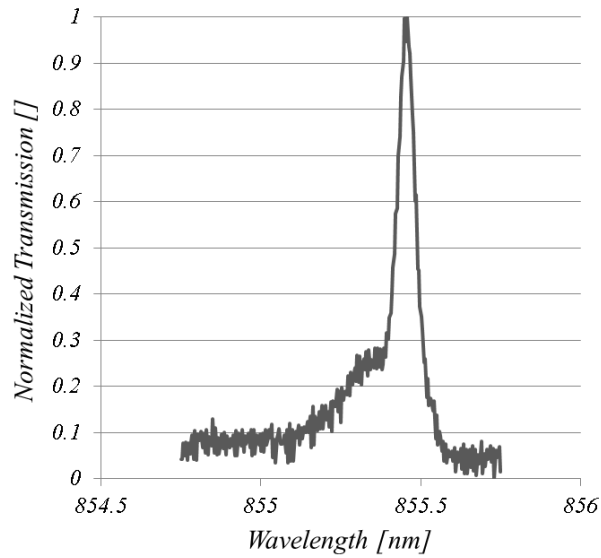
....

Figure 6.11: Resonance peak of TM slab waveguide acquired by wavelength tuning of the illuminating VCSEL source.

6.10.4   Discussion & Conclusions

A planar DBR waveguide sensor has been designed, fabricated and experimentally characterized at a proof-of-concept level. The produced structure was verified by AFM measurements and preliminary spectral measurements confirmed the sensor concept. The structures exhibit a wide stop-band with a multitude of resonance peaks in the range of 840 – 850 nm when covered by an aqueous solution. Additionally, as required, the FSR was smaller than the tuning range of a common VSCEL of approximately 2 nm and a high cover refractive index sensitivity and narrower FWHM compared to waveguide grating couplers could be measured. Nonetheless, the transmission and spectral width of the resonance peaks were lower and wider than desired, hence limiting the cavity's finesse. This can mainly be attributed to inherent losses in the waveguide as well as scattering at the waveguide cover interface. The influence of these parasitic losses on the resonance peak height can be seen in Figure 6.12. In this simulation, the waveguide extinction coefficient k_{wg} has been set to 10^{-6} and 10^{-5}, respectively, resulting in a pronounced damping of the resonance peak transmissions.
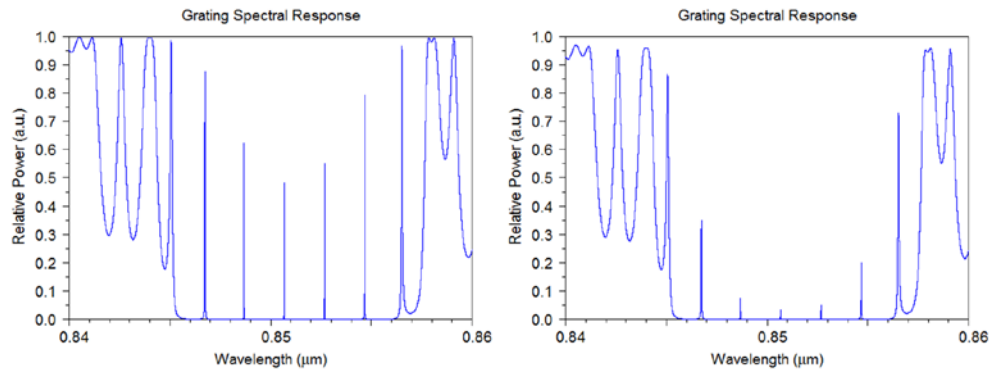
Figure 6.12: Simulated influence of the waveguide extinction coefficient k_{wg} on the transmission spectrum of a DBR structure. (**left**, $k_{wg} = 10^{-6}$, **right**, $k_{wg} = 10^{-5}$).

To reduce the inherent losses of the propagating light, it would be beneficial to use ion-beam sputtering to produce the waveguides instead of magnetron sputtering, yielding lower extinction coefficients. Additionally, the entire waveguide structure (except the sensitive resonator itself) should preferably be coated and buried under a cover dielectric, e.g. SiO_2. This would decrease interfacial scattering, the susceptibility to surface contamination as well as the influence of the cover refractive index on the auxiliary waveguide structures with no sensing purpose, which mainly limited the conducted experiments. By implementation of aforementioned structural changes, a highly sensitive, planar waveguide DBR sensor structure with a high finesse and extended measurement range should therefore be feasible.

6.11 References

1.   Cooper, M. a. Optical biosensors in drug discovery. *Nat. Rev. Drug Discov.* **1,** 515–528 (2002).

2.   Pasche, S. *et al.* Integrated optical biosensor for in-line monitoring of cell cultures. *Biosens. Bioelectron.* **26,** 1478–1485 (2010).

3.   Bier, F. F. & Schmid, R. D. Real time analysis of competitive binding using grating coupler immunosensors for pesticide detection. *Biosens. Bioelectron.* **9,** 125–130 (1994).

4.   Vörös, J. *et al.* Feasibility study of an online toxicological sensor based on the optical waveguide technique. *Biosens. Bioelectron.* **15**, 423–429 (2000).

5.   Cooper, M. Label-free biosensors: techniques and applications. (2009).

6.   Ciminelli, C., Campanella, C. E. C. M., Dell'Olio, F., Campanella, C. E. C. M. & Armenise, M. N. Label-free optical resonant sensors for bio-chemical applications. *Prog. Quantum Electron.* **37**, 51–107 (2013).

7.   Schmitt, K., Oehse, K., Sulz, G. & Hoffmann, C. Evanescent field Sensors Based on Tantalum Pentoxide Waveguides – A Review. *Sensors* **8**, 711–738 (2008).

8.   Kozma, P., Kehl, F., Ehrentreich-Förster, E., Stamm, C. & Bier, F. F. Integrated planar optical waveguide interferometer biosensors: A comparative review. *Biosensors and Bioelectronics* **58**, 287–307 (2014).

9.   Estevez, M. C., Alvarez, M. & Lechuga, L. M. Integrated optical devices for lab-on-a-chip biosensing applications. *Laser Photon. Rev.* **6**, 463–487 (2012).

10.   Vahala, K. K. J. Optical microcavities. *Nature* **424**, 839–846 (2003).

11.   Wang, Q., Zhang, D., Wang, Z. & Huang, Y. Optimizing the quality factor of a wideband guided-mode resonance biosensor. *Appl. Phys. A* **117**, 553–556 (2014).

12.   Tamir, T. Guided-wave optoelectronics. (1988).

13.   Nellen, P. M., Tiefenthaler, K. & Lukosz, W. Integrated optical input grating couplers as biochemical sensors. *Sensors and Actuators* **15**, 285–295 (1988).

14.   Kunz, R. E., Dübendorfer, J. & Morf, R. H. Finite grating depth effects for integrated optical sensors with high sensitivity. *Biosens. Bioelectron.* **11**, 653–667 (1996).

15.   Brazas, J. & Li, L. Analysis of input-grating couplers having finite lengths. *Appl. Opt.* **34**, (1995).

6.11 References

16.   Norton, S. M., Erdogan, T. & Morris, G. M. Coupled-mode theory of resonant-grating filters. *J. Opt. Soc. Am. A* **14,** 629 (1997).

17.   Cottier, K., Wiki, M., Voirin, G., Gao, H. & Kunz, R. E. Label-free highly sensitive detection of (small) molecules by wavelength interrogation of integrated optical chips. *Sens. Act., B Chem.* **91,** 241–251 (2003).

18.   Hill, K. O. & Meltz, G. Fiber Bragg grating technology fundamentals and overview. *J. Light. Technol.* **15,** 1263–1276 (1997).

19.   Pham, S. V. *et al.* On-chip bulk-index concentration and direct, label-free protein sensing utilizing an optical grated-waveguide cavity. *Sensors Actuators, B Chem.* **174,** 602–608 (2012).

20.   Grieco, A. *et al.* Optical Bistability in a Silicon Waveguide Distributed Bragg Re fl ector Fabry – Pérot Resonator. **30,** 2352–2355 (2012).

21.   Lee, B. Review of the present status of optical fiber sensors. *Optical Fiber Technology* **9,** 57–79 (2003).

22.   Vaughan, M. The Fabry-Perot interferometer: history, theory, practice and applications. (1989).

23.   White, I. M. & Fan, X. On the performance quantification of resonant refractive index sensors. *Opt. Express* **16,** 1020 (2008).

24.   Loock, H.-P. & Wentzell, P. D. Detection limits of chemical sensors: Applications and misapplications. *Sensors Actuators B Chem.* **173,** 157–163 (2012).

25.   De Vos, K., Bartolozzi, I., Schacht, E., Bienstman, P. & Baets, R. Silicon-on-Insulator microring resonator for sensitive and label-free biosensing. *Opt. Express* **15,** 7610 (2007).

26.   Huang, W. Coupled-mode theory for optical waveguides: an overview. *JOSA A* (1994).

27.   Hale, G. M. & Querry, M. R. Optical Constants of Water in the 200-nm to 200-microm Wavelength Region. *Appl. Opt.* **12,** 555–563 (1973).

28.   Ganesh, N., Block, I. D. & Cunningham, B. T. Near ultraviolet-wavelength photonic-crystal biosensor with enhanced surface-to-bulk sensitivity ratio. *Appl. Phys. Lett.* **89,** 023901 (2006).

7 Conclusions and Outlook

Because of the cumulative character of the present thesis, consisting of a collection of published, self-contained articles, the reader is referred to the specific conclusions at the end of the individual chapters. Nonetheless, a general Conclusion and Outlook shall be given hereafter.

This thesis covered theoretical as well as practical aspects of a novel, label-free biosensor development. After a chapter on the fundamental theory and the field-of-use of dielectric waveguide sensors, the reader was introduced to various numerical methods to accurately simulate and optimize the performance of waveguide grating couplers. In Chapter 3, a new algorithm, based on FEM, TLTMM and model-based search, was presented for the sensitivity calculation of a grating based dielectric biosensor. The methods allow for consideration of non-negligible parameters such as grating depth, duty-cycle, shape, inherent losses and surface roughness. Thus, most of the sensor parameters can be taken into account and a global optimization of the chip is possible with a procedure that is rather easy to implement with the help of standard simulation software. Since one of the key advantages of grating based biosensors is the number of tuning parameter, it is crucial to be able to simulate the impact of each variable for the design.

In the subsequent Chapter 4, numerous waveguide grating chips were fabricated and the refractometric sensitivity of these sensors was experimentally determined for different waveguide thicknesses, wavelengths and polarizations of the incident light. The results were compared with numerical calculations to verify well-established theory. A good agreement between theoretically calculated and experimentally measured sensitivity was observed. Therefore, it can be concluded that the sensitivity of the coupling angle towards the change of the bulk refractive index can accurately and reliably be modeled with established

theory. This study aimed at filling a gap in the published literature by experimentally reconstructing the sensitivity curves for waveguide grating coupler based sensors.

In Chapter 5, a novel, label-free sensor platform (ARGOS) based on angular interrogation with a scanning MEMS mirror was introduced and validated towards refractometric as well as bioaffinity measurements for large and small molecules. The refractometric measurements confirmed the extended dynamic range, a high linearity and sensitivity of the ARGOS system. Due to the high flexibility towards the implemented laser source in the ARGOS system, both power and wavelength ranges are vast and the appropriate light source can be chosen according to the specific application or measurement configuration. The advantageous SBSR for the interrogation at short wavelengths was computationally as well as experimentally demonstrated. Additionally, a self-referencing waveguide grating sensor was introduced, fabricated and qualitatively investigated towards prevalent physical perturbations. The individual system components, such as electronics, optics and fluidics were described in the chapter's appendix. Although it can be concluded that with its relatively compact size, weight and low power consumption, the ARGOS system is well-suited for battery powered field measurements, further development efforts regarding assay development are required. Moreover, the system should further be miniaturized, including integrated microfluidics, reagents and pumps, to eventually come up with a monolithic, easy-to-use, hand-held sensor device on a lab-on-a-chip basis.

A design study of a novel sensor approach was introduced in Chapter 6. The distributed Bragg grating resonator aims at overcoming certain shortcomings such as limited dynamic range and finesse for waveguide grating sensors. The formation of a resonant cavity in a planar waveguide results in a multitude of resonance peaks with high finesse, but with the manageable complexity of waveguide grating couplers. Compared to grating couplers or simple Bragg grating reflectors, the multiple resonance peaks are an advantage since they potentially allow for interrogation with low-cost equipment such as VCSELs and

simple photodiodes instead of costly laser sources or spectrometers. Compared to other high-Q resonant cavity sensors, the proposed design can be fabricated with relatively simple, standard lithographic means. First samples were successfully fabricated and qualitatively characterized. The preliminary measurements confirmed the sensor concept as structures exhibited a wide stop-band with a multitude of resonance peaks in the range of 840 – 850 nm when covered by an aqueous solution. Additionally, the FSR was smaller than the targeted 2 nm, a requirement for the consistent interrogation with a VCSEL source. Nonetheless, the transmission and spectral width of the resonance peaks were lower and wider than desired, hence limiting the cavity's finesse. This can mainly be attributed to inherent losses in the waveguide as well as scattering at the waveguide cover interface. To reduce the inherent losses of the propagating light, it would be beneficial to use ion-beam sputtering to produce the waveguides and additionally burry the latter, except for the sensitive resonator area, in a protective cover layer. Further engineering and development efforts by implementation of aforementioned structural changes, a highly sensitive, planar waveguide DBR sensor structure with a high finesse and extended measurement range should, therefore, be feasible.

In general it can be concluded that biosensors already are and will become even more important in our everyday lives in the near future. Checking the quality of our food and beverages or search for allergens in the latter, continuously monitoring our body and vital signs, specifically adapt and customize a patient's medication, detect traces of water- and airborne chemicals and pathogens and so forth, is of increasing interest in various sectors such as healthcare, security and environmental monitoring, but also for consumer products. Whereas modern cell-phones, for example, are equipped with analogues of most of our senses, such as sight (camera), hearing (microphone), touch (touch-screen), thermoception (temperature sensor) and balance (gyroscopes), the ability to taste and smell still lacks in its technological implementation. Integrated optics in combination with recent developments in MEMS technologies and integrated electronics will facilitate

the development of truly miniaturized lab-on-a-chip biosensors, but evanescent field based sensors are highly interesting candidates due to their extreme sensitivity. Nonetheless, many technological problems still need to be overcome in order to realize robust, versatile and easy to use sensors for the connection with real-world applications in the consumer market. On one hand, the technology still faces substantial challenges towards the integration in hand-held devices. Stable light sources and highly efficient temperature control in order to reduce noise and drift, correct and simple liquid-handling, stable surface chemistries with long shelf-lives with high specificity to eliminate false-positive signals, still remains extremely challenging and requires further technological advances. With the on-going research efforts and recent developments in academia as well as industry, there can be no doubt that integrated optical biosensors will be ubiquitous in our future society and will have a positive impact on our lifestyles.
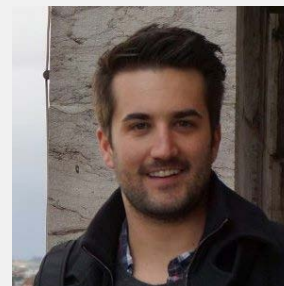
Florian **Kehl**

// Education

10/2010 – 06/2015	**ETH Swiss Federal Institute of Technology, Zürich, Switzerland**	

PhD Candidate, *Laboratory of Biosensors and Bioelectronics, Dept. of Information Technology and Electrical Engineering. Advisor: Prof. Janos Vörös. In collaboration with CSEM.*

Development of a multiplex robust, label-free, remotely-controlled and portable optical biosensor platform for online monitoring of toxins and pollutants in the aquatic environment. Involved in system design, opto-mechanics, electronics and microfluidics.

03/2009 – 09/2009 **University of California, Berkeley, USA**
Master's Thesis/Visiting Research Scholar,
Berkeley Sensor & Actuator Center (BSAC)
Advisor: Prof. Kris S. J. Pister

Research on an autonomous, guided small scale rocket with gimbaled thrust and MEMS 6 DoF inertial measurement unit.

10/2007 – 02/2010 **University of Basel, Switzerland**
Master of Science, *Master in Nanophysics*

Final grade: 6.0/6.0
Semester Thesis: Feasibility Study and Development of a Fluorescent Screen on an Ultraviolet Laser Projector

10/2004 – 09/2007 **University of Basel, Switzerland**
Bachelor of Science, *Major in Nanoscience*

08/1999 – 08/2003 **Highschool Degree, KSS Sargans, Switzerland**

// Experience

01/2011 – 06/2015 **Optics Balzers AG, Liechtenstein**
Project Leader, *R&D Biochip Engineering*

Responsible for R&D engineering efforts in the field of waveguide grating biosensors. Scientific and technical leader in a European FP7 project. Manager of a research project funded by the Swiss commission for technology and innovation CTI.

04/2010 – 12/2010
&
08/2007 – 03/2009
Swiss Center for Electronics and Microtechnology CSEM SA, **Landquart, Switzerland**
R&D Intern

Development of a waveguide grating based optical biosensor platform and its microfluidic cartridge, incl. assay development.

// Profile

// Name
Florian Kehl
// Date of Birth
April 13th, 1984
// Nationality
Swiss
// Civil Status
Single, no children

// Expertise

Integrated Optics, (Bio)chemical Sensing, Systems Engineering, Photonics, MEMS, Lasers, Nanotechnology, Lithography, Microfabrication, Simulations, µFluidics, Waveguides, CAD, Thin Films, Integration, Clean Room Technologies, R&D

// Contact

// Address
Lukmaniergasse 8
CH-7000 Chur
Switzerland

// Phone
+4179 734 7816

// Email
florian.kehl@gmail.com

// Website

// Peer-Reviewed Publications

2015   *An Attitude Controller for Small Scale Rockets*
F. Kehl, A.M. Mehta, K.S.J. Pister, *Springer Tracts in Advanced Robotics*, **2015**,*105*: 201-214.

Design of a Label-Free, Distributed Bragg Grating Resonator Based Dielectric Waveguide Biosensor
F. Kehl, D. Bischof, M. Michler, M. Keka, R. Stanley, *Photonics*, **2015**; *2(1)*:124-138.

Automated and portable solid phase extraction platform for immuno-detection of 17β-estradiol in water
S. Heub, N. Tscharner, V. Monnier, **F. Kehl**, P.S. Dittrich, S. Follonier, L. Barbe,
Journal of Chromatography A, **2015**,*1381*: 22–28.

Experimental Validation of the Sensitivity of Waveguide Grating Based Refractometric (Bio)sensors
T. E. Gartmann[†], **F. Kehl**[†]*, Biosensors, 2015; 5(2):187-198.*

2014   *Integrated planar optical waveguide interferometer biosensors: a comparative review*
P. Kozma, **F. Kehl**, E. Ehrentreich-Förster, C. Stamm, F. F. Bier,
Biosensors and Bioelectronics, **2014**, *58*: 287-307.

2013   *FEM-Based Method for the Simulation of Dielectric Waveguide Grating Biosensors*
T. Guillod, **F. Kehl**, and C. V. Hafner,
Progress In Electromagnetics Research, **2013**,*137*: 565-583.

2010   *Hybrid Robot Gripper and Tools for Handling and Bonding Micro Fluidic Chips*
M. Altmeyer, A. Koller-Hodac, S. Walpen, E. Krüttli, M. Lüthy, **F. Kehl,** J. Auerswald,
ISR/ROBOTIK, **2010,** 1-6.

2009   *Optimal hybridization efficiency upon immobilization of oligonucleotide double helices*
J. Razumovitch, K. de França, **F. Kehl**, M. Wiki, W. Meier, C. Vebert,
Journal of Physical Chemistry B, **2009**, *113(24)*: 8383-8390.

// Patent Applications

Measurement method based on an optical waveguide sensor system
F. Kehl, S. Follonier, PCT/EP2014/061740 (WO2014EP61740), pending.

Integrated optical waveguide sensor system
F. Kehl, M. Keka, M. Michler, R. Stanley, PCT/EP2014/001579, pending.

// Skills

Languages:		
	German:	mother tongue
	English:	oral and written fluency
	French:	conversational

Technical: Full system integration and prototyping from optics, electronics, mechanical design to software engineering. Extensive practical experience in (bio)chemistry-, optics-, electronics- and clean room laboratories, mechanical workshops including CNC machining, AFM, Lithography, RIE.

Management: Project management, project acquisition, supervision and lead of technicians and students (3 Master's & 4 semester theses), 4 years of experience in industry and product development.

Software:

Inventor	●●●●○
Solidworks	●●●○○
Eagle CAD	●●●○○
Matlab	●●●●●
LabView	●●●●○
COMSOL	●●●○○
ZEMAX	●●●○○
MS Office	●●●●●

// Grants

2012   **CTI Research Grant (No. 13865.2 PFNM-NM)**
Swiss Commission for Technology and Innovation
Amount: 470'196 CHF (509'000 USD)

2009   **Nanoscience Argovia Travel Grant**
Swiss Nanoscience Institute, University of Basel
Amount: 4'000 CHF (4'300 USD)

// Awards

2013   **Award for Outstanding Poster Presentation**
Elsevier, 3rd Int. Conf. on Bio-Sens. Technology, Spain.

2008   **Best Poster Award**
INASCON, Arhus, Denmark.

// Presentations

2014   ***Development of an integrated, label-free, waveguide grating based biosensor platform for on-the-spot measurements and online monitoring of toxins and pollutants in food production processes and in the aquatic environment.***
F. Kehl, N. Tscharner, G. Etlinger, S. Follonier, J. Vörös, *Scientific Symposium: Small Solutions for Big Water-Related Problems - Innovative microarrays and small sensors to cope with water quality and food security, October 26-28, 2014, Rome, Italy*

2013   ***An Attitude Controller for Small Scale Rockets,*** A. Mehta, F. Kehl, *9th International Conference on Field and Service Robotics, December 9-11, 2013, Brisbane, Australia*

2012   ***Combined FEM and analytical method for the simulation and optimization of planar dielectric waveguide grating biosensors,*** F. Kehl, T. Guillod, *8th Workshop on Numerical Methods for Optical Nano Structures, July 2-4, 2012, Zürich, Switzerland*

2009   ***Real-time attitude determination and control of sounding rockets for deployment of wireless sensor networks***
F. Kehl, *Micro Autonomous Systems and Technology - Collaborative Technology Alliance (MAST-CTA); June 2009, University of California, Berkeley, USA.*

// Extracurricular Activities

Since 2013   **Member of the Astronomical Society Graubünden,** Falera, Switzerland

Since 2010   **Lead Singer in Music Formation,** Azmoos, Switzerland

07/2003 & 10/2004   **Aeronautical Training Courses for Paratroopers,** Swiss Army, Switzerland

03/2004 – 08/2004   **Reconnaissance Soldier,** Swiss Army, Switzerland

Since 2003   **Licensed Ski Instructor (J&S),** Federal Office of Sports, Switzerland

06/1995 – 08/2000   **Pitcher, Baseball Club Buchs,** Buchs, Switzerland

08/1997   **Scuba Diving Certificate,** Buchs, Switzerland

// Personal Interests

Astronomy, (Astro)photography, Travelling, Playing Music/Singing, Skiing, Hiking

$$2kh_f\sqrt{n_f^2 - n_{eff}^2} + \varphi_{fc} + \varphi_{fs} = 2\pi m_{wg}$$

Acetazolamide
222.2 Da

$$E_{m,s,0} = \begin{cases} \cos(\theta_m) \\ 0 \\ \sin(\theta_m) \end{cases}$$

$$\beta_{m,s} = |\Re(k_{m,s,y})|$$